THE NUCLEO-CYTOPLASMIC FUNCTION OF ACTIN AND ACTIN DEPOLYMERIZATION FACTORS IN PLANT IMMUNITY

By

Pai Li

A DISSERTATION

Submitted to
Michigan State University
in partial fulfillment of the requirements
for the degree of

Plant Biology – Doctor of Philosophy
Molecular Plant Sciences – Dual Major

2022

ABSTRACT

THE NUCLEO-CYTOPLASMIC FUNCTION OF
ACTIN AND ACTIN DEPOLYMERIZATION FACTORS IN PLANT IMMUNITY

By

Pai Li

The plant immune system is a multi-phase complex network that involves the collaboration of multiple subcellular structures. In the past two decades, the core signaling pathways of the immune process, including pattern-triggered immunity (PTI), effector-triggered immunity (ETI), and systemic acquired resistance (SAR), as well as the behavior of organelles, have been revealed to a level of clarity that is able to describe a general and well-covered process of the immune response. However, there are still many events during the immune response that remain mysterious. For instance, while higher plants live a sessile lifestyle, there are countless intracellular motions mediated by the cytoskeleton (including its associated proteins) in response to the external triggers, such as the invasion of pathogens. As our knowledge of plant immunity accumulates, the deficiency in knowledge on how immune signaling regulates the behavior of the cytoskeleton as a critical aspect of defense response, howbeit, becomes more evident. Therefore, this is a field of research that calls for powerful toolboxes to facilitate the analysis of the cytoskeleton in the context of immunity, as well as instructive biological model(s) that guide the direction of the multifarious studies.

In this dissertation, I focus on the summary and prospective discussion on the immune function of the actin cytoskeleton and, more importantly, describe my original studies on two major aspects of this topic. First, a prerequisite to functional study of the actin cytoskeleton in the cytoplasm is the ability to accurately describe the status of the cytoskeleton. To achieve this goal, I developed an algorithm, namely implicit Laplacian of enhanced edge (ILEE), to accurately identify and analyze the biological status of the cytoskeleton from confocal image samples. This method

significantly improves the accuracy, stability, and robustness of cytoskeleton segmentation, solves other technical hindrances, and enables abundant information to be extracted from images for biological interpretation (see *Chapter 2*). The ILEE algorithm will further help me to explore the phenotypes of actin architecture in response to immune signaling, which was not previously available due to the lack of the toolbox. Also, the ILEE has been packaged as a library released publicly to benefit the community with a powerful cytoskeleton analysis platform.

For the second project of my total research, I focused on the immune function of the actin cytoskeleton in the nucleus. Previously, some Arabidopsis actin depolymerization factors were reported to genetically contribute to plant immunity by unknown mechanism(s), and my story began with a novel activity identified among Arabidopsis actin depolymerization factors – to interact with WRKYs, the stress-responsive transcription factors. During my research, I proved that certain ADFs can form a complex with WRKYs that binds to targeted promoters, hence regulating the activity of WRKYs and playing a positive role in the immune response. The knowledge obtained through this study, in combination with previous research (Lu et al., 2020; Porter et al., 2012) of my lab, can be summarized into a biological model, in which ADF mediates a nuclear-cytoplasmic immune regulation that systemically facilitates both cytoskeleton dynamics and pro-immune transcriptome reprogramming. In general, this study reveals a novel yet general pattern of cytoskeleton mediated transcriptional regulation, as ADF and perhaps other components of the actin cytoskeleton can shuttle between the cytoplasm and nucleus to form a network with a higher level of complexity. As a potential broader impact, the application range of this model includes but is not necessarily limited to plant immunity.

ACKNOWLEDGEMENTS

“Day as a teacher, father livelihood.” I would like first to thank my advisor Dr. Brad Day, for his generous offer of the opportunity to work on the interesting and inspirational research on the functionality of actin cytoskeleton in plant immunity, as well as his warm, illuminative guidance and crucial support on science, academia, and life. Dr. Brad Day provided me with the accessibility to multiple intervolved yet intriguing projects of study, which trained me to think big and systematically to ask critical questions and explore the unknown. Without his guidance, I would not have developed my ability to act as a proud scientist.

I would like to thank the previous and current members of the Day Lab, Dr. Amy Baetsen-Young, Alex Corrian, Huan Chen, Dr. Kun Jiang, Dr. Brittni Kelley, Dr. Yong-sig Kim, Dr. Yi-ju Lu, Bruce Proctor, Dr. Hikari Sakamoto, Dr. Masaki Shimono, Dr. Saroopa Samaradivakara, Yoichiro Tanaka, Rikako Yamauchi, and Dr. Yi Zhao, for the happy, supportive, and enjoyable vibe we created and have maintained. Special thanks to Dr. Yi-ju Lu, who provided me with critical initial lab training and endless support, Alex Corrian, who discovered the critical evidence that inspired my research, and Bruce Proctor, who helped my research by great efforts as a trustworthy, highly performed undergrad assistant.

I would like to thank Dr. Sheng Yang He, my secondary advisor, for his thought-provoking and rigorous training in my study. After having acquaintance with him at an international conference, he introduced me to Dr. Day, which provided me with the precious opportunity to enjoyable research at MSU. I would also like to thank the members of the He Lab, for the warm, illuminative environment and critical advice on my study, all of which contributed to my success from a different perspective.

I would like to thank my collaborator Ze Zhang and Dr. Yiying Tong of the Department of Computer Science and Engineering, MSU, for their significant contribution to developing the ILEE algorithm, as introduced in *Chapter 2* of the dissertation.

I would like to thank my Ph.D. Graduation Committee members Dr. Katherine W. Osteryoung and Dr. Shin-Han Shiu, for their critical guidance on the general direction and crucial details of my research.

I would like to thank Urumqi No.1 Senior High school (my high school), Sun Yat-sen University (my undergrad institute), and MSU for the professional and well-rounded education that successfully introduced me to academia. I would also like to especially thank Dr. Yongjun Lu, and the members of the Lu Lab at School of Life Sciences, Sun Yat-sen University, who introduced me to the world of plant-pathogen interaction and provided me opportunities to participate and lead multiple studies, as well as the professional training identical to the level of a master or even doctoral student, despite I was an undergrad.

Finally, I would like to thank my mother, Jihong Yang, and my father, Nanzheng Li, who gave me a great native family full of respect, open-mindedness, and sustained support. As the first doctor ever in the family's history, my achievements are the best proof of your efforts as outstanding parents. I would also like to thank my girlfriend Xuan Xie, who has stayed with me for nine years and shared me with her happiness, care, and wisdom, without which I would never make through the adversity in my life along the way.

TABLE OF CONTENTS

LIST OF TABLES.....viii

LIST OF FIGURES ix

KEY TO ABBREVIATIONS.....xii

Chapter 1: The plant immunity and the immune-regulatory function of cytoskeleton.....1
Chapter abstract.....1
Plant biotic interaction.....2
Core signaling mechanism of plant immunity.....7
Immune attenuation: rebalancing growth versus defense.....16
The immune functionality of Plant cytoskeleton.....20
The cytoskeleton as a molecular and cellular scaffold of plant immunity.....21
The actin cytoskeleton is required for turnover of PM-localized PRRs.....24
The role of the cytoskeleton in intercellular trafficking of immune-associated processes.....26
Battlefield cytoskeleton: the frontline of plant-pathogen interaction.....28
Pathogen targeting of cytoskeletal organization: immune subversion and pathogenicity..32
Emerging themes on the immune functions of the nuclear actin cytoskeleton.....36

Chapter 2: Implicit Laplacian of Enhanced Edge (ILEE): An unguided algorithm for accurate and automated quantitative analysis of cytoskeletal images.....38
Chapter abstract.....38
Introduction and rationale.....39
Results.....43
The ILEE pipeline.....43
Identification of coarse background.....44
Cytoskeleton segmentation by ILEE.....46
Computational analysis of cytoskeleton indices.....50
ILEE displays high accuracy and stability over actin image samples.....52
ILEE leads to discovery of new features of actin dynamics in response to bacteria.....56
ILEE has broad compatibility with various sample types.....60
Discussion.....62
Methods.....66
Plant genotypes and growth.....66
Bacteria growth and plant inoculation.....66
Mouse cancer cells sample.....66
Confocal microscopy.....67
Manually portrayed ground truth binary image.....67
Double-blind MGT analysis.....68
Statistical analysis and data visualization.....68
Determination of *K2* for sample batches.....68
ILEE.....69
Computation of cytoskeletal indices.....76
Methods Library API reference.....78

Chapter 3: The nuclear cytoplasmic function of actin depolymerization factors (ADFs) in plant Immunity……80
Chapter abstract……80
Introduction and rationale……81
Results……82
WRKY transcription factors are potential ADF interactors……82
The Expression pattern of ACT, ADF, and WRKY……84
The interaction specificity of Arabidopsis leaf ADF-WRKY interactome……87
ADFs interact with WRKY-DNA complex……89
Certain ADFs enhance the transcription promoting activity of WRKYs……92
ADF4 stabilizes the interacted WRKYs……96
Nuclear ADF4 contributes to resistance against pathogen……98
ADF4, while binding WRKY29, targets immune-regulatory genes genome-widely and regulate WRKY29 activity and targeting spectrum……100
Inspection of the ADF interaction interface……103
Discussion……106
Methods……110
Plant Growth……110
Construction of vectors……110
DNA point-mutation……112
Agrobacteria-mediated transformation……112
Protoplast transformation……113
Confocal microscopy……113
Semi-quantitative BiFC……114
Promoter reporter assay……114
ChIP-qPCR……116
ChIP-seq……116
Bacterial growth assay……117
Transcriptional temporal pattern analysis of ACT, ADF, and WRKY……117
Statistics and visualization……118

APPENDICES……119
APPENDIX A: Appendix A: supplemental figures of ILEE……120
APPENDIX B: Proposed future experiments……139
APPENDIX C: Specialized primers in this study……141

REFERENCES……142

LIST OF TABLES

Table 3-1: selected WRKYs and their phylogenic groups……..….86

Table AC-1: list of specialized primers used in the study herein. Primers for ADF4 mutation and ChIP-qPCR are listed……..141

LIST OF FIGURES

Figure 1-1: Invasion strategies by phytopathogens……3

Figure 1-2: A schematic map of plant local immunity……8

Figure 1-3: Dynamics of signaling processes associated with local immunity……..12

Figure 1-4: Schematic diagram of cytoskeleton polymerization/depolymerization (treadmilling)..21

Figure 1-5: The versatility and involvement of the plant cytoskeleton in immunity……22

Figure 1-6: The cytoskeleton is central to the balance between immunity and susceptibility, and the host-dominated balance and alterability between G-actin, F-actin, and tubulin control the plant response to pests and pathogens……...34

Figure 2-1: ILEE pipeline and the demonstration of cytoskeletal indices……42

Figure 2-2: NNES global thresholding……45

Figure 2-3: Cytoskeletal identification by ILEE……47

Figure 2-4: Visualized demonstration of concepts of cytoskeleton indices……51

Figure 2-5: ILEE shows superior accuracy and robustness over classic thresholding approaches……53

Figure 2-6: ILEE library enables the discovery of actin dynamic features of bacteria infected leaf tissue……57

Figure 3-1: AlphaScreen and co-localization assay reveal potential existence of ADF-WRKY interaction……83

Figure 3-2: Expression pattern of all ACTs, ADFs, and WRKYs in Arabidopsis leaves upon immune signaling……....85

Figure 3-3: ADF-WRKY interaction intensity of selected family members of Arabidopsis…..…..90

Figure 3-4: ADF4 co-localizes with WRKY29 on WRKY29-targeted promoters……109

Figure 3-5: ADF can boost the transcription activation capability of interacted WRKYs……94

Figure 3-6: ADF4 can stabilize interacted WRKY exclusively……97

Figure 3-7: Bacteria growth assay of nuclear and cytoplasmic-exclusive complementation lines of ADF4……..99

Figure 3-8: ChIP-seq identifies of genome-wide target of WRKY29 and the enhancement of WRKY29 promoter bind by ADF……...101

Figure 3-9: Inspection on potential mechanism of ADF-WRKY interaction……104

Figure 3-10: A schematic diagram describing the nuclear-cytoplasmic function of ADF4 in immune regulation……107

Figure 3-11: Construction of Gateway vectors for multiple purpose……...111

Figure AA-1: NNES (Non-connected negative elements scanning) identification of course background……..120

Figure AA-2: Performance of NNES adaptive global thresholding and its prediction model (3D) ……..……....121

Figure AA-3: Visualized explanation of core ILEE algorithm…….122

Figure AA-4: Significant difference filter……..124

Figure AA-5: The mean and standard deviation (STD) of gradient magnitude of ground noise is directly proportional to the STD of noise……..…125

Figure AA-6: The ratio of x-y unit and z unit influences the proportional coefficient of σ_{Noise}-μ_G and σ_{Noise}- σ_G relationship……...126

Figure AA-7: Determination of global gradient threshold……..127

Figure AA-8: The impact of *K* and the training for K_2 estimation……..128

Figure AA-9: The stability of ILEE and other classic image thresholding approaches for cytoskeleton segregation in confocal images……130

Figure AA-10: The visualized comparison of robustness of ILEE and other algorithms by segmentation accuracy……..131

Figure AA-11: The quantificational comparison of robustness of ILEE and other algorithms by segmentation accuracy……..133

Figure AA-12: The quantificational comparison of robustness of ILEE and other algorithms by index rendering stability……....134

Figure AA-13: The stability/robustness of ILEE and MGT in batch analysis of biological samples of Figure 2-6……135

Figure AA-14: The correlation of *occupancy* and *linear density*……136

Figure AA-15: The performance of ILEE on other type of biological sample……137

Figure AA-16. ILEE and human eye have different tendency to judge the topological structure of cytoskeleton, especially between two bright bundles……138

Figure AB-1: The technical route to construct the high-order mutant lines of ADFs……139

Figure AB-2: The scheme diagram describing the IP-MS based identification of ADF4 in vivo phosphorylation sites……..……..140

KEY TO ABBREVIATIONS

PTI: PAMP-Triggered Immunity

ETI: Effector Triggered Immunity

ILEE: Implicit Laplacian of Enhanced Edge

TF(s): Transcription Factor(s)

ADF(s): Actin Depolymerization Factor(s)

WRKY(W): WRKY transcription factor

Chapter 1: the plant immunity and the immune-regulatory function of cytoskeleton

(This chapter is adapted from Li and Day, 2019 and Li et al., 2020, published by the author.)

Chapter abstract

Throughout the lifespan, plants confront an endless barrage of pathogens and pests. To defend the biotic threats, plants have evolved a complex immune system responsible for surveillance, perception, and the activation of defense. These processes require the activation of host perception, the regulation of numerous signaling cascades, and transcriptome reprogramming, all of which are highly dynamic in terms of temporal and spatial scales. Towards defining how immune signaling is regulated, recent research has focused on the core mechanisms that underpin receptor-ligand interactions, phospho-regulation of signaling cascades, and the modulation of host gene expression during infection. Meanwhile, thanks to the expanded horizon facilitated by these studies, one of the major participants of the immune signaling – the plant cytoskeleton – has emerged as a critical regulator of the transport of the organelles, proteins, and chemicals that support plant defense signaling. However, the major aspects and particular mechanisms of the pro-immune functionality of the plant cytoskeleton are largely unknown. In this chapter, I will introduce the current knowledge on plant immunity, focusing the functionality of the cytoskeleton on the immune processes, as well as the strategies adopted by the pathogens to target the activity of the cytoskeleton. This led to the discussion of the frontier topics in this field of study, which greatly motivated my original studies described in *Chapter 2* and *Chapter 3* of the dissertation, on the immune function of the actin cytoskeleton and actin-associated proteins. In total, I will integrate the recent discoveries and hypothetical models, to present a dynamic portrait of plant immunity, focusing on my field of interest.

Plant Biotic Interactions

In natural ecosystems, most plants are resistant to most pathogens, a phenomenon whose mechanism is undoubtedly one of the holy grails in plant pathology – to understand and harness the ability of a plant to respond to, and successfully defend against, pathogen invasion (Staskawicz, 2001). Indeed, the abundance of host, pathogen, and climatic diversity provides a rich source of broad-spectrum resistance, the result of which is a naturally selected balance of genetically diverse plant and pathogen/pest populations. Therefore, epidemics in ecosystems are rare, and when they do occur, they are typically restricted to a specific geographical region, climate, or a combination of both. In the case of natural resistance, typically referred to as non-host resistance, the breadth of genetic diversity represented in the host population is often sufficient to limit infection(s), resulting in the evolution of what is referred to as non-adapted (Stam et al., 2014). Conversely, and what has become the basis for much of the research in modern molecular plant pathology, the selection for and enrichment of pathogens that are adapted to their host has resulted in the establishment of ecosystems where pathogen virulence and disease are more often the norms than the exception.

Plants begin and end their lifecycles in a single geographical location; however, the environment around plants is in constant flux. In response to these changes, and ultimately, to survive and thrive, plants must sense, respond, and adapt to an endless barrage of external perturbations – biotic and abiotic threats. Thus, it is not surprising that an emerging theme in plant pathology is the contribution and influence of the environment on immune system maturation (Chappelka and Grulke, 2016; Morris et al., 2017). To successfully respond to and defend against biotic threats, plants have evolved highly complex pathogen defense systems or surveillance networks, which functions similarly to the innate immunity of humans. The defense signaling acts cooperatively with numerous cellular processes, and together, the sum of these interactions imparts the ability

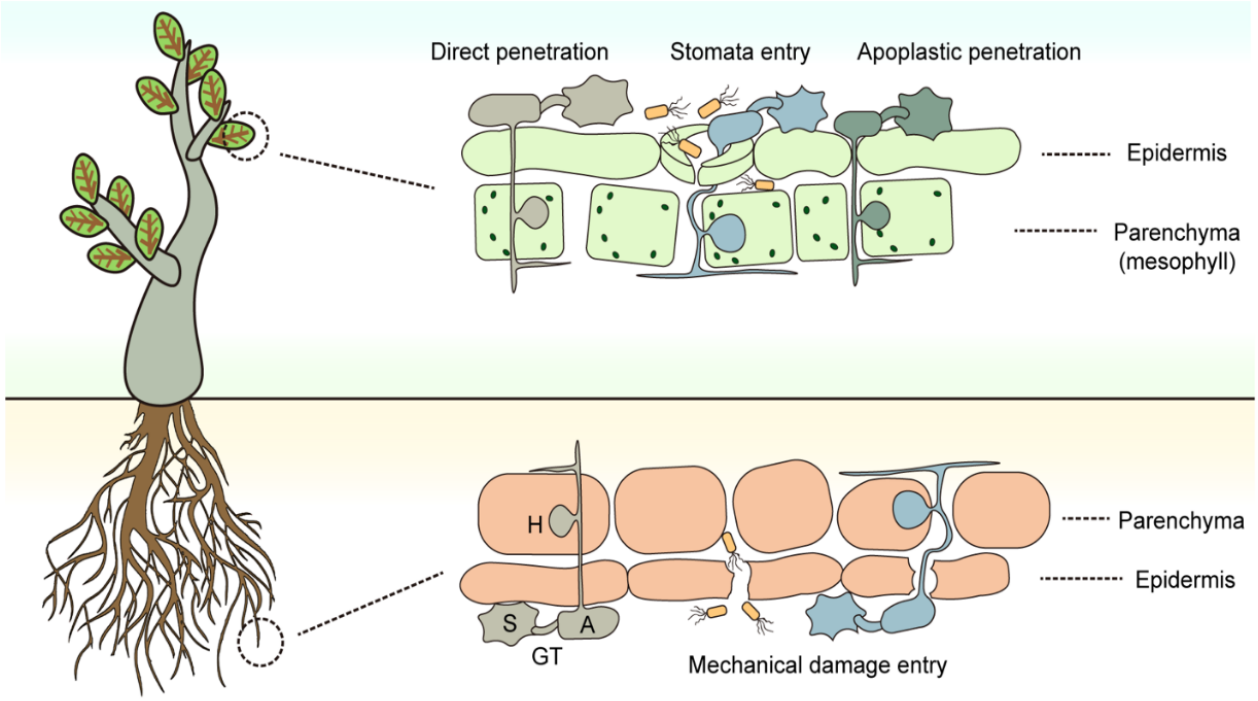

Figure 1-1: Invasion strategies by phytopathogens. To promote infection, both phyllospheric and rhizosphere pathogens must overcome physical barriers on the plant surface. Filamentous pathogens typically infect their host using the appressorium to invade living cells. During infection, the germinating spore (S) forms an extended tube-like structure (i.e., germination tube, GT), which then develops into an appressoria (A) that promotes the entry into plant. Appressorium can either directly penetrate into epidermis cells by breaking through the cuticle surface and cell wall, or enter through the apoplast, the space between cells. Additionally, wounds or natural openings (i.e., stomata) on the plant surface provide easy entry into the intercellular space. Once inside the host, filamentous pathogens use a root-like structure (i.e., haustoria, H) to obtain host-derived nutrients, resulting in the establishment of the pathogen-host interface. The invasion of bacterial phytopathogens, unlike filamentous pathogen, highly depends on natural openings to enter the plant host.

to recognize a vast array of biotic threats (e.g., pathogens, pests, viruses) and distinguish self from non-self (Sanabria et al., 2008). As described in greater detail below, underpinning the function and activity of the plant immune system is a complex network of preformed and inducible signaling processes, which provides unfettered access to both external and internal (i.e., systemic) cues.

During fungal colonization of plants, the transition from external to internal growth and proliferation begins with germination of a spore and formation of the penetration-specialized architecture

– appressoria (Yi and Valent, 2013; Ryder and Talbot, 2015). In short, this process enables "forced entry", or direct penetration, of the plant outer physical barriers, a common yet diverse invasion strategy among filamentous pathogens (see Figure 1-1). For instance, the model foliar powdery mildew pathogen *Golovinomyces orontii* uses its appressoria to forcibly invade into leaf epidermal cells by breaking the cuticle and cell wall (Braun et al., 2019). Such a strategy is also common in soilborne pathogens, including, for example, *Phytophthora sojae*, which invades the roots of soybean (Fawke et al., 2015). Alternatively, pathogens do not necessarily need to directly penetrate into a live cell in the very beginning; case-in-point, the oomycete pathogen *Hyaloperonospora arabidopsidis* (Coates and Beynon, 2010) penetrates the cuticle and grows into the apoplast, the space between the junction of two pavement cells (Underwood, 2012), which potentially benefits the pathogen by delaying the full engagement with plant immune system. As a point of strategy, while the "forced entry" model greatly expands the opportunity for filamentous pathogens to successfully invade the host, the "passive entry" mechanism (e.g., through natural openings or wounds) presents less of a challenge to the pathogen as a function of reduced physical barriers and defense response. One of such examples is the invasion of *Colletotrichum* species, which causes anthracnose diseases. Outside plant, they generate non-penetrative appressoria, from which undifferentiated germ-tubes extend and search for stomata to enter, resulting in host colonization via intercellular hyphae development (Latunde-Dada et al., 2002).

Of the numerous systems that have advanced our understanding of the processes underpinning appressorium-mediated penetration, the interaction between rice and the fungal pathogen *Magnaporthe grisea* illustrates one of the better illustrated examples of this virulence mechanism. As demonstrated using a combination of genetics-, cell biology-, and classical plant pathology-based methods, *M. grisea* initiates appressorium development upon the perception of the hydrophobic leaf surface environment, in combination with contact of the wax cuticle (Ryder and

Talbot, 2015; Anjago et al., 2018). Upon contact and assessment of the leaf surface environment by the developing fungus, physical penetration is mediated by the establishment and maintenance of cellular turgor pressure, which comes from elevated concentrations of glycerol in the appressoria, as well as a semi-permissive melanin barrier at the host-fungal interface (Chang et al., 2014; Ludwig et al., 2014). During this stage of infection, appressorial growth and development is facilitated by the assembly of a condensed septin-actin network, a mechanism hypothesized to enhance mycelia growth and trafficking during the maturation of pathogen infection (Van Ngo and Mostowy, 2019). In addition to the early stages of fungal development and infection, the pathogen secretes a battery of virulence-associated enzymes to promote infection, including cutinases, cellulases, and pectinases (Kebdani et al., 2010), which target host cell wall components to promote further ingress. In total, the integrity of the whole penetration-facilitating system of filamentous pathogen is a prerequisite of successful and efficient invasion. Indeed, mutants with reduced turgor pressure or an absence of cell wall degrading enzymes display reduced penetration capabilities (Auyong, 2015; Paccanaro et al., 2017; Tang et al., 2018).

In the case of phytopathogenic bacteria, the transition from epiphytic/saprophytic growth to infection is hypothesized to be induced by external signals, including those emanating from a combination of the host and environment (e.g., changes in humidity and temperature), as well as from microbial community (i.e., microbiome composition, quorum sensing, etc.) (Baker et al., 2010; Leonard et al., 2017; Xin et al., 2018). In the case of leaf-attached bacterial colonies, communities may persist as non-infective entities as a consequence of low surface humidity. Such “dormancy” on the host surface is mediated by a humidity-regulated quorum sensing system that inhibits the transition to an infection phase, as indicated by bacterial mobility, exopolysaccharide production, and pathogen secretion system maturation (Quiñones et al., 2005, 2005; Cheng et al., 2016). Once the stimulus is perceived by potential pathogenic microorganisms, as described in the case of the model bacterial phytopathogen *P. syringae* (Ortiz-Martín et al., 2010), the bacteria

enters infection phase. In short, this process coincides with the rapid expression of core pathogenesis regulons, including *hrp*/*hrc*, *hrpA*, *hrpL*, and *hrpR*. In turn, this leads to the activation of signaling associated with the production of key virulence factors, including toxins(Baker et al., 2010; Geng et al., 2012), and the induction of signaling responsible for the production of the type III secretion system (TTSS) (Tang et al., 2006). In another example for soilborne bacteria, *Ralstonia* solanacearum perceives oleanolic acid (Wu et al., 2015) and ferulic acid (Zhang et al., 2017) as critical host-released virulence inducive signals, potentially via PrhA-PrhR receptor complex. This is significant, because these compounds are directly released into the soil matrix, and *R. solanacearum*, like other soilborne pathogens, may induce transitions to pathogenesis and gain higher virulence before host invasion.

As a foundation describing molecular plant-pathogen interactions during host immune signaling and defense, it is important to clarify the status of pathogen virulence in advance of host infection. Current models portray pathogen virulence, in the most generalizable terms, as a process activated upon host contact. In this context, and herein, we too will define contact between a pathogen and the apoplast or living cell as “time zero” in the chronology of the activation of plant immunity. This leads to an essential question related to the entire process of plant immunity – *are pathogens already capable (i.e., competent) of interfering with immune signaling at time zero*? For bacteria, as discussed above, they are capable of entering the infection phase and activating the effector/toxin secretion systems before time zero. For filamentous pathogens, spore germination, *per se*, is a hallmark of the initiation of the infection phase, which activates a virulent secretome before penetration (Kleemann et al., 2012). Hence, it is reasonable to hypothesize that pathogens have already obtained the ability to inhibit the impending defense response by host before confronting with plant immune system. This temporal advance is critical for pathogenesis because it ensures that the secretion of effectors or other defense-inhibitory compounds to host is, at a minimum, simultaneous with pathogen perception, if not in advance.

Core signaling mechanism of plant immunity

In plants, local immunity describes a fundament concept founded on the basic principle that an independent live cell is immuno-totipotent – possessing the full capability of all aspects of the immune response, independent of additional signal input(s) from other host-associated components (Verdeil et al., 2007). Previous work has generalized a canonic model to describe local immunity with two primary nodes, namely PAMP-triggered immunity (PTI) and effector-triggered immunity (ETI). PTI, as mechanism of basal defense, is activated following host perception of microbial PAMPs (pathogen associated molecular patterns), the conserved organismal motifs required for the survival and lifestyle of the microbe (e.g., flagellin, chitin). As an immune response that best illustrates the initiation and integration of complex host signaling and innate immunity, PTI follows a classic cellular signaling model comprised of receptors, cascades, and defense executors. Here, we describe the temporal function(s) of each of these three components (i.e., receptors, cascades, and defense executors) as they correlate with the initiation of basal defense signaling (see Figure 1-2).

Plant pattern recognition receptors (PRRs) perceive a wide range of elicitors, including pathogen-derived cell wall/membrane components (e.g., peptidoglycan, chitin), pathogen-associated proteins (e.g., flagellin, effectors), and host-derived danger associated molecular patterns (DAMPs; e.g., cuticle). Though diverse, these receptors share certain features: they are single-transmembrane receptor-like kinases or receptor-like proteins, containing a leucine-rich repeat (LRR), LysM, EGF-like, or lectin domain for ligand binding within the apoplast (Boutrot and Zipfel, 2017). For most cases, evidence supports a general mechanism wherein a core receptor and their associated kinases form the primary receptor complex, in association with additional regulators, mediate pathogen recognition and the initiation of downstream signaling. Herein lies one of the key remaining questions: *How fast does PRR activation occur following pathogen perception?*

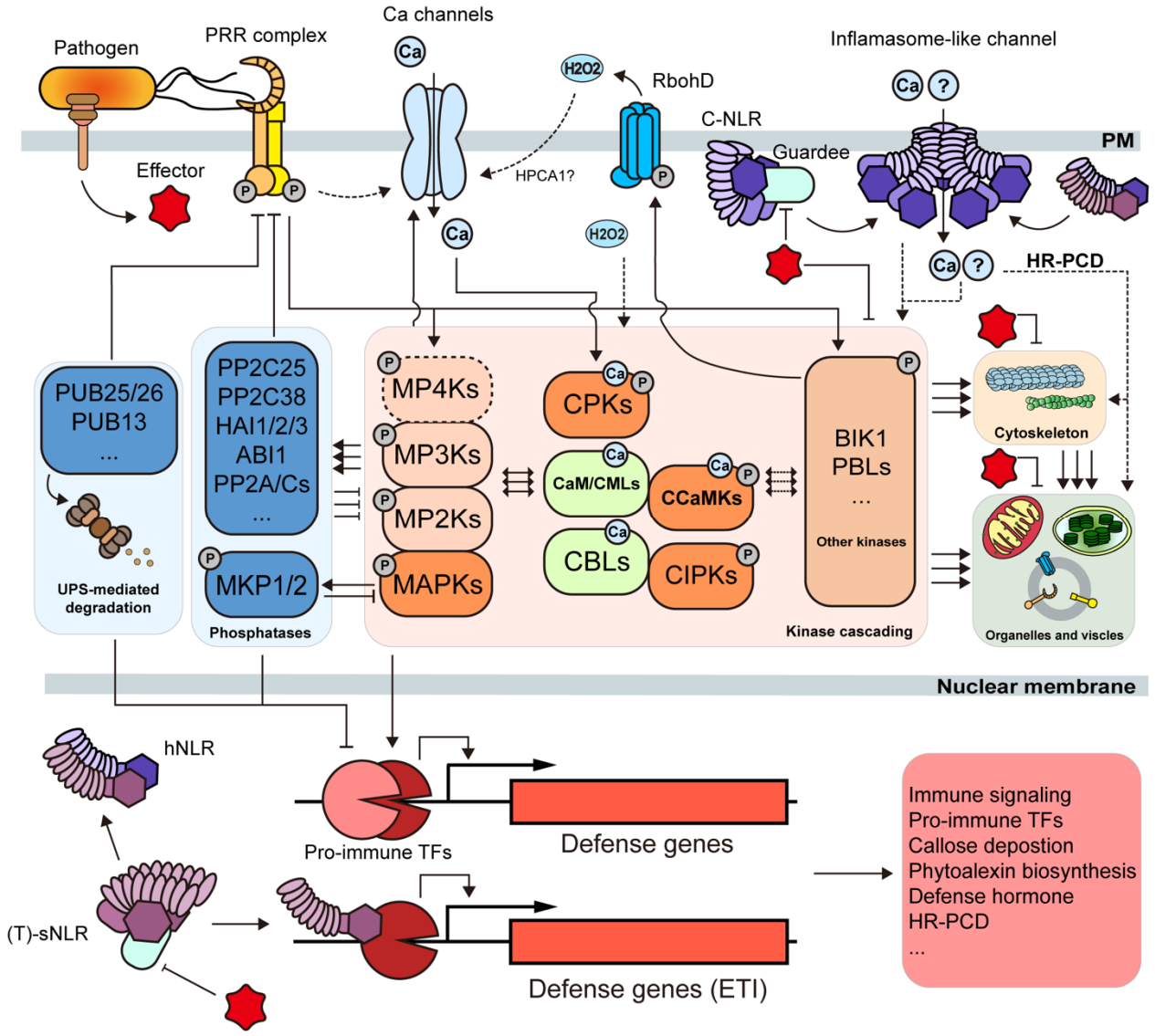

Figure 1-2: A schematic map of plant local immunity. Invasive pathogens are recognized by plant PRR (pattern recognition receptor) proteins, which results in the activation of broad spectrum of downstream signaling, such as Ca^{2+} influx, the accumulation of H_2O_2 generated by RbohD (respiratory burst oxidase homolog protein D), and kinase cascading, which includes signaling pathways mediated by MAPKs, CPKs, and other additional kinases. As depicted, various kinases may also engage in a highly coordinated crosstalk during signal amplification and attenuation. These immune signals, amplified by kinase cascades, trigger a variety of defense responses, including cytoskeletal remodeling, activation of defense function in organelles, and transcriptional reprogramming through the activity of pro-immune transcription factors (TF). In total, the sum of this highly coordinated signaling functions to promote plant defense signaling and pathogen resistance. Concomitant with the activation of defense signaling, the attenuation of key immune pathways occurs, a process hypothesized to function in rebalancing of immunity and growth pathways occurs. To cope with plant immunity, pathogens have evolved mechanisms to deliver effector proteins into plant cell, which target and inhibits immune signaling, as well as to subvert immunity through targeting of critical host cellular processes…

Figure 1-2 (cont'd) … In response, plants utilize NLR (nucleotide-binding leucine-rich-repeat proteins) proteins to recognize certain effectors through sensing pathogen modification of surveilled host processes (i.e., guardee), resulting the activation of robust immune signaling and cell death (i.e., ETI; effector-triggered immunity). As a potential mechanism to activate ETI, cell membrane (PM)-associated NLRs (in most instances, possessing a coiled-coil domain, i.e,, C- NLR), can form a channel-like structure following activation, which presumably functions to mobilize additional defense signaling molecules. NLRs containing a Toll/interleukin-1 receptor- like domain (T-NLRs) at the C-terminus are typically associated with a nuclear subcellular localization, and in large part, function as sensors (i.e., sNLR) that activate helper NLRs (hNLR) to form channels within the PM. As an additional hypothesized mechanism, activated nuclear NLRs may regulate specific defense genes functioning in ETI, by interacting with TFs. Dashed in indicate putative/hypothesized processes.

While no technical approaches currently exist which can directly measure the speed of PRRs activation, this question can be answered by correlating the timing of measurable downstream outputs, such as the generation of apoplastic reactive oxygen species (ROS) – one of the earliest measurable defense responses (Lehmann et al., 2015). In Arabidopsis, the PTI-triggered apoplastic ROS burst is generated by respiratory burst oxidase homolog protein D (RBOHD) (Kadota et al., 2015), a plasma membrane (PM)-associated NADPH oxidase that generates H_2O_2 as secondary signaling messenger. As one example of the link to PRR signaling complex activation, RBOHD is phosphorylated and activated by BIK1 (*Botrytis*-induced kinase 1), a core signaling kinase within the FLS2 (flagellin sensitive 2)-associated PRR complex (see Figure 1-2; Kadota et al., 2014). As an indicator of the timing of this response, the rate of ROS accumulation (i.e., d[ROS]/dt) reaches saturation at approximately 3 minutes after flg22 (elicitor that activates FLS2) stimulation (Nühse et al., 2007), with complementary data demonstrating a maximum accumulation approximate 25 min following *P. syringae* infection (Smith and Heese, 2014). Taken together, the initial activation of PRRs occurs within the first few minutes following pathogen perception (Figure 1-3); the rapidity of this process further illustrates the role of ROS as second messenger in downstream immune signaling, including regulating Ca^{2+} influx.

Once PAMP recognition and PRR associated signaling events are activated, the immune signal is handed off to downstream signaling processes, which serves to not only amplify the initial

signal, but importantly, functions as a mechanism to regulate signaling specificity and the activation of defenses that are appropriate to the nature of the stimulus. To accomplish this, plants utilize a complex series of phosphorylation-dependent signaling cascade, the best characterized of which include mitogen-activated protein kinases (MAPK) (Meng and Zhang, 2013) and calcium-dependent protein kinase (CPDK; aka CPK) relays (Singh et al., 2017). To date, one of the best characterized signaling pathways is flg22-triggered PTI, wherein MAPKs are rapidly activated following phosphorylation by FLS2-associated signal regulators – a cascade from MAPKKK3/5 to MAPK3/4/6 (see Figure 1-2; Mithoe and Menke, 2018). As an illustration of the rapidity of this process, it has been demonstrated that flg22-induced signaling occurs within ~5 minutes following ligand perception as determined by MAPK3/4/6 phosphorylation; maximal phosphorylation is believed to peak at ~30 minutes post elicitation (see Figure 1-3; Frei dit Frey et al., 2014).

Simultaneous with MAPK cascading, CPK-dependent signaling is induced by Ca^{2+} influx, a process that is initiated by gated Ca^{2+} channel(s) downstream of PRRs (also discussed in Section III). While direct evidence is largely absent which describes the dynamic status of CPK phosphorylation during PTI, the influx of cytosolic Ca^{2+} can be used as an indirect index of CPK activity. Indeed, the accumulation of cytosolic Ca^{2+} obtains maximum speed (i.e., $d[Ca^{2+}]_{cyt}/dt$) in 1 minute after elicitor treatment; the Ca^{2+} concentration reaches the peak in 3 minutes post-treatment (Qi et al., 2010). Because CPKs are directly activated by elevated concentration of cytosolic Ca^{2+} without intermediate kinases, and CPKs, Ca^{2+} channels, and RBOHD form a positive feedback loop (see Figure 1-2), the activation of CPKs is supposed to be slightly faster than MAPKs. This hypothesis is supported by evidence demonstrating that the rice *Os*CPK18 functions as direct upstream regulator of *Os*MAPK5 (Xie et al., 2014), which further indicates that CPK-MAPK crosstalk is involved in PTI signaling. In total, these data support a model whereby MAPKs and CPKs work synergistically (Tena et al., 2011), yet non-redundantly (Li et al., 2018) as pro-immune activators.

Following MAPK and CPK signaling, the next step is the activation of defense executor proteins, a process leads to nuclear-based transcriptional reprogramming, induction of defense hormone accumulation and signaling (Verma et al., 2016), cytoskeleton/organelle remodeling (introduced above), regulation of the secretome and cell wall/apoplast composition (Bellincampi et al., 2014), and cellular motion (e.g. stomatal closure; Arnaud and Hwang, 2015). As key outputs of defense, the development of each of these cellular processes can be briefly categorized into two distinct phases. The first phase is the fast, pre-transcriptional defense responses, which are often directly activated as a byproduct of the basal immune signaling cascade. For example, RBOHD, described above, activates a robust ROS burst in the apoplast via the direct activation of PRR complex assembly and activation (Kadota et al., 2014, 2015); as noted above, the timing of this response is detectable within 3 minutes of elicitation. Similar rapid signaling responses are also observed in the case of PM-associated ion channels (Jeworutzki et al., 2010). As another example of rapid signaling through PTI executor, PAMP-triggered actin remodeling illustrates the integration of PRR function with broader signaling platforms, as illustrated by the detection of changes in microfilament remodeling within 5-15 minutes following PTI elicitation (Henty-Ridilla et al., 2014). While the full mechanism(s) underpinning this response is unknown, we posit that it involves the regulation of actin depolymerizing factors (ADFs) by cytosolic kinases at the downstream of PRRs, as well as H_2O_2 and phosphatidic acid (Porter et al., 2012; Li et al., 2015, 2017a). While still largely hypothetical, this model is in agreement with an abundance of data describing fast responses mediated by changes in actin filament organization, including the activation of downstream immune signaling processes.

In order to initiate a large-scale and long-term output of defense, signaling next proceeds to the phase of transcriptional activation of sustained and robust defense processes (Lewis et al., 2015). As indicated by its classification, the foundation of this stage of immunity lies in the activation of stress-responsive transcription factors and the gene networks under their control. In brief, key

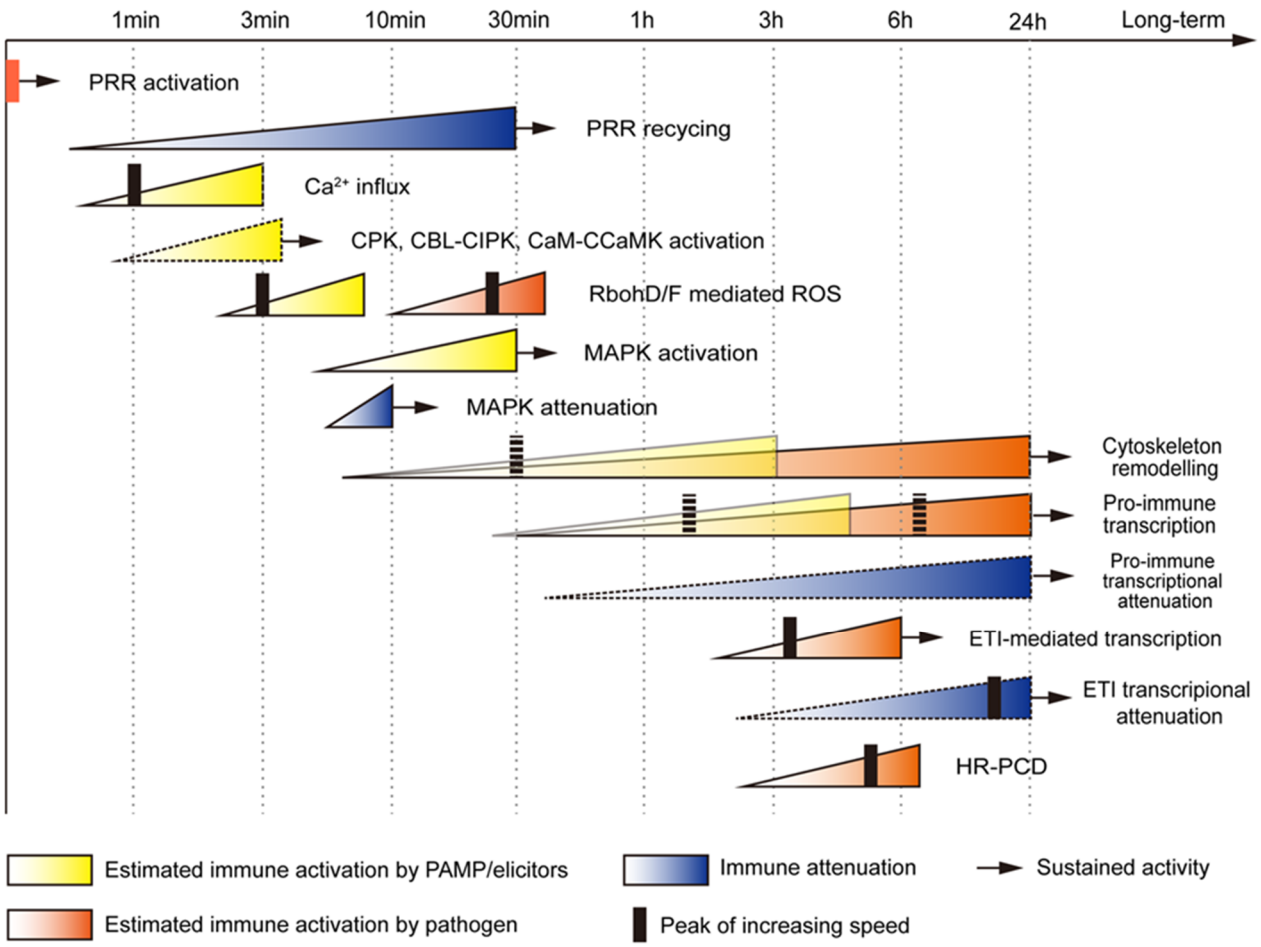

Figure 1-3: Dynamics of signaling processes associated with local immunity. The signaling processes associated with local immune signaling can largely be described in a temporal fashion; for the sake of comparison, we suppose "Time 0" = PRR activation. To estimate the signaling dynamics (i.e., timing of initiation, sustained saturation, peak of increasing speed, and termination), published data recording the development of immune processes following elicitor treatment or pathogen infection are collected, analyzed, and translated into this figure. Dashed lines in indicate estimation without direct evidence.

regulators of this includes AP2/ERF, bHLH, bZIP, MYB, NAC, and WRKY (Tsuda and Somssich, 2015). Here, as a result of MAPK activation, the phosphorylation of defense transcription factors by MAPK significantly contributes to plant immunity. For example, in response to necrotrophic fungal pathogen *Botrytis cinereal*, MAPK3/6 phosphorylates WRKY33 within 0~12 hours post-infection (hpi), which has been shown to regulate the overall resistance signaling within 6~24 hpi (Mao et al., 2011). Interestingly, as an example of the dynamic control and specificity of signaling,

the *WRKY33* mRNA is up-regulated in response to flg22 or HrpZ (a bacterial elicitor) elicitation at ca. 1 hpi and subsequently down-regulated at 4 hpi, suggestive of a negative feedback loop to control signaling (Liu et al., 2015). As such, a single PAMP treatment does not necessarily reflect the true dynamics of TF activity, because pathogens possess multiple elicitors (e.g., PAMPs, effectors) that result in the stimulation of various synergistic signaling cascades. In this regard, the overall dynamics and pattern of defense-induced transcription cannot be measured exclusively by the early (ca. minutes to hours) events, but rather, must be evaluated over the duration of the interaction, which can last days or longer. Thus, as illustrated in Figure 1-2 and Figure 1-3, the activation of immunity is not a sequential series of events, but rather, represents a complex network of processes, each of which can be activated or attenuated multiple times during the host-pathogen interaction.

Another important aspect of plant immunity is Effector-triggered immunity (ETI), a robust and sustained pattern of immunity activated following perception of pathogen-secreted effector proteins. As an additional layer of the immune surveillance platform, ETI resembles PTI in many regards, such as the involvement of MAPK signaling cascades and defense gene activation. However, distinct from PTI, ETI results in the activation of an apoptosis-like cell death (aka hypersensitive response (HR); Balint-Kurti, 2019), a fast process hypothesized to result in an abrogation of pathogen proliferation. As estimated by the dynamics of electrolyte leakage (indicating cell death) during HR, full intensity of ETI occurs within 2~6 hours after inoculation of avirulent (containing effectors that triggers ETI) bacterial pathogens (Mackey et al., 2002, 2003). Similar to such dynamic pattern, the transcriptome reprogramming during ETI reaches the maximum speed during the same period of time (Mine et al., 2018), indicating that ETI is a fast-acting immune response that may overcover the development of basal defense.

In terms of its mechanism, ETI relies on the function of host resistance (R) proteins to survey the

cell for perturbations, through what is referred to as the Guard Hypothesis (Biezen and Jones, 1998). As highlighted in reviews by Dangl and Jones (Jones and Dangl, 2006) and Chisholm *et al*. (Chisholm et al., 2006), the Guard Hypothesis posits that R protein "guards" another host derived protein (guardee), and when a guardee is modified (e.g., cleaved, phosphorylated, etc.) by a pathogen-secreted effector, its associated R protein recognize such modification and triggers downstream signaling. Most of R protein belongs to nucleotide-binding site leucine-rich repeat (NB-LRR or NLR) protein family, which is also the best studied R protein architecture (Monteiro and Nishimura, 2018). According to their distinguishing feature of the structure and activity, NLR proteins have been historically divided into two subgroups, based on the amino-terminal presence of either a coiled-coil (CC) domain or a domain with similarity to the Toll/interleukin-1 receptor (TIR) family of proteins. In total, different domains (e.g., TIR/CC, NB, and LRR) of NLR provide abundant interaction interfaces, which not only supports intramolecular interactions that inhibit NLR activation at the absence of corresponding effector, but also serves as intermolecular adapters to form NLR heterodimers that regulates ETI with higher order of flexibility (Sukarta et al., 2016). Directly related to this feature is the genetic evidence that certain extra downstream NLR(s) may be commonly required for ETI activation mediated by various NLRs (Adachi *et al*., 2019). This leads to a helper-sensor model where a "sensor" NLR (sNLR; cesari et al., 2014) perceives the existence of avirulent effector and activates a "helper" NLR (hNLR; Bonardi et al., 2011), which next processes ETI signaling pathway. Such model potentially explains why NLRs form heterodimer and why ETI mediated by various R protein shares a unique pattern. However, one of the key questions that remains in ETI is: *How does activated NLR protein function in ETI initiation?*

Recently, a series of publications offers a mechanistic insight into the biochemical function of activated NLR proteins. To explore the topic, Wang and colleagues (Wang et al., 2019, 2019) inspected the protein structure of activated NLR ZAR1 (HOPZ-activation resistance-1) through a

combined approach of cryo-EM based modeling and analysis. In brief, the study demonstrated that ZAR1 presents a pentameric-like structure, forming a general funnel shape within the PM . Related to its function to activate programmed cell death, this conformation is easily associated to mammalian inflammasome complexes, which serve as a cytosolic catalytic center to activate downstream apoptosis (Sharma and Kanneganti, 2016). However, the PM-localized ZAR1 differs from cytosolic inflammasomes with respect to its subcellular localization, which suggests a distinguishing function of ZAR1 as a massive channel that mediates influx of apoplast components (including Ca^{2+}) and leakage of cytosol and trigger the downstream signaling of ETI. Interestingly and related to this, co-expression of NAIP (inflammasome structure protein that resembles sNLR and recognize animal PAMP), $RPS4^{TIR}$- NLRC4 (inflammasome structure protein that resembles hNLR, and fused with TIR domain of RPS4), and corresponding PAMP (conceptually equal to “effector” in plant immunity) in *N. benthamiana* can trigger HR-like symptoms (Duxbury, 2016), which suggests that formation of the inflammasome in plants is sufficient to trigger ETI, yet the downstream signaling events in animals and plants may vary.

Hence, a general picture of ETI can be further clarified if the sensor-helper model is combined with the hypothesis that NLR functions as a PM localized channel. As described by Jubic and colleagues (Jubic et al., 2019), while some NLR, such as ZAR1, can both perceive effector activity and form up an active pentamer channel on the PM, other NLRs (i.e., absolute sNLR) does not have the second capability due to the lack of corresponding interaction interfaces or PM localization. In this case, an hNLR to be activated by sNLR is required for the assembly of PM-localized channel to activate ETI. Howbeit, it is still not clear whether the vast material transport mediated by the NLR channel is the major process responsible for ETI. Since some NLRs have additional biochemical activity, such as regulating TFs in the nucleus (Sun et al., 2020), it is possible that activated NLR can initiate several relatively independent signaling pathways the synergistically contributes to the development of ETI.

Immune attenuation: rebalancing growth versus defense

The energy distribution of growth versus defense requires a constant balancing of signaling processes, including the simultaneous activation and attenuation of processes that share considerable overlap. Quite obviously, plant defense signaling following pathogen perception requires the rapid engagement and activation of a broad range of immune signaling processes, as described above. At the same time, in the absence of pathogens, plants redirect a considerable amount of energy to processes which downregulate immune signaling (Huot et al., 2014). Thus, the attenuation of immune signaling is a critical process of self-defense which likely evolved as a mechanism to protect the host from the ill effects of hyper-activated defenses that down-regulates growth.

In contrast to the events associated with the activation of pro-immune signaling, our current knowledge of con-immune signaling is relatively limited. What we do know, however, is that much like immune activation signaling, MAPK cascade also plays an essential role in this process and represent one of the best characterized con-immune signaling mechanisms known. In Arabidopsis, a well-illustrated example of immune attenuation lies in our understanding of signaling mediated by MAPK3/6, which is activates its own inhibitory, MAPK phosphatase 1/2 (MKP1/2; Jiang et al., 2018). In a detailed and elegant series of temporal gradient analyses focusing on the dynamics of MKP1 activity, it was revealed that MKP1 phosphorylation by MAPK6 is saturated at ~10 min following PAMP treatment, resulting in the stabilization of MKP1 and an increase in MPK1 protein levels (Jiang et al., 2017b). Corelated to this observation, *MPK1* and *MKP2* mRNAs are nominally upregulated (< 2-fold) in response to biotic stress perception; we surmise that this illustrates a relatively low impact of transcriptional regulation on MPK abundance. Besides MAPKs *per se*, MKPs may actually dephosphorylates a wide spectrum of immune signaling substrates, as evidenced by the fact that MKP1 regulates thousands of MPK6-independent pro-immune

transcriptions within 90 min after flg22 elicitation (Jiang et al., 2017c). Moreover, and consistent with the role for MPK1/2 as broad regulators of immune attenuation, it is noteworthy that previous work has demonstrated that MPK1/2 are negative regulators of defense against biotrophic (e.g., *R. solanacearum*) and hemi-biotrophic (e.g., *P. syringae*) pathogen, whereas MKP2 is a positive regulator against necrotrophic (e.g., *B. cinerea*) pathogens (Lumbreras et al., 2010; Anderson et al., 2011). Taken together, these data illustrate that defense attenuation facilitates host immune-totipotency against full spectrum of pathogens.

In addition to MKPs, other protein phosphatases (i.e., PP2A/Cs) also function as known contributors of counteracting kinase activity in immune signaling, and as such, play a substantial role in immune attenuation (Withers and Dong, 2017). For example, recent work has demonstrated that a group of PP2Cs (i.e., HAI1/2/3) quench MAPK3/6 downstream of flg22 triggered ABA signaling – a key virulence mechanism utilized by pathogens to manipulate immune signaling (Mine et al., 2017). Likewise, Arabidopsis AP2C1 (aka PP2C25) dephosphorylates MAPK4/6, which modulates JA-and SA- associated immune signaling. In similar mechanisms, additional kinases also regulate the activation of PP2A/Cs, including the key PTI signaling regulators CPK6, BIK1, and BAK1 (Brandt et al., 2012; Segonzac et al., 2014; Couto et al., 2016). However, evidence indicating phosphatase targets of other immune signaling components, such as receptors, enzymes, channels, and TFs, is still lacking, illustrating a general knowledge gap in the breadth of engagement by the mechanism of immune attenuation.

Another important mechanism for immune signaling attenuation is the degradation of immune signaling components, a process that is typically mediated via the ubiquitin-proteasome system (UPS). In brief, UPS functions through E1, E2, and E3 ligases, of which E1 and E2 energize and load ubiquitin onto the proteasome complex, with E3 function to physically guide target specificity (Sharma et al., 2016). As a common mechanism in plant immune signaling, several well-

characterized examples of ubiquitin-mediated attenuation exist. For example, FLS2 is targeted by the U-box E3 ligases PUB12/13, resulting in the degradation of FLS2 following flg22 stimulation (Lu et al., 2011). As an illustration of the specificity and rapidity of this response, it was further demonstrated that physical association of PUB13 with FLS2 is initiated at ca. 30 seconds post FLS2 activation, indicating that PUB12/13 promotes rapid quenching of immunity. In contrast, LYK5, a membrane-associated receptor kinase responsible for chitin perception, is also targeted by PUB13, but the activation of LYK5 results in its dissociation from PUB13 and enhances LYK5 accumulation (Liao et al., 2017). In another example, the immune kinase BIK1 is ubiquitinated by U-box E3 ligases PUB25/26, but such process is inhibited by the hetero-trimeric G-protein complex XLG2/3-AGB1-AGG1/2 when BIK1 is inactive (Liang et al., 2016). Upon activation of BIK1 (i.e., in response to PTI elicitation), the XLG2/3- AGB1-AGG1/2 inhibitory complex dissociates, releasing unblocked BIK1 for UPS mediated-degradation (Liang et al., 2016; Wang et al., 2018).

Given that the proteasome exists within the cytosol, nucleus, and vacuole, it is a reasonable assumption that free, soluble, proteins are targeted to the proteasome via simple diffusion processes. However, this is not the case of PM-associated proteins, which are typically anchored through a variety of mechanisms, including transmembrane domains, post-translational modification, as well as via association with PM-resident components. In this regard, PM-associated immune signaling components, such as FLS2, BAK1, SERK1, CERK1, LYK5, PERP1, and SlCf-4, all require endocytosis-based mechanisms as a means to regulate recycling and or degradation (Claus et al., 2018). In a general sense, the constitutive endocytosis of membrane components serves as a recycling mechanism to ensure that immunity is maintained in signaling-competent state. As a mechanism describing the naïve and activated recycling of immune receptors, the example of flg22-triggered FLS2 endocytosis is one of the best characterize models (Robatzek et al., 2006; Mbengue et al., 2016). As observed, following flg22 elicitation, the majority of FLS2

(GFP-tagged FLS2) was internalized from the PM to cytosolic vesicles within 20-40 minutes following flg22 treatment. As an illustration of immune attenuation and the regulation of PTI, during this same time, *de novo* synthesized FLS2 was not replenished at the PM. Instead, a marked induction in *FLS2* transcription was observed, indicating that PRR endocytosis is an approach of immune regulation, in support of UPS, to maintain the equilibrium of immune signaling.

As a final example, the negative regulation of pro-immune transcription represents a key component of the defense signaling network attenuation. Just as immune activation requires the induction of TF-mediated gene expression, so does immune attenuation. Among the best example(s) of this process is illustrated by the activity of the plant-specific family of WRKY transcription factors, known for their broad roles in signaling processes associated with both abiotic and biotic stress (Tsuda and Somssich, 2015; Hussain et al., 2019). For example, Arabidopsis WRKY18 and WRKY40 are rapidly induced following *P. syringae* DC3000 and *G. orontii* perception, yet they function as synergistic negative regulators of resistance in response to both pathogens (Xu et al., 2006; Pandey et al., 2010). Using a series of ChIP-seq and RNA-seq approaches, it was further revealed that WRKY18 and WRKY40 possess broad transcriptional regulatory (presumably inhibitory) functions over defense genes during the early activation of PTI (Birkenbihl et al., 2017). Taken together, these studies indicate that certain "WRKY sub-regulatory networks" may serve as a mechanism to prevent over-induction of immunity, through balancing the in/activation of transcription following pathogen perception. Related to this hypothesis, Moore and colleagues (Moore et al., 2011) provided a similar network perspective, proposing a transcription pulse model to describe transcription cascading in plant immunity. In short, this posits that the expression of TFs in different temporal nodules display consecutive cyclical bursts, with sharp up- and down-regulated oscillations over the course of the lifecycle, a process regulated in part by UPS-mediated degradation of transcription activators in the nucleus. Indeed, such a mechanism is required for the degradation of activated NPR1, as well

as the enrichment of pro-immune TF inhibitors, including MYC2-induced *JAZ* expression.

The immune functionality of Plant cytoskeleton

There are two major classes of the cytoskeletal network are found in higher plants (Figure 1-4). The first, microfilaments (MF), commonly referred to as the actin cytoskeleton, are formed by the polymerization of globular (G)-actin into filamentous (F)-actin, a process in plants that requires the function of more than 75 actin binding proteins (Figure 1-4A) (Day et al., 2011). Actin is responsible for functions ranging from cytoplasmic streaming (e.g., movement of organelles) and cell division, to trafficking and endocytosis. The second, microtubules (MT), are comprised of a complex array of α/β-tubulin heterodimers, a network that is typically associated with cell growth and long-distance intercellular movement and communication (Figure 1-4B) (Brandizzi and Wasteneys, 2013). Both MF and MT exhibit a remarkable degree of rapid, seemingly random yet highly specific, dynamism, represented by tremendous rates of polymerization and depolymerization. Together, these patterns of cytoskeletal organization yield a highly dynamic and tightly regulated framework that connects the intercellular components of the cell to an endless suite of microenvironments and physiological processes. The eukaryotic cytoskeleton engages a variety of signaling events, including those associated with cell division and development, organelle movement, vesicle trafficking, and immunity (Porter and Day, 2016; Elliott and Shaw, 2018). As a function of the plant immune system, an abundance of data supports roles for the cytoskeleton in at least two key aspects of the immune response: 1) establishment and maintenance of signaling-competent microenvironments, and 2) cellular trafficking (organelle, proteins, and small molecules). Below, we highlight current research in each of these areas, discussing the role of each of these in immunity and the function of each as linkages between immune signaling and the dynamism of the host cytoskeleton.

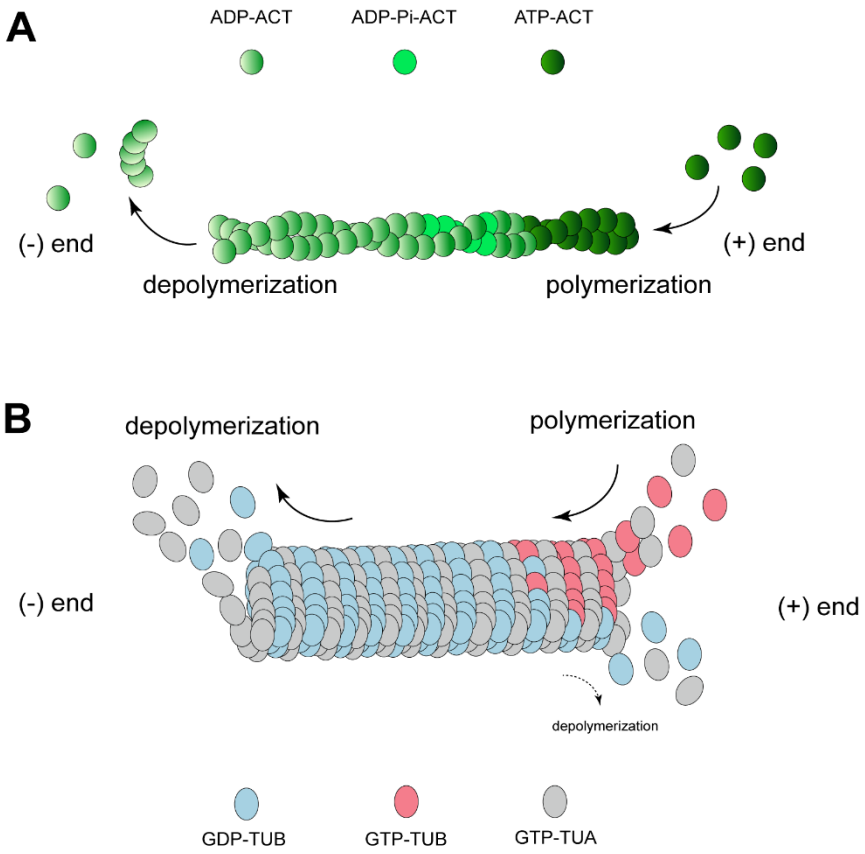

Figure 1-4: Schematic diagram of cytoskeleton polymerization/depolymerization (treadmilling). A, Microfilament treadmilling. G-actin is dynamically polymerized onto the growing F-actin strand. The (+) end is defined as the site where polymerization dominates, and the (-) end as where depolymerization dominates, while spontaneous polymerization/depolymerization may occur on both sites. Actin polymerization is achieved through loading ATP-associated G-actin to the end of F-actin, while depolymerization occurs through destabilization of ADP-associated actin. **B**, Microtubule treadmilling. The (+) end is defined as the site where both polymerization and depolymerization are very active, with polymerization dominating. Conversely, on the (-) end, tubulin is relatively stable with dominant depolymerization occurring. α-tubulin (TUA) and β-tubulin (TUB) form a heterodimer as the basic unit of the polymerized microtubule. TUA is constitutively bound to GTP; TUB binds the growing MT filament as GTP-bound monomers, and tends to disassociate from the filament when bound to GDP.

The cytoskeleton as a molecular and cellular scaffold of plant immunity

In a typical plant cell, the vast majority of the cytoskeleton stretches from the cytosol to attachment points at or near the plasma membrane (PM). This is significant, as the PM is regarded as one of the key signaling interfaces between the host and pathogen, supporting the function of two primary classes of immune receptors: PRR complexes and the coiled-coil type NB-LRR (CC-NLR)

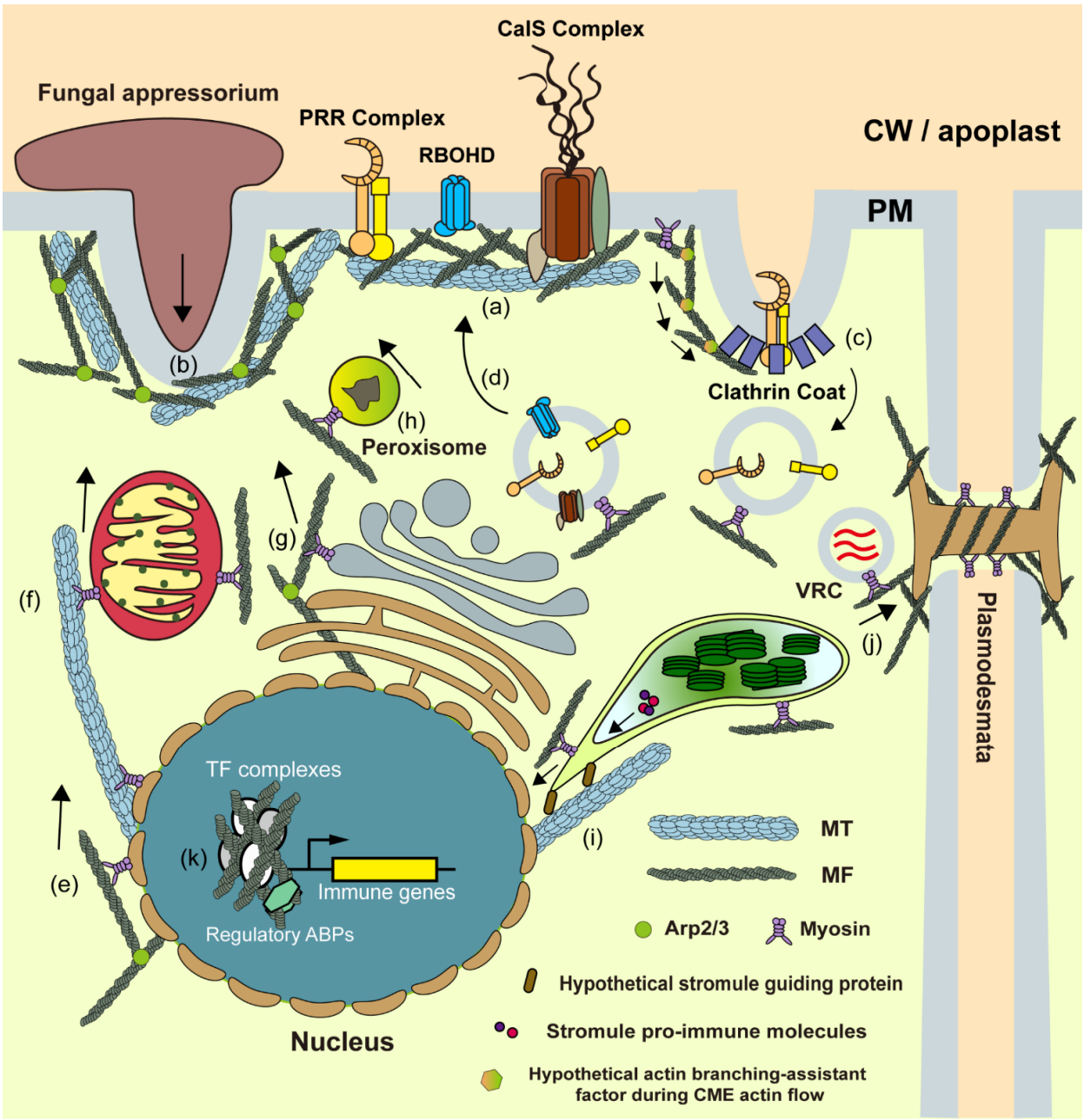

Figure 1-5: The versatility and involvement of the plant cytoskeleton in immunity. Plant MF and MT are involved in multiple processes during the immune response. (a) The cytoskeleton provides the physical attachment, as well as specialized microenvironments, to numerous PM-associated immune processes (e.g., PRR complexes, RBOHD, and CalS complex) and is required for full functionality of these immune processes. (b) The cytoskeleton aggregates at the interaction interface of fungal pathogen penetration, a process that is even more striking in avirulent strains. The cytoskeleton is also required pro-immune cellular trafficking, a process that is associated with the transport immune-functional molecules, through the action of endocytosis (c), PM and apoplast secretion (d), transport of organelles (e, f, g, h), plastid stromules (i), as well as cell-to-cell trafficking through plasmodesmata. (j) Virus replication complex (VRC) can hijack cytoskeleton and transports to adjacent cells through plasmodesmata. (k) As a less-characterized mechanism of plant immunity, actin is also involved in the transcriptional regulation of immune signaling events within the nucleus, potentially through aiding in the formation of a regulatory complex consisting of transcription factors and chromatin. Arrows are shown to indicate the directionality/movement of corresponding cellular components.

resistance proteins. Thus, it is not surprising that the cytoskeleton-PM interface is also a key component of the signaling processes associated with receptor activation, mobilization, and signaling transduction. Indeed, as a scaffold for many of these PM-associated processes, recent work has revealed that the plant cytoskeleton selectively interacts with – either directly or indirectly – numerous membrane-localized receptors associated with immunity and signaling plant defense.

In Arabidopsis, the PM localized PRRs FLS2 (flagellin receptor) and BRI1 (brassinosteroid receptor), interact with BIK1 to form a co-receptor complex to initiate downstream signaling (Couto and Zipfel, 2016). Following ligand binding, activated PRR complexes aggregate into distinct nanodomains within the PM, where they function in immune signaling activation (Keinath et al., 2010). Indeed, a recent study demonstrates that FLS2-BIK1 and BRI1-BIK1 complexes localize in distinct nanodomains within the PM, where they further associate with different proteins required for downstream signaling (Bücherl et al., 2017). In the case of BRI1-BIK1, the nanodomain has been shown specifically interact with the MT network. This finding is significant as it provides experimental evidence that plant receptor kinases, including immune receptors, form functional complexes with the plant cytoskeleton to activate downstream signaling associated with immunity. In an additional study, it was further demonstrated that disruption of actin filament organization leads to the generation of a relatively enhanced ROS burst response following flg22 perception by FLS2 (Sun et al., 2018). In total, these studies were among the first to provide evidence supporting the hypothesis that cytoskeletal organization – and the physical interactions between PRR complexes and actin – are required for maintenance of appropriate levels of immune activation and signaling.

While conclusive data demonstrating that the plant cytoskeleton directly interacts with individual immune receptors is lacking, an abundance of data in mammalian systems does exist. For example, the nucleotide-binding oligomerization domain protein 1 (NOD1), the PRR responsible

for perception of p G-d-glutamyl-meso-diaminopimelic acid (iE-DAP), requires F-actin for proper PM localization. Further, the interaction(s) between NOD1 and actin serves as an immune interface which influences actin-remodeling and control of downstream signaling (Kufer et al., 2008), including the phospho-dependent activation of the actin depolymerizing factor cofilin (Bielig et al., 2014). Similar to the activation of NOD1, the mammalian muramyl dipeptide receptor NOD2 is also recruited to the PM through its association with actin (Legrand-Poels et al., 2007). Using a pharmacological-based approach, these studies also demonstrated that following application of cytochalasin-D, an inhibitor of actin polymerization, both NOD1 and NOD2 signaling are activated, providing strong support for the hypothesis that the actin remodeling (including depolymerization) of PM-associated F-actin is likely a physical trigger of NOD1/2 signaling. Taken together, data from both plant and animal systems support the hypothesis that the cytoskeleton provides the necessary microenvironment to sustain the functionality of immune receptor complexes (Figure 1-5, (a)), and based on this, we hypothesize that the actin cytoskeleton is a guardee of PM-localized PRRs.

The actin cytoskeleton is required for turnover of PM-localized PRRs

During both PTI and ETI, the turnover of activated signaling complexes is mediated by receptor endocytosis, a process that functions not only to protect the plant from constitutive activation of defenses (i.e., autoimmune response), but also to support the surveillance function of the immune system (He et al., 2017). In the case of the PTI, recycling of PM-associated immune components is controlled in large part by clathrin-mediated endocytosis (CME), a process that requires the function of the actin cytoskeleton (Nagawa et al., 2012). In well-studied in animal and yeast models, CME is initiated by loading the clathrin coat onto the PM components (e.g., PRRs), which induces concomitant physical changes in the PM endocytic membrane fraction. Once the clathrin coat is loaded onto the cargo, the newly formed compartment gradually bends towards the cytosol, ultimately resulting in a scission from the membrane. While the initial bending force that curves

the membrane is provided by the clathrin coated vesicles themselves, the growth and bending of the cargo-containing fraction is driven by actin polymerization. In short, this process is facilitated by the specific attachment of actin to the clathrin coat. Upon binding, the actin filaments extend by polymerizing and branching, a process mediated by the Arp2/3 complex and PM-associated myosin. This process is referred to as actin flow (Kaksonen and Roux, 2018). It is predicted that plants utilize functionally and mechanistically analogous processes to those in animal systems (Figure 1-5, (c)), yet in plants, the actin branching structure required for actin flow may not be mediated by the Arp2/3 complex (Fan et al., 2015). This hypothesis is supported by data showing that the Arabidopsis Arp2/3 mutant does not have a exhibit developmental lethality (Li et al., 2003), the expected phenotype if CME is fully inhibited.

In the case of plant immunity, multiple PRRs, as well as numerous additional PM-associated proteins, have been demonstrated to require CME for plant defense activation and signaling. For example, in the case of PTI, Mbengue *et al*. (Mbengue et al., 2016) demonstrated that FLS2, EFR (Ef-Tu receptor), and PERP1/2 (pep1 receptor) require clathrin, as well as the activity of BRI1-ASSOCIATED KINASE 1 (BAK1), for endocytosis, which are activated by corresponding PAMPs. A second study further indicates that CME is required not only for the endocytosis of PEPR1 itself, but also the activation of PEPR1-mediated defense responses (Ortiz-Morea et al., 2016). Interestingly, myosin inhibitor 2,3-butanedione monoxime (BDM) was found to inhibit FLS2 endocytosis, while the actin filament modifier latrunculin-B (LatB) was shown to have only a minor impact on FLS2 endocytosis (Beck et al., 2012). Taken together, these data support a role for actin cytoskeleton-mediated CME in the turnover and regulation of PM-associated immune receptors and their associated signaling processes. As one might expect, ETI-associated receptors also rely on CME for proper activity, as is the case for the tomato R-protein Cf-4, which functions in immunity against the pathogenic fungus *Cladosporium fulvum* (Postma et al., 2016).

The role of the cytoskeleton in intercellular trafficking of immune-associated processes

The plant immune response relies on specialized patterns of cellular trafficking to deploy the suite of proteins, organelles, and small molecules required for pathogen resistance signaling (Park et al., 2018). To facilitate the rapid re-localization of immune components to the site of infection, both MF and MT are required for the specific trafficking of immune cargo to the site of infection(Brandizzi and Wasteneys, 2013; Tominaga and Ito, 2015; Nebenführ and Dixit, 2018). As a broader function underpinning the regulation of this process, and moreover, the connectivity to PTI, numerous studies have demonstrated that the plant immune signal involves the positive feedback in the expression of PM-cell wall (CW) associated immune components (Figure 1-5, (d)), which include various signaling complexes, CW-associated polysaccharide synthases, and CW polysaccharide components synthesized in Golgi (Schneider et al., 2016; van de Meene et al., 2017; Bacete et al., 2018). For example, flg22 perception enhances the transcription of *FLS2*, *EFR*, *BAK1*, and *RBOHD* (Li et al., 2016), a process that is hypothesized to compensate for the turnover (i.e., endocytosis) of PM-associated immune components to sustain the immune (i.e., PTI) signaling capacity of the cell. The enhanced expression these PM-CW localized immune regulators requires a robust cytoskeleton system for their transportation and localization to the membrane. For instance, once pathogen signals (i.e., PAMPs) are perceived, callose- enriched papillae between the CW and PM will form to inhibit pathogen penetration, which is regulated by salicylic and jasmonic acid pathway (Luna et al., 2011; Yi et al., 2014). At a mechanistic level, callose deposition requires callose synthases (CalSs), enzymes that are sorted in Golgi and translocated to the cell wall. This process requires the activity of both MF and MT, and disruption of either cytoskeletal network leads to a dysfunction in CalS (Cai et al., 2011). Accordingly, in another study, it was demonstrated that an Arabidopsis class XI myosin mutant, with disrupted MF/MT trafficking, has dampened callose and lignin accumulation at the fungal infection site (Yang et al., 2014). Thus, from perception of PAMPs to the activation of PTI-associated defense

responses, the cytoskeletal network plays a key role in surveillance, activation, and the execution of immunity.

As noted above, the cytoskeleton is also required for the rapid re-localization of various host organelles and proteins to the site of pathogen penetration, a process that is hypothesized to enhance the immune response (Figure 1-5, (e-h)). In one of the best-characterized examples, Takemoto et al. (Takemoto et al., 2003) observed the accumulation of Arabidopsis ER and Golgi occur at the infection site of oomycete plant pathogen *Hyaloperonospora arabidopsidis*, simultaneously with rapid remodeling of actin filaments. Subsequent work further showed that these events paralleled the redistribution of the host nucleus, ER, Golgi, mitochondria, and peroxisome at sites adjacent to penetration events during powdery mildew infection (Takemoto et al., 2006; Yang et al., 2014). We posit that these processes function to accelerate defense-associated metabolism, yielding an increase in the rate of response during infection via cytoskeletal-mediated cellular trafficking.

The recent discovery of a role for chloroplast in plant immunity illustrates the complex relationship(s) between immune signaling and the cytoskeletal network. As a component of the plant defense system, the chloroplast plays a role in the activation of HR-PCD though its degradation, which functions as a source of ROS burst following ETI elicitation (Dong and Chen, 2013). Interestingly, disruption of the MT network has been shown to trigger chloroplast autophagy, yet this same disruption attenuates cellular autophagy (Wang et al., 2015). Based on this, it is difficult to discern a role for the concomitant regulation of chloroplast and cytoskeleton as a function of HR-PCD. However, the explanation may lie in recent data describing the function of stromule formation during the activation of plant defense. A recent study found that chloroplasts form a tube-like architecture, called stromules, which stretch towards chloroplasts as well as other plastids and even the nucleus, to mediate immune signaling (Hanson and Hines, 2018 ; Figure 1-

5, (i)). As an ETI-associated process, stromules were demonstrated to function in the transport of the N-Receptor Interacting Protein 1 (NRIP1; Caplan et al., 2008) and potentially other pro-immunity molecules into the nucleus to trigger the ETI against tobacco mosaic virus (TMV) effector p50 (Caplan et al., 2015). As a link to the engagement of the cytoskeleton, two recent study confirmed that the extension of stromules from the chloroplast is mediated by the cytoskeleton (Erickson et al., 2018; Kumar et al., 2018). In brief, these studies demonstrate that MT guides the stromules for extension, and application of the MT-disrupting agents amiprophos-methyl or oryzalin inhibited the growth of stromules. In parallel, MF serves as the anchor point rather than the extension track (Kumar et al., 2018), potentially through binding of the stromule via class XI myosin (Natesan et al., 2009). Taken together, these studies provide compelling evidence indicating the deployment of organelles and the transportation of their products is crucial for immune regulation, which relies on the activity of the cytoskeleton.

Battlefield cytoskeleton: the frontline of plant-pathogen interaction

Recent data from a suite of studies demonstrate numerous important roles for the plant cytoskeleton in the activation and signaling of plant immunity. However, the question remains: *Is the reorganization of the cytoskeleton a response, or a consequence? Is it associated with the activation of immunity, or a process manipulated by pathogens to induce susceptibility?* The short answer is both. A leading hypothesis in the field of cell biology and immunity is that the rapid and seemingly random reorganization of the cytoskeletal network is a plant-regulated cellular response to support immune signaling and downstream signaling of defense (Day et al., 2011). In this case, recent data demonstrates that pathogens alter both types of cytoskeletal structures during infection to evade immunity and promote infection. It is very common that rapid changes in cytoskeletal organization occur during immune activation. For example, perception of the PAMPs flg22, elf26, and chitin have all been shown to trigger the reorganization of actin in

Arabidopsis epidermal cells (Henty-Ridilla et al., 2013, 2014) and in stomatal guard cells (Shimono et al., 2016a). As predicted, these PAMP-stimulated events require the PRRs FLS2, Ef-Tu, and CERK1, reinforcing the requirement of the actin cytoskeleton for PRR-PAMP function. Upon infection of tobacco BY-2 cells, the *Pseudomonas syringae* DC3000 (*Pst* DC3000) type III secretion system (T3SS) helper protein, HrpZ, has been demonstrated to function as a PAMP, the perception of which induces bundling of F-actin and a concomitant decrease in MT density (Guan et al., 2013).

Alternatively, it is also demonstrated that pathogens can alter actin cytoskeletal structures during infection to evade immunity and promote infection. In a follow-up infection assay using *Pst* DC3000, it was observed that while the MT architecture did not change within 16 hpi (Lee et al., 2012); treatment for longer periods (i.e., >20 h) tended to induce long-term and multiple-phase influences on host actin. These changes included an initial increase in MF density, followed by a decrease in MF density with a concomitant increase in MF bundling at later stages of infection (Henty-Ridilla et al., 2013). Importantly, a type-III secretion system (T3SS)-deficient, avirulent, strain *Pst* DC3000 *ΔhrpH* was unable to trigger the second phase of remodeling, suggesting a role of pathogen virulence by the T3SS as well as T3Es themselves (Shimono et al., 2016b).

In the case of fungal pathogens, similar to bacteria, avirulent and virulent strains confer differences in the pattern of cytoskeleton re-organization, illustrating a role for the cytoskeleton as a common immune component in response to multiple types of pathogens. In the well-defined barley-powdery mildew interaction system, avirulent strains will trigger the rapid reorganization of host MF and MT during the invasion process(Kobayashi et al., 1992; Opalski et al., 2005; Miklis et al., 2007); this response is indicated by actin bundling at the interface of the mature appressorium, with the formation of a dense network of MF surrounding the papillae. Such phenomena are referred to as actin focusing, with F-actin linking the host nucleus and the host-

appressorium interface. For virulent strains, however, this pattern of filament organization is not observed, with only a slight aggregation of filament bundles without actin focusing. Interestingly, MT remodeling patterns show a similar trend, with the induction of thick radial arrays of MT bundles at the site of appressorium formation in the presence of avirulent isolates and no aggregation in the presence of virulent strains (Kobayashi et al., 1992). Similar to powdery mildew, studies in the cowpea-rust fungi interaction system also demonstrated that avirulent strains trigger MF and MT reorganization, leading to a reduction in filament density, while no significant reorganization is observed in cells infected by virulent strains (Skalamera and Heath, 1998).

In the case of bacterial pathogen infection, this phenomenon can be phenocopied by the application of cytoskeletal agents that interfere with MF and MT dynamics, manifesting in differing immune phenotypes between bacterial and fungal pathogens. For example, in the case of bacterial phytopathogens, disrupted MF increases resistance, including both PTI and ETI branches (Tian et al., 2009; Henty-Ridilla et al., 2013; Kang et al., 2014a; Krutinová et al., 2018), while disrupted MT increase susceptibility to infection (Lee et al., 2012). However, host resistance to fungal pathogens is usually dampened by both MF and MT dynamics inhibitor (Schmidt and Panstruga, 2007). These data indicate that cytoskeletal architecture has a significant influence on plant immunity, potentially controlled by both host and pathogen to alter the balance of resistance versus susceptibility.

While the broader function and mechanism(s) associated with MF/MT (re)organization in response to pathogen infection remain largely undefined, insight into the role of the cytoskeleton in plant immunity is becoming clearer through the analysis of individual MF- and MT-associated proteins. Among the first regulators of actin cytoskeletal organization revealed to play an important role in immunity are the actin depolymerizing factor (ADF)/cofilin (hereafter referred to as AC) family of proteins – a conserved class of small proteins that regulate actin cytoskeletal

organization via filament severing and depolymerization (Kanellos and Frame, 2016). As a family, ACs are widely conserved across all eukaryotes, yet their abundance varies: In human, 3 ACs have been identified (i.e., ADF, CFL1, and CFL2) and in most plants, dozens of ADF-encoding genes are present (11 in Arabidopsis, up to 27 in banana) (Kanellos and Frame, 2016; Nan et al., 2017). Similar to their mammalian counterparts, plant ADFs function as key regulators of cytoskeletal organization, controlling the overall balance of cellular G- and F-actin ratios.

In recent studies, ADFs have also been shown to be associated with the function and activity of the plant immune system. For example, as a regulator of PTI, it was demonstrated that Arabidopsis ADF4 plays a key role in PAMP-triggered actin remodeling, demonstrating that ADF4 – and actin depolymerization – are necessary components of actin remodeling and callose deposition upon elf26 perception by the EFR (Henty-Ridilla et al., 2014). In the case of fungal pathogen perception and immunity, the *adf4* mutant was found to possess enhanced resistance, with subclass I ADFs imparting an additive effect on pathogen susceptibility (Inada et al., 2016). Furthermore, these immune functions are controlled by the phosphor-regulation of CPK3, a critical mechanism to transduce immune signaling to the actin cytoskeleton dynamics (Lu et al., 2020). These data suggest that resistance signaling associated with ADF function may in fact be mediated in a homologue/class-specific manner, and moreover, that expansion of the ADF gene family in plants, as compared to mammals, may impart roles for specific and individual ADFs. Indeed, additional data support this hypothesis: Arabidopsis ADF6 was shown to negatively regulate the localization of RPW8.2 to extrahaustorial membranes to promote immune signaling (Wang et al., 2009); ADF3 is a positive regulator of resistance against aphids(Mondal et al., 2018); and in wheat, *TaADF4* and *TaADF7* significantly contribute to resistance against the stripe rust pathogen *Puccinia striiformis* (Fu et al., 2014; Zhang et al., 2017), while *TaADF3* is an negative regulator of this interaction (Tang et al., 2016). However, the detailed mechanism of these pro-immune function is unknown.

In addition to ADFs, the roles of other MF/MT associated proteins in plant immunity are beginning to emerge. For instance, capping protein (CP), which biochemically functions as an (+) end actin polymerization inhibitor, is required for MF re-organization during immune signaling (Li et al., 2015, 2017a). Further, a recent study has shown that Arabidopsis Profilin3 (PFN3) negatively regulates PTI by inhibiting formin-mediated actin polymerization (Sun et al., 2018). This discovery is interesting, because profilins are usually regarded as co-factors for formin-mediated actin polymerization. Thus, the biochemical function of AtPFN3 represents another strategy of cytoskeletal architecture regulation during immune activation – competitive inhibition of active cytoskeleton regulators. Converse to MF function during plant immunity, the molecular mechanism(s) of MT regulation during immune signaling events is relatively unclear. Thus, we posit that future work in the area of immune-MT interactions will lead to exciting new discoveries for the broader role of the cytoskeleton during plant defense and pathogen virulence.

Pathogen targeting of cytoskeletal organization: immune subversion and pathogenicity

Given the incredible connectivity of the cytoskeletal platform to nearly all cellular networks (Figure 1-5), it is not surprising that pathogens and pests have evolved mechanisms to block immunity – either directly or indirectly – through manipulation of cytoskeletal function. In this respect, by targeting a few key steps in cytoskeletal assembly, for example, pathogens can gain access to a range of host mechanisms. To usurp, evade, or destroy? These are the evolved “choices” that pathogens have made to overtake the function and activity of the immune system at the cytoskeletal interface. In the case of plant viruses, whose amplification and intercellular movement require manipulation of the host cell machinery, including cytoskeleton (Hong and Ju, 2017), the “choice” is to usurp. As a general strategy for viral manipulation of the cytoskeleton, the viral replication complex (VRC) can load itself onto the cytoskeleton using scaffold proteins (e.g., movement protein, linking protein) or myosins, which enable the virus to track along the

cytoskeletal network, including through plasmodesmata (Pitzalis and Heinlein, 2018, 2017; Figure 1-5, (j)). As a result, the infecting virus is able to move from cell to cell, overwhelming immunity, and ultimately taking control of the host.

As noted above, pathogen effector molecules function to subvert immune signaling, and in recent years, much effort has been spent on the discovery of the constellation of host processes targeted by these secreted factors. Thus, it was only a matter of time before pathogen effectors were identified which can directly and/or indirectly influence cytoskeletal function. In the case of indirect modulation of cytoskeletal function, work from Lee and colleagues (Lee et al., 2012) observed that the *Pst* DC3000 T3E HopE1 can bind to calmodulin, a process that leads to disassociation of the microtubule-associated protein 65-1 (MAP65-1) from the MT network, resulting in an increase in susceptibility to *Pst* DC3000. In a similar mechanism, the *Xanthomonas euvesicatoria* T3E AvrBsT, and acetyltransferase, was shown to acetylate ACETYLATED INTERACTING PROTEIN1 (ACIP1), causing it to dissociate from MT, leading to a dampening of plant immunity (Cheong et al., 2014). Interestingly, it has also been demonstrated that pathogenic effectors can also influence the regulation of cytoskeletal function within and between organelles. As demonstrated by Erickson *et al*., the *Xanthomonas campestris* T3E XopL, an E3 ligase, suppresses plastid stromule formation induced by Agrobacterium; it is hypothesized that XopL targets unknown MT-associated proteins, a conclusion based on the observation that a non-active mutant of XopL loses such function but binds to MT (Erickson et al., 2018).

Lastly, and in work supported by independent studies that converged on similar pathogen virulence mechanisms, is the case of the *P. syringae* T3E HopG1. Previous work showed that HopG1 is a mitochondria-targeted effector that suppresses plant immunity (Block et al., 2010). In

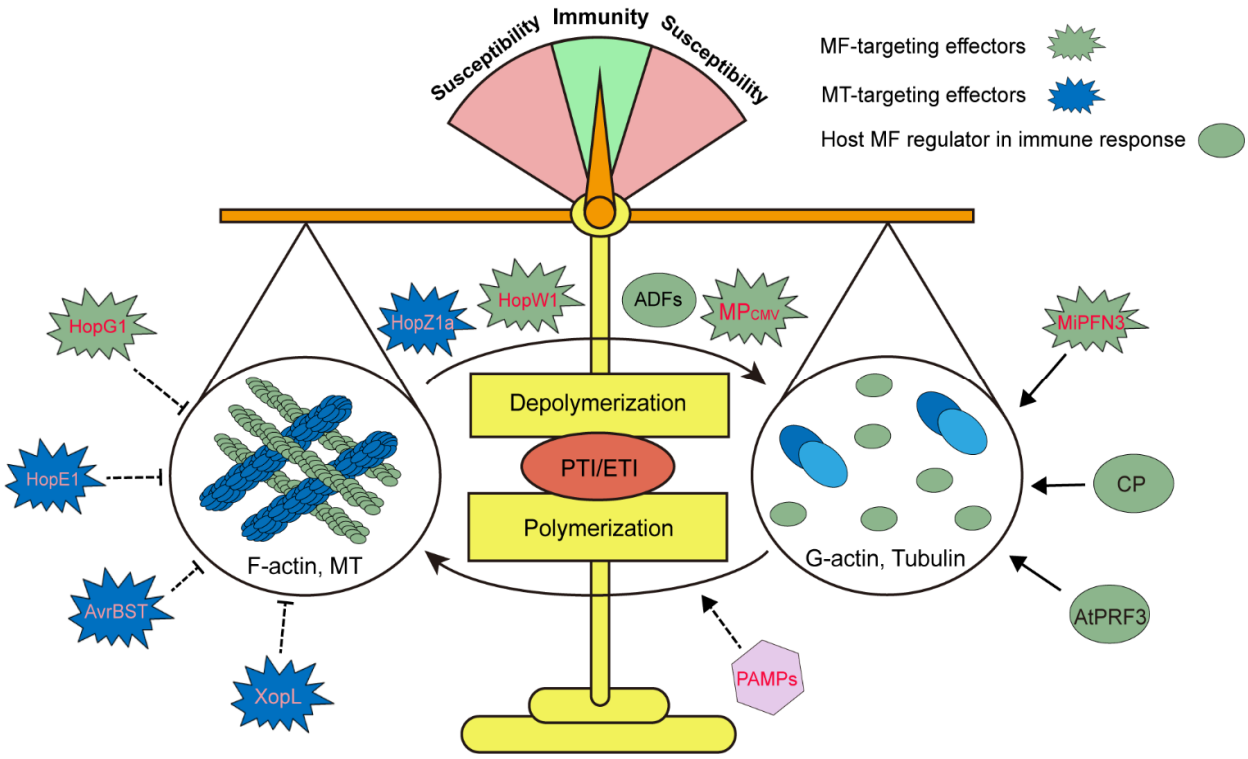

Figure 1-6: The cytoskeleton is central to the balance between immunity and susceptibility, and the host-dominated balance and alterability between G-actin, F-actin, and tubulin control the plant response to pests and pathogens. The cytoskeleton is tightly regulated by the temporal and spatial control of filament architecture, and these points of control are influenced by the perception of pathogens and pathogen elicitors (i.e., PAMPs, effectors). For host, identified actin regulator in immune response includes ADFs (depolymerizing and severing actin), CP (stabilizing short F-actin oligo and G-actin), and AtPFR3 (stabilizing G-actin). Pathogen and pests, on the other hand, can use effectors to interfere the host regulation of cytoskeleton. For instance, HopW1 and the CMV movement protein (MP) can directly sever F-actin, thus increasing the cellular concentration of G-actin. Similarly, HopZ1a can disrupt MT filaments by acetylating tubulins, a process that results in disruption of the MT network and associated process. In the case of MF function, MiPFN3 can stabilize G-actin and directly inhibit actin assembly. HopG1, HopE1, AvrBsT, and XopL can indirectly interfere host cytoskeletal function.

a bid to define virulence factors that target host cytoskeletal immune signaling, Shimono et al. (Shimono et al., 2016b) demonstrated that HopG1 interacts with Arabidopsis kinesin 7.4 (i.e., Kin7.4), a mitochondria-localized motor protein whose function is required for actin filament organization. During *Pst* DC3000 infection of Arabidopsis, HopG1 is delivered into the host cell, and subsequently associates with Kin7.4, resulting in actin bundling and enhanced disease symptom development. This is exciting from the standpoint of pathogen targeting of the

cytoskeleton and in the broader context of a role for actin in immunity. For example, if HopG1 and kinesin associate on the mitochondrial outer membrane, this might suggest a mechanism to inhibit the motor activity of kinesin, leading to an impediment in mitochondrial motion through the concerted action of both (i.e., MF and MT) cytoskeletal networks. This would then lead to a reduction in the energy needed to support cytoskeletal function and dynamism (Bartolák-Suki et al., 2017). However, if HopG1 and kinesin localize within the mitochondria itself, it would indicate a role for HopG1 in the disruption of kinesin function and a broader role of mitochondria as a signaling hub for immunity and cell death through actin filament remodeling. We tend to favor the latter, as evidence for such a role is supported by numerous studies demonstrating a function for the actin-mitochondrial network as a hub for the activation of apoptosis, a process associated with pathogen-induced senescence (Shimono et al., 2016b).

Converse to the examples highlighted above – whereby pathogens finesse cytoskeletal function to promote infection and disease – pathogens have also evolved virulence strategies to disrupt actin cytoskeletal dynamics in a more abrupt manner. In short, pathogens can paralyze host immunity by directly dissembling the cytoskeletal machinery. In one of the first examples of directed targeting of the plant cytoskeleton by a phytopathogen, work by Lee et al. (Lee et al., 2012) uncovered a mechanism whereby the *P. syringae* T3E HopZ1a, an acetyltransferase, can modify and disrupt the MT network to interfere with MT-supported processes, such as trafficking. More recently, work by Kang et al. (Kang et al., 2014) showed that the *P. syringae* T3E HopW1 disrupts F-actin integrity by directly depolymerizing actin filaments during infection, a process resulting in blocks to protein cargo trafficking and endocytosis. Such strategies are also employed by viral pathogens, such as the case of the cucumber mosaic virus (CMV) movement protein (MP), which can sever F-actin to increase the size exclusion limit of plasmodesmata, potentially accelerating the viral spread to adjacent cells (Su et al., 2010). Additionally, a newest study demonstrates that root-knot nematodes secrets an effector, *Meloidogyne incognita* Profilin3

(MiPFN3) into host “giant cell”, the feeding structure, to inhibit host actin polymerization and cause higher susceptibility (Leelarasamee et al., 2018).

While each of these examples clearly demonstrates that direct disruption of the MT or MF networks are strategies to impede plant immunity, the question remains as to how the activities of these effectors are coordinately regulated, since absolute disruption of plant MF/MT does not always lead to attenuated immune response, as mentioned above. One hypothesis is that additional signals are generated during infection that leads to proper regulation of effector-mediated cytoskeleton dissemble. This would, hypothetically, result in the specific modulation of effectors’ activities at different key stages of the infection process, which leads to disruption of immune signaling. Such strategies have been characterized in the case of *Salmonella* infection of human cells, in which the co-regulation of the type-III effectors SipA and SipC, with opposing yet cooperative, actin polymerizing and depolymerizing activites renders the immune escape (McGhie et al., 2009).

Emerging themes on the immune functions of the nuclear actin cytoskeleton

The past two decades have witnessed the discovery of numerous mechanisms underpinning the linkages between the cytoskeleton and plant immune system (Figure 1-6). However, like many pieces of research on other fields of the cytoskeleton, these studies mainly focused on the cytoskeleton – including its associated proteins – in the cytoplasm, leaving the nuclear cytoskeleton not well explored. In fact, according to the studies using animal systems, the molecular functions of proteins associated with the nuclear cytoskeleton are sometimes different from those from the cytoplasm. For example, the nuclear actin also forms the filament configuration, but this short nod-like F-actin can interact with RNA polymerase to form a transcriptional regulatory complex (Kelpsch and Tootle, 2018), a novel activity compared to the

similar cytoplasmic architecture. Besides, other nuclear-exclusive functions of actin include but are not limited to facilitating chromatin remodeling, chromatin movement, histone deacetylation, DNA damage repair, and maintenance of the nuclear mechanical structure (Kelpsch and Tootle, 2018). As both actin and most of the actin-associated proteins exist in the nucleus, it is hypothesized that the actin dynamics is empowered by a different set of biological significance in the nucleus.

While there is currently no study supporting a particular immune function of the nuclear cytoskeleton at the mechanism level, there is indeed genetic evidence suggesting that ADFs, as a family of actin-binding protein introduced above, contribute to functions that support pathogen resistance in the nucleus. First, Arabidopsis ADF4 contributes to the robust transcription of the NB-LRR protein RPS5, which can be further regulated by ADF4 phosphorylation (Tian et al., 2009; Porter et al., 2012); however, its cytoplastic function as a mediator of actin severing/depolymerization cannot explain such activity. Second, in another study, it was reported that ADF4 genetically contributes the resistance against powdery mildew exclusively when it is imported into the nucleus (Inada et al., 2016). While the evidence is relatively indirect, the framework exists to further define and conceptually link the role of the cytoskeleton in almost every step of plant immune response, from pathogen perception to the regulation of the immune transcriptome. This work is particularly described in *Chapter 3* of this dissertation, where my study revealed that ADFs control pro-immune transcription by directly interacting with WRKY transcription factors.

Chapter 2: Implicit Laplacian of Enhanced Edge (ILEE): An unguided algorithm for accurate and automated quantitative analysis of cytoskeletal images

(The chapter is revised from Li et al., 2021, a preprint release under submission process.)

Chapter abstract

The eukaryotic cytoskeleton plays essential roles in cell signaling, trafficking, and motion. As recent work explored and discovered an emerging link between cytoskeleton dynamics and plant immunity, it becomes more important to utilize quantitative analysis of cytoskeletal fluorescence images as a standard approach to define cytoskeletal function and correlate with immune process. However, due to the uneven spatial distribution of the cytoskeleton, including varied filament shape and unstable binding efficiency to staining markers, these approaches may result in inaccurate cytoskeletal segmentation. Additionally, quantitative approaches currently suffer from human bias, as well as information loss caused by *z*-axis projection of raw images. To overcome these obstacles, I developed Implicit Laplacian of Enhanced Edge (ILEE), a cytoskeletal component segmentation algorithm, which uses as 2D/3D-compatible, unguided local thresholding approach, therefore providing less biased and more stable and accurate results. Empowered by ILEE, I constructed a Python library, namely ILEE_CSK, for automated quantitative analysis of cytoskeleton images, which computes cytoskeletal indices that cover density, bundling, severing, branching, and directionality. Compared to various classic approaches, the ILEE generates descriptive data with higher accuracy, stability, robustness, and efficiency, providing a superior platform for the evaluation of cytoskeletal organization and status. My study also revealed that the treatment of a virulent bacterial pathogen on Arabidopsis leaf causes a multi-aspect regulation of cytoskeleton dynamics, which provides a foundation to investigate and define the link between plant immunity and cytoskeleton. In addition to the

analysis described herein, I have released ILEE_CSK as an open-source library for the community, together with Google Colab pipelines, as a convenient and user-friendly access that requires no programming knowledge or specific computer requirements for usage.

Introduction and rationale

As discussed in Chapter 1, plants, as well as other higher eukaryotes, have evolved complex mechanisms to organize and co-regulate a multitude of cellular processes, including growth, development, movement, cell division, and response to environmental stimuli. For example, plants coordinate growth with resistance against abiotic and biotic stress by engaging numerous systemic signaling processes, among which the cytoskeleton plays an indispensable role (Lian et al., 2021). To facilitate these processes and ensure robust and highly specific responses to changes in cell status, plants utilize two types of cytoskeleton – microfilaments and microtubules – to connect intercellular signaling to extracellular environments. Structurally, both of them are chains dynamically assembled from monomeric subunits named global actin and tubulin, respectively, and are involved in ceaseless events of polymerization/depolymerization, bundling, severing, and branching (Blanchoin et al., 2014; Brouhard, 2018), which is commonly referred to as “cytoskeletal dynamics”. Therefore, the foundational step to explore the relationship between the plant immunity and the cytoskeleton is to define and observe the status of cytoskeleton dynamics – the behavior of cytoskeleton – during an immune event.

Over the past several decades, confocal microscopy-based methods using fluorescence markers have been developed to monitor changes in cytoskeletal organization (Melak et al., 2017). While showing advantages in real-time observation and intuitive visual presentation, these approaches possess critical limitations – namely, they are subject to interpretation from captured images, which potentially involves human bias. As a step to remedy this limitation, the emergence of

computational algorithm-based analyses offers a solution to describe the quantitative features of cytoskeletal architecture with reduced human bias. However, while early studies introduced the concept of using generalizable image processing pipelines (Lichtenstein et al., 2003; Shah et al., 2005) to transfer the task of evaluation away from the user and into a series of computer-based quantitative indices, several key bottlenecks emerged. First, most of the quantitative algorithms described to date are limited to 2D images. As a result, these approaches require the user to manually generate z-axis projections from raw data, resulting in an incredible amount of information loss, especially within the perpendicular portion of the cytoskeleton. Second, many approaches require users to manually set the threshold to segment cytoskeletal components from the images, resulting in sampling bias. Lastly, the accuracy and robustness of current algorithms greatly varies among different types of biological samples. This latter hurdle imposes a considerable disparity in the algorithm performance for plants (usually with curvy and spherical cytoskeleton) and animal (usually straight and complanate) samples, which compromises the performance of some advanced cytoskeleton analysis algorithms (Liu et al., 2020, 2018; Alioscha-Perez et al., 2016) when directly applied to plant cell images. In fact, while sample source greatly impacts our ability to evaluate the features of cytoskeletal function across all eukaryotes, the vast majority of current approaches are developed based on cytoskeletal images from animal cells, which indicates potential systemic bias when applied to other types of image samples, such as plant.

Previous work described the development of a global-thresholding-based pipeline to define and evaluate two key parameters of cytoskeleton filament organization in living plant cells: cytoskeletal density, defined by *occupancy*, and bundling, defined by statistical *skewness* of fluorescence(Higaki et al., 2010). Interestingly, while it utilizes manual global thresholding (MGT), which can potentially introduce a certain level of user-bias, it still outperforms many standardized adaptive/automatic global or local thresholding approaches such as Otsu (Otsu, 1979) or Niblack

(Niblack, 1985). As a further advance of this early work, Higaki and colleagues developed the use of coefficient of variation (*CV*) of fluorescence to quantify the level of filament bundling, which improved the robustness and utility of the algorithm(Higaki et al., 2020). However, not only does this pipeline consume a considerable amount of time and effort from users for massive sample processing, but it also leaves unaddressed two key issues of rigor in image processing and analysis: information loss and human bias.

In the current study, I led a team and developed implicit Laplacian of enhanced edge (ILEE), a 2D/3D compatible unguided local thresholding algorithm for cytoskeletal segmentation and analysis, which is based on the native value, first-order derivative (i.e., gradient), and second-order derivative (i.e., Laplacian) of the cytoskeleton image altogether (see Figure 2-1). The research described herein supports ILEE as a superior quantitative imaging platform, one that overcomes current limitations related to information loss through dimensional reduction, human bias, and inter-sample instability. As shown, ILEE can accurately process cytoskeleton samples with a high dynamic range of fluorescence brightness and thickness, such as live plant sample.

As a key advance in the development of ILEE, I further established an ILEE-based Python library for the fully-automated quantitative analysis of 12 cytoskeletal indices within 5 primary classes: density, bundling, connectivity, branching, and anisotropy. This platform not only enables the acquisition and evaluation of key actin filament parameters with high accuracy from both projected 2D and native 3D images, but also improves the accessibility to a broader range of biologically relevant states, including polymerization/depolymerization, bundling, severing, branching, and directional regulation. The library, ILEE_CSK, is publicly released at GitHub (https://phylars.github.io/ILEE_CSK/). In addition, I developed the ILEE Google Colab pipelines for the one-stop data processing, visualization, and statistical analysis, which is a convenient and user-friendly interface that requires no programing experience or computational device.

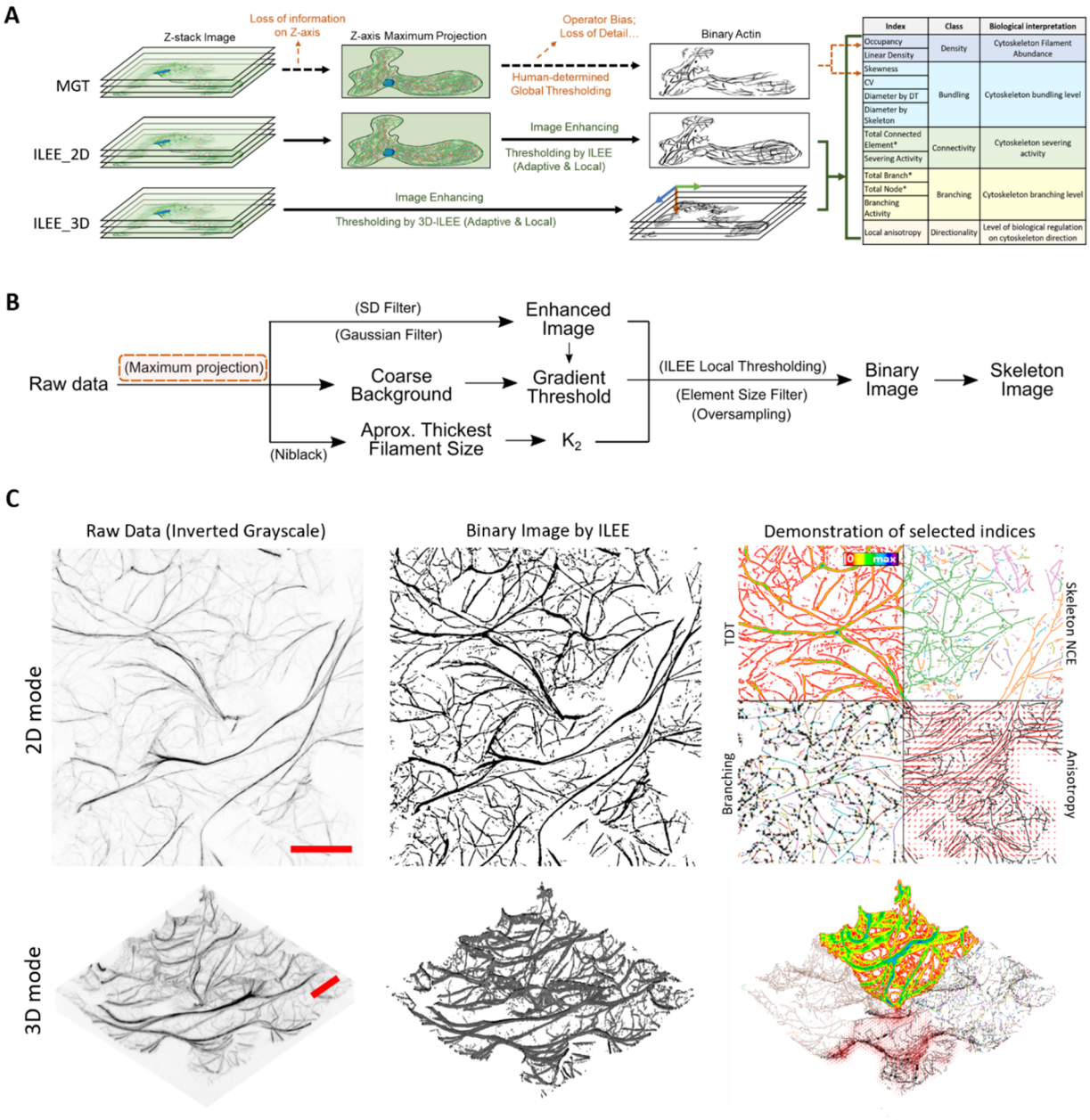

Figure 2-1: ILEE pipeline and the demonstration of cytoskeletal indices. A, ILEE is an adaptive local thresholding approach that applies to both 2D and 3D data structures, with an output of 13 cytoskeletal indices. **B**, Schematic diagram of the ILEE algorithm. ILEE requires a sample image with enhanced edge gradient, a computed gradient threshold, and an implicit Laplacian smoothing coefficient, K_2, to generate a binary image and skeletonized image for index computation. Z-axis maximum projection (red box) is only conducted in the 2D mode. **C**, Visualized demonstration of ILEE performance. Raw data, binary image generated by ILEE, and visualization of selected data, by both 2D and 3D data structure are shown. TDT, total distance transformation map, used to compute all diameter indices; skeleton NCE, non-connected elements of skeleton image with each element in different color, used to calculate severing activity; branching, skeleton image with each branch in different color and each node by black cross; anisotropy, local anisotropy level, shown as length of red lines, and direction of first eigen vector, shown as the direction of red lines. Scale bar = 20μm.

Results

The ILEE pipeline

Raw images generated by laser scanning confocal microscopy are typically obtained through detecting in-focus photons by a sensor from each resolution unit on a given focal plane. Since the cytoskeleton is a 3D structure which permeates throughout the cell, current approaches to capture filament organization and architectural parameters rely on pixel scanning of each plane along the z-axis, independently, at regular intervals within a given depth, and reconstruction into 3D images. However, due to limited computational biological resources, most studies have exclusively employed the z-axis projected 2D image, which results in substantial information loss, as well as systemic bias in downstream analyses.

In our newly developed algorithm, I integrated both 2D and 3D data structures into the same processing pipeline to ameliorate the aforementioned conflict (Figure 2-1A). In short, this pipeline enabled automatic processing and evaluation of both traditional 2D and native 3D z-stack image analysis. As shown in Figure 2-1B, cytoskeleton segmentation using ILEE requires 3 inputs: an edge-enhanced image, a global gradient threshold that recognizes the edges of potential cytoskeletal components, and the Laplacian smoothing coefficient *K* (described below). With these inputs, a local threshold image is generated via ILEE, and the pixels/voxels with values above the threshold image at the same coordinates are classified as cytoskeletal components. The output of this is the generation of the binary image (Figure 2-1C). Once acquired, the binary image is further skeletonized (Lee et al., 1994) to enable the downstream calculation of numerous cytoskeleton indices, the sum of which comprises the quantitative features of cytoskeletal dynamics (Figure 2-1C). Additionally, because the 2D and 3D modes share a common workflow, all of the calculated cytoskeleton indices also share the definition for both modes, regardless of the difference in dimensional spaces. This additional feature enables a horizontal comparison of

both modes by the user, which will significantly contribute to the community by providing massive image datasets for further examination, and comparison through the open-source library. In general, the ultimate goal of this approach, and resultant algorithm, is to construct a pipeline that enables the automated detection of the eukaryotic cytoskeleton from complex biological images in an accurate and unbiased manner.

Identification of coarse background

One of the central problems of automated cytoskeletal image processing is how to accurately recognize cytoskeletal components – a task that is extremely challenging because object pixels (i.e., cytoskeleton components) generally have a high dynamic range of signal intensity within and among individual samples, due to varied bundle thickness, the concentration of fluorescent dye, and its binding efficiency. As a framework to further understand this challenge, the value of a single pixel captured using confocal microscopy is conceptually comprised of three components: (1) the true fluorescence, that which is emitted by the dye molecules within the pixel, (2) the diffraction signal transmitted from neighboring space, and (3) the ground noise generated by the sensor of the imaging system (Figure 2-2A). During confocal imaging, the ground noise is a constant due to fixed setting of photon sensors, while the diffraction signal is positively correlated with the local fluorescence. Therefore, an ideal actin segregation algorithm will be a local thresholding approach that refers to both ground noise and local signal intensity.

In order to identify ground noise and locate the background for downstream analyses (e.g., fine thresholding), I designed an algorithm that calculates a global threshold using the morphological features of the ground noise; namely, non-connected negative element scanning (NNES; Figure 2-2B). In brief, NNES calculates the total number of non-connected negative elements at different

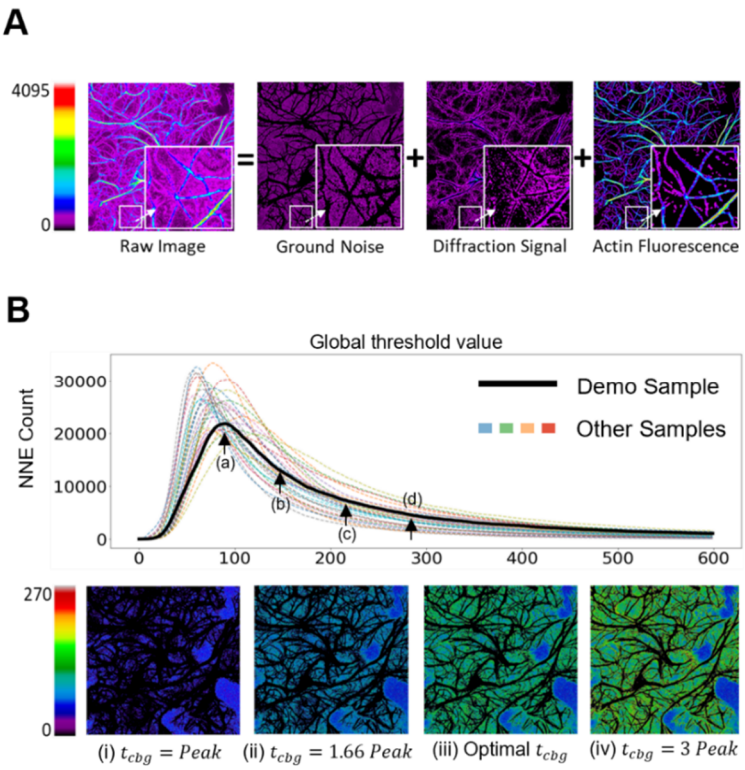

Figure 2-2: NNES global thresholding. A, the conceptual decomposition of confocal fluorescence image of cytoskeleton. An Arabidopsis leaf confocal microscopic image of actin, as an example of the eukaryotic cytoskeleton, can be decomposed into 3 components: ground noise, the mechanical noise of the sensor regardless of true fluorescence signal, diffraction light, the unavoidable diffraction signal of fluorescence component around, and true actin signal. They correspond to noise filtered by coarse background, noise additionally filtered by ILEE, and segmented actin components in the algorithm. **B**, The performance of NNES. The curve reflecting the NNE (negative non-connected component) count when certain global thresholding is applied to the raw images of 30 randomly selected sample in the database of my Lab. They have a very smooth shape, which is easy to detect the peak as a feature value. The demonstration of filtered background of position (i), (ii), (iii), and (iv) are shown above, where (iii) is adopted. The black area surrounded by colored area is the foreground information to be further processed.

global thresholds, resulting in the identification of a representative value with a maximum non-connected negative element count (Figure 2-2B, (i)). The global threshold for the coarse background (Figure 2-2B, (iii)) will be determined using a linear model trained by the representative value rendered by NNES and manual global thresholding (MGT), a global threshold determined by operators experienced in cytoskeleton image analysis (Figure AA-1 and AA-2). NNES can maintain stability and accuracy over different samples that vary in the distribution of native pixel value, because ground noise is the image component with the lowest

value that is subject to a normal distribution and generally does not interfere with the actual fluorescence signal. Another accessible method is to directly use the peak-of-frequency brightness of the image as a representative value to train a model. However, this approach is less accurate because the interval near the theoretical peak is always turbulent and non-monotone, a limitation potentially due to the pollution of diffracted light (Figure AA-1).

Cytoskeleton segmentation by ILEE

The core strategy of ILEE is to accurately identify the edge of all cytoskeletal filament components and apply an implicit Laplacian smoothing (Desbrun et al., 1999) on the selected edge, which generates a threshold image that refers to high gradient areas and smoothly connects the selected edge of potential cytoskeleton fractions (Figure 2-3A). As illustrated in Figure AA-3A, the general local threshold trend changes as a function of the baseline values of the cytoskeleton edges. This is because ILEE selectively filters out high-frequency noise while preserving salient geometric features of individual actin filaments, in leveraging the spectral characteristics of Laplacian operators (Figure AA-3B). Thus, ILEE can filter the background and noise regardless of the general local brightness level, and it therefore does not require an operating kernel that may restrict the performance at varying filament thickness. Additionally, the edge of the cytoskeletal component is smoothed and elongated using a significant difference filter (SDF; Figure AA-4) and a Gaussian filter, the sum of which serves to enhance the continuity of the edge and contributes to the accuracy of edge detection (Figure 2-1B and 3A). Based on this process of the computational pipeline, I named this algorithm Implicit Laplacian of Enhanced Edge (ILEE).

The core concept of ILEE was proposed by Dr. Yiying Tong and Ze Zhang, the collaborators in my team. The algorithm builds a linear system based on Laplacian operators to achieve local

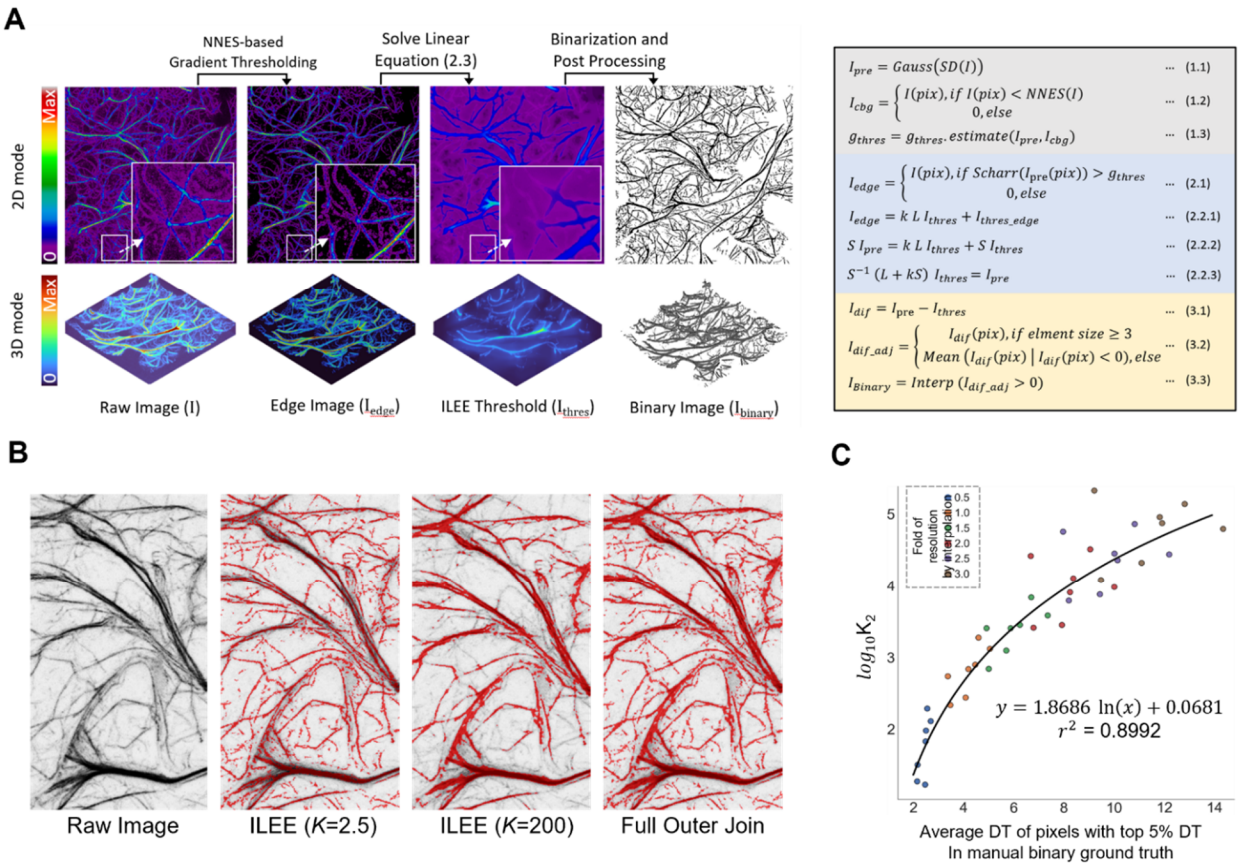

Figure 2-3: Cytoskeletal identification by ILEE. A, Visual demonstration and summarized mathematical process of ILEE. On the left, the visualized intermediate images of ILEE process are presented; on the right, an abbreviated mathematical process of ILEE is shown (see Method for detailed computational process). Grey, image pre-processing; blue, ILEE in a narrow sense; yellow, post processing. **B**, The value of implicit Laplacian smoothing coefficient *K* influences ILEE performance. When *K* is small (e.g., 2.5), the rendering of faint and thin filaments is accurate, but the edge of thick filaments tends to be omitted. Conversely, when *K* is large (e.g., 200), rendering of thick filaments is accurate but thin and faint filaments are omitted. I adopt a solution to use a full outer join image of a fixed K_1 = 2.5, and an estimated universal K_2 for an entire biological batch of samples. **C**, Optimal K_2 estimation model. I established a regression model to compute any universal K_2 for a given sample batch (see Figure AA-8 for detail). To maximize the training sample pool, 7 images with manually portrayed ground truth binary image (shown as single dots) are interpolated by a new resolution of different folds to the original (shown as different color) into 42 samples that cover the general range of actin thickness by pixel. The adopted K_2 are computed as one that render an average deviation rate of distance transformation (DT) compared to the ground truth, and a non-linear regression estimation model is trained using the mean of top 5% DT values and these K_2. For input sample pool for ILEE, the mean of top 5% DT will be calculated by Niblack thresholding.

adaptive thresholding for edges of cytoskeletal components (see *Methods* for detail). To do this, we first calculated the gradient of the whole image. Then, based on an estimated global threshold

of the gradient magnitude (g_{thres}) over the image, we identified pixels above g_{thres} as boundary elements (I_{edge}) with high gradient magnitude to preserve during implicit Laplacian smoothing (Figure 2-3A, 2.1). Accordingly, we constructed a selection matrix *S*, a diagonal matrix with *i*-th diagonal entry being 1 if the *i*-th pixel has a norm of the gradient above g_{thres}. The output of this approach is marking all of the elements to be kept as the boundary of the cytoskeleton filament, which serves as a guidance for local thresholding. Using this approach, I_{edge} can be mathematically redefined as shown in Figure 2-3A, equations 2.2.1 and further 2.2.2, where *L* is the Laplacian matrix and *K*, or implicit Laplacian smoothing coefficient, is a weight that adjusts the influence of the Laplacian operator. The local threshold image can therefore be rendered by solving the linear equation shown in Figure 2-3B, 2.2.3. A detailed mathematical algorithm is introduced in *Methods*.

For a given image input, the performance of ILEE depends on two parameters: g_{thres}, which defines the edge, and *K*, which determines the weight of detail (i.e., high-frequency components) to be filtered. To calculate the optimal g_{thres} for an input image, the pixel brightness values of the area identified as coarse background by NNES are used. Since the ground noise is subjected to a normal distribution, I hypothesized that there is a certain deducible statistical relationship between the image gradient, defined by Scharr operator (Scharr, 2000), and the native brightness of pixels within the coarse background. Using a normal random array that simulates the noise with a 2D or 3D data structure, I demonstrated that the distribution of the background gradient magnitude is also normal-like, and both mean (μ_G) and standard deviation (σ_G) of the gradients are directly proportional to the standard deviation of their native pixel values (σ_{cbg}), and I calculated the proportionality coefficient (see Figure AA-5). For 3D mode, since the pixel size on the x- and y-axis is different from that of the z-axis, the proportionality coefficient of μ_G and σ_G over σ_{cbg} will vary for different ratios of the x-y unit : z unit (see Figure AA-6). To solve this problem,

I simulated artificial 3D noise images and trained a multi-interval regression model that accurately (R^2 > 0.999) calculates the proportionality coefficient of μ_G and σ_G over σ_{cbg} for different x-y : z ratios of the voxel. Finally, using this approach and randomly selected actin image samples, a prediction model is established as $g_{thres} = \mu_G + k(\sigma_{cbg}) * \sigma_G$, to determine the g_{thres} as ILEE input (Figure AA-7).

To determine the appropriate setting of *K*, I first tested how different *K* values influence the result of the local threshold image (I_{thres} of Figure 2-3A). As shown in Figure AA-8A, at the optimal g_{thres}, a low value of *K* generated an I_{thres} that is highly consistent with the selected edge. When *K* increases, the total threshold image shifted towards the average value of the selected edges with increasing loss of detail. As for the resultant binary image, a relatively lower *K* enables the accurate recognition of thin and faint actin filament components, yet is unable to cover the full width of thick filaments. Conversely, a high *K* value covers thick actin filaments with improved accuracy, resulting in a binary image that is less noisy; however, thin and/or faint filaments tend to be omitted as pseudo-negative pixels (Figure 2-3B, Figure AA-8A). To overcome this dilemma, I applied a strategy using a lower K_1 and a higher K_2 to compute two different threshold images, as well as binary images, that focuses on thin/faint components and thick components, respectively. Then, I generated a full outer-join image that contains all cytoskeleton components in these two binary images. This approach led to improved recognition of actin with varying morphologies (see Figure 2-3B).

As described above, K_1 controls the performance of thin and faint filaments. Since the theoretical minimum thickness of distinguishable cytoskeletal components is approximately equal to one pixel unit, K_1 can be fixed to a constant to recognize the finest of cytoskeletal components from a complex and heterogeneous set of input samples. Using this combined approach, I identified an

empirical optimal K_1 of 2.5. However, since different image samples have different distributions of cytoskeleton thickness, K_2, which controls the performance over thick filaments, must be guided according to the maximum thickness among all samples. To ensure that the algorithm described herein is fully unguided, my strategy was to estimate an appropriate K_2 from an estimated maximum thickness using all samples from a single batch of experiments, including multiple biological replicates (if applicable). To do this, I used Niblack thresholding to first generate a coarse binary image (which is sufficiently accurate for the thickest portion of the filament) and from this, I calculated the mean of the top 5% of the Euclidian distance transformation (DT) values of all positive pixels (see *Methods* for additional information). Next, the top 5% means of all single images were averaged, which is used to estimate K_2 via a trained model using diverse samples with manual binary ground truth (Figure 2-3C and Figure AA-8B, C, D). All individual image samples of all groups in the same batch of experiment were processed through ILEE by this K_2, and hence the bias of human input was avoided. When processing native 3D images, additionally, an alternative approach that uses a single *K* that balances the accuracy over thin/faint and thick filaments is provided, because the 3D ILEE can be time-consuming if MATLAB-based GPU acceleration (already employed by the library) is not applicable for individual users.

Computational analysis of cytoskeleton indices

For image library assembly, cytoskeletal indices are automatically calculated from the binary image generated by ILEE. As a substantial expansion from the previously defined cytoskeletal indices (e.g., *occupancy*, *skewness*, and *CV*)(Higaki et al., 2010, 2020), this study proposed 12 indices (including 8 core indices; see Figure 2-4 for a visualized demonstration) within 5 classes. In short, these classifications describe and function as quantifiable features of cytoskeletal morphology and dynamics, and importantly, each of these are critical considerations within the context of complex biological samples (Figure 2-1A; see also *Methods* for detailed mathematical

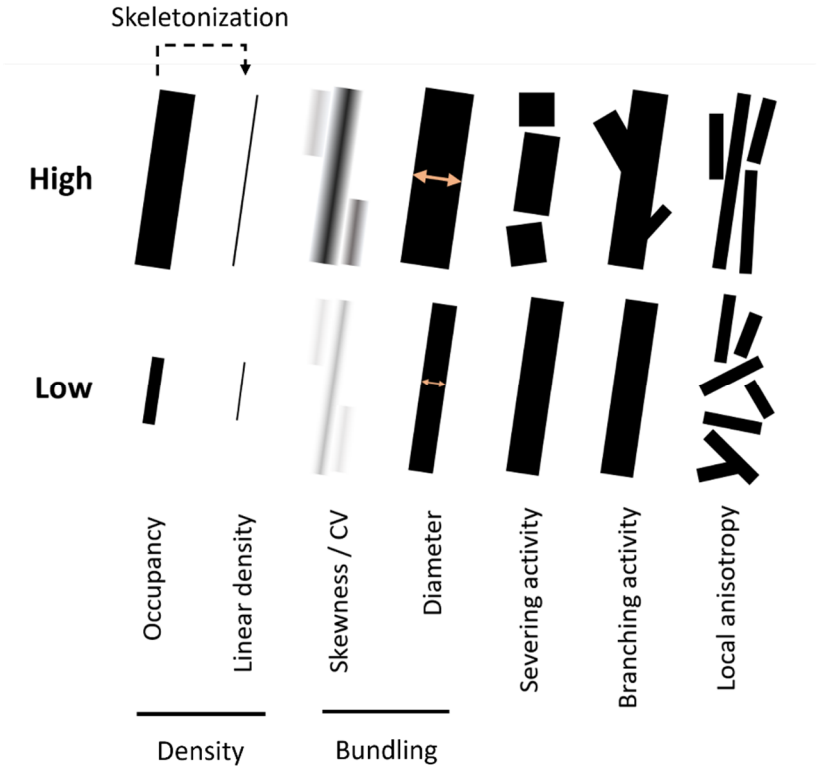

Figure 2-4: Visualized demonstration of concepts of cytoskeleton indices. Major cytoskeleton indices involved in this research are explained by showing schematic cytoskeleton pieces representing high vs low value of the indices. Skewness/CV, as well as Diameter (TDT/SDT) have similar concept and reflect similar features of cytoskeleton image, with minor difference in their mathematical definition (see *Methods* in this Chapter); therefore, their demonstrations are merged.

definitions). It is worth noting that all of these indices require a certain level of image post-processing (e.g., oversampling) to further enhance the accuracy, which is described in *Methods*.

For the index class “density”, I developed a novel set of metrics to evaluate *linear density*, a feature that measures filament length per unit of 2D/3D space. For “bundling”, I developed two new, highly robust, indices referred to as *diameter by total DT* (*diameter_TDT*) and *diameter by skeleton DT* (*diameter_SDT*), both of which measure the physical thickness of filament bundles, in addition to the indirect indices *skewness* and *CV*, which estimate the relative bundling level

based on statistical distribution of fluorescence intensity. For the class “connectivity”, I introduced two indices, *total connected element* and its derived index – *severing activity*, which estimates the severing events within per length unit of the cytoskeleton. This additional metric assumes that severing generates two visible cytoskeletal filaments, which is distinguishable from filament depolymerization. This is an important consideration in terms of the biological activity of the cytoskeleton, as it enables the decoupling of the impact of filament depolymerization and filament severing, key activities of the eukaryotic actin depolymerizing factor (ADF) and cofilin family of proteins(Tanaka et al., 2018). For the class “branching”, my algorithm is based on Skan, a recently developed Python library for graph-theoretical analysis of the cytoskeleton (Nunez-Iglesias et al., 2018). To further explore the relationship between filament morphology and the biological activity of branching, I specifically designed an additional index, referred to as “branching activity”, which I define as the total number of additional branches emerging from any non-end-point node per unit length of filament. In total, this index measures the abundancy/frequency of cytoskeletal branching. Finally, the library is capable of estimating the level of directional cytoskeletal growth by indexing *local anisotropy*, which measures how local filaments tend to be directional or chaotic. This approach is adapted from an ImageJ plug-in FibrilTool (Boudaoud et al., 2014), but we expanded this algorithm to 3D with both numerical and visual output (Figure 2-1C), contributed by my collaborator Ze Zhang.

ILEE displays high accuracy and stability over actin image samples

To evaluate the performance of ILEE in terms of its accuracy and compatibility over diverse samples, I constructed a dataset of actin images from Arabidopsis leaves with diverse morphology, and compared ILEE with numerous traditional global and local thresholding algorithms, including MGT. First, to evaluate the accuracy of each algorithm in terms of filament segregation, I manually

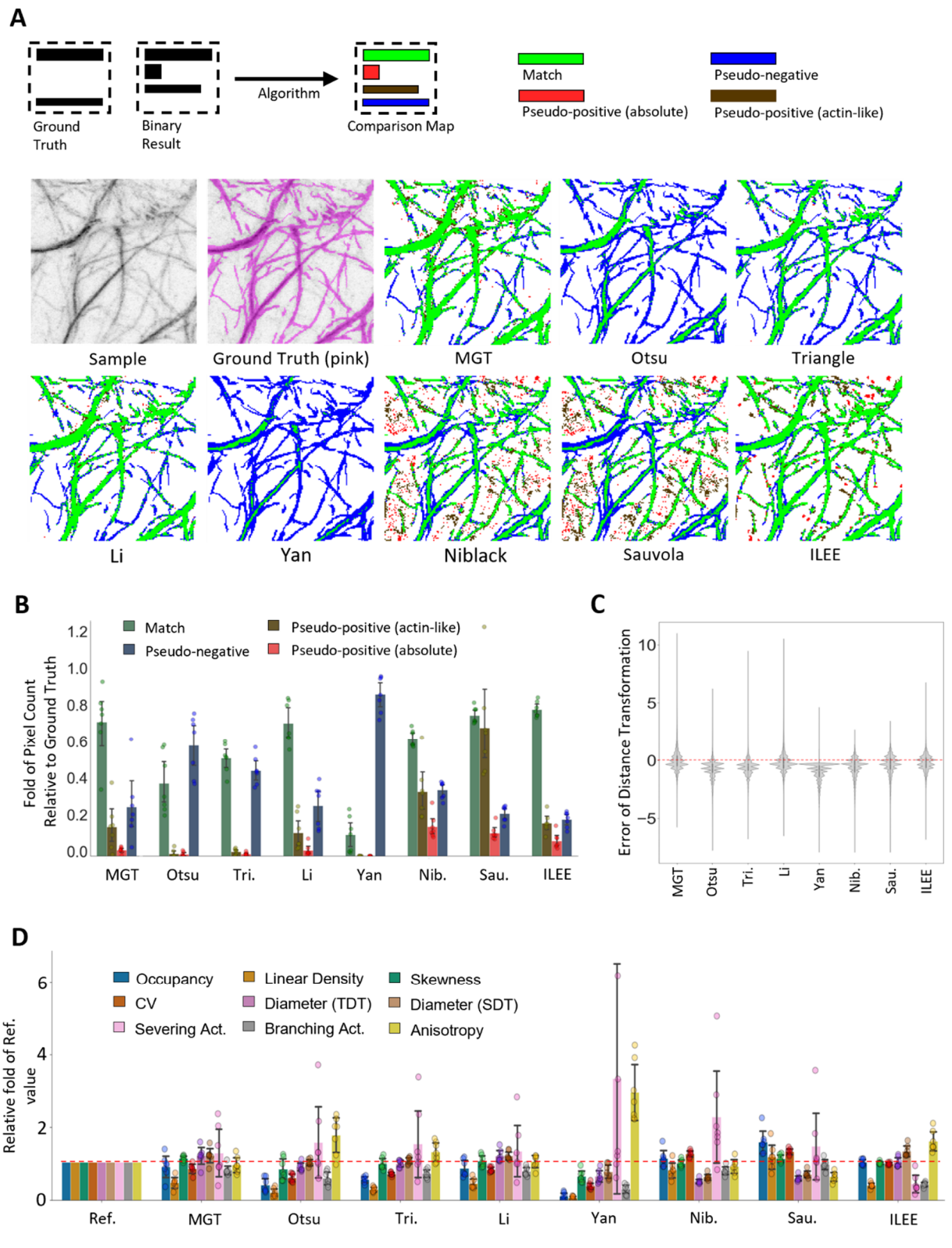

Figure 2-5: ILEE shows superior accuracy and robustness over classic thresholding approaches. The manually portrayed binary ground truth of 7 visually diverse selected samples…

Figure 2-5 (cont'd) … were compared with binary images rendered by ILEE, MGT, 4 global thresholding algorithms (Otsu, Triangle, Li, Yan), and 2 local thresholding algorithms (Niblack and Sauvola). **A**, Visualized comparison of ILEE versus other approaches. Pixels with different colors are defined as green: match of rendered binary image and ground truth; blue: pseudo-negative, the pixels omitted by the algorithm; red, absolute pseudo-positive, the pixels that are rendered by the algorithm but not in the ground truth, and are not within a filament-shaped component; brown, actin-like pseudo-positive, the pseudo-positive pixels within a filament-like component, which cannot be judged by high confidence. ILEE has the most accurate cytoskeleton segmentation.**B**, Quantitative comparison of pixel render demonstrating that ILEE has superior accuracy and stability across diverse samples. ILEE has the highest match rate and low and stable error rate, while MGT and Li also have acceptable performance. **C**, Comparison of distribution of distance transformation error. Single pixel errors of all 7 samples were merged and summarized as a violin plot. Red dashed line indicates no error, or results identical to the ground truth. ILEE has a symmetric and centralized distribution, indicating an accurate and unbiased filament segmentation. **D**, ILEE has accurate and robust computation of cytoskeletal indices. Nine indices computed using binary images rendered by different algorithms are compared with the ground truth. The index values are normalized to the fold of ground truth. Red dashed line indicates 1-fold, or identical to the ground truth.

generated the ground truth binary image from each of the *in planta* collected samples, using a digital drawing monitor (Figure 2-5A, ground truth). Next, I used each of the ground truth binary images as a reference and compared the filament architecture obtained by ILEE, MGT, and 6 additional adaptive thresholding algorithms. These additional thresholding algorithms include Otsu (Otsu, 1979), Triangle (Zack et al., 1977), Li (Li and Tam, 1998), Yan (Jui-Cheng Yen et al., 1995), Niblack (Niblack, 1985), and Sauvola (Sauvola and Pietikäinen, 2000) (Figure 2-5). As an additional element of rigor, because pseudo-positive pixels can be obtained due to user bias during the generation of each of the ground truth images (even when the operator is experienced in the actin imaging field), I further analyzed and categorized each non-connected component of pseudo-positive pixel by its shape and connectivity to matched elements and identified the actin-like pseudo-positive pixels as possible real actin components.

As shown in Figure 2-5A (visualized demonstration), 4B (quantitative analysis), and 4C (bias analysis), ILEE offers a superior performance, with the highest rate of accuracy with low pseudo-positive and pseudo-negative occurrence, as well as the lowest bias over local filament thickness. It is noteworthy, however, that the adaptive global thresholding approaches (from Otsu to Yan)

tend to be relatively accurate when judging the thick and bright bundles of the cytoskeleton. However, these approaches are unable to capture faint filaments, and as a result, generate a high pseudo-negative rate. Conversely, both adaptive local thresholding approaches, Niblack and Sauvola, generate numerous block-shaped pseudo-positive elements, and fail to capture the near-edge region of thick filaments. For MGT and Li method, although they showed satisfactory match rate, as well as lower averaged pseudo-positive/negative rates, their performance are far less stable than ILEE (Figure 2-5B).

As the next step in my analysis, I evaluated the accuracy and stability of cytoskeletal indices using ILEE versus other commonly used imaging algorithms. To do this, I first evaluated the ground truth indices from the manually generated binary images. In brief, quantitative measurements were collected from all methods and normalized by the relative fold to the result generated from the corresponding ground truth image. As shown in Figure 2-5D, ILEE showed improved stability compared to all other quantitative approaches and the highest accuracy for *occupancy*, *skewness*, CV, and *diameter_TDT*. However, in terms of the morphology-sensitive indices (i.e., *linear density*, *severing activity*, and *branching activity*), the ILEE algorithm did not fully conform with data collected from the ground truth binary images. Upon further inspection, I determined that this is because the manually portrayed ground truth images and ILEE results showed different tendencies in the judging the pixels in the narrow areas between two bright filaments (see *Discussion*). While other approaches displayed obvious, somewhat predictable, inaccuracies, the MGT and Li methods still generated satisfactory results, which echoes their performance in actin segmentation. However, the performance of these two algorithms among diverse and complex biological samples was not as stable as ILEE.

In order to further evaluate the stability and robustness of ILEE performance, I continued to analyze the variance coefficient of all groups (Figure AA-9), uncovering that ILEE is the only

approach which simultaneously maintained high accuracy and stability. Next, I tested the robustness of ILEE and other approaches against noise signal disturbance by adding different levels of Gaussian noise to the image dataset (Figure AA10-12). Using this approach, it was observed that ILEE was still the best performing algorithm, maintaining stable and accurate results of image binarization and cytoskeleton indices against increasing noise. Taken together, these results demonstrate that ILEE has superior accuracy, stability, and robustness over MGT and other classic automated image thresholding approaches in terms of both cytoskeleton segmentation and index computation.

ILEE leads to discovery of new features of actin dynamics in response to bacteria.

My primary impetus for the creation of the ILEE algorithm was to develop a method to define cytoskeleton organization from complex samples, including those during key transitions in cellular status. For example, our previous research has demonstrated that the activation of immune signaling is associated with specific changes in cytoskeletal organization (Henty-Ridilla et al., 2014, 2013; Li et al., 2017a; Lu et al., 2020). Complementary to these studies, other research identified the temporal and spatial induction of changes in cytoskeletal organization as a function of pathogen (e.g., *Pseudomonas syringae*) infection and disease development (Guo et al., 2016; Kang et al., 2014; Shimono et al., 2016b). The sum of these studies, which broadly applied MGT-based quantitative analysis of cytoskeleton architecture, concluded that virulent bacterial infection triggers elevated density (by *occupancy*) yet induced no changes in filament bundling (by *skewness*) in the early stages of infection. Since one of the major motivations herein was to develop an ILEE-based toolkit – supported by novel cytoskeletal indices – to investigate the process of pathogen infection and immune signaling activation, I collected raw data from a

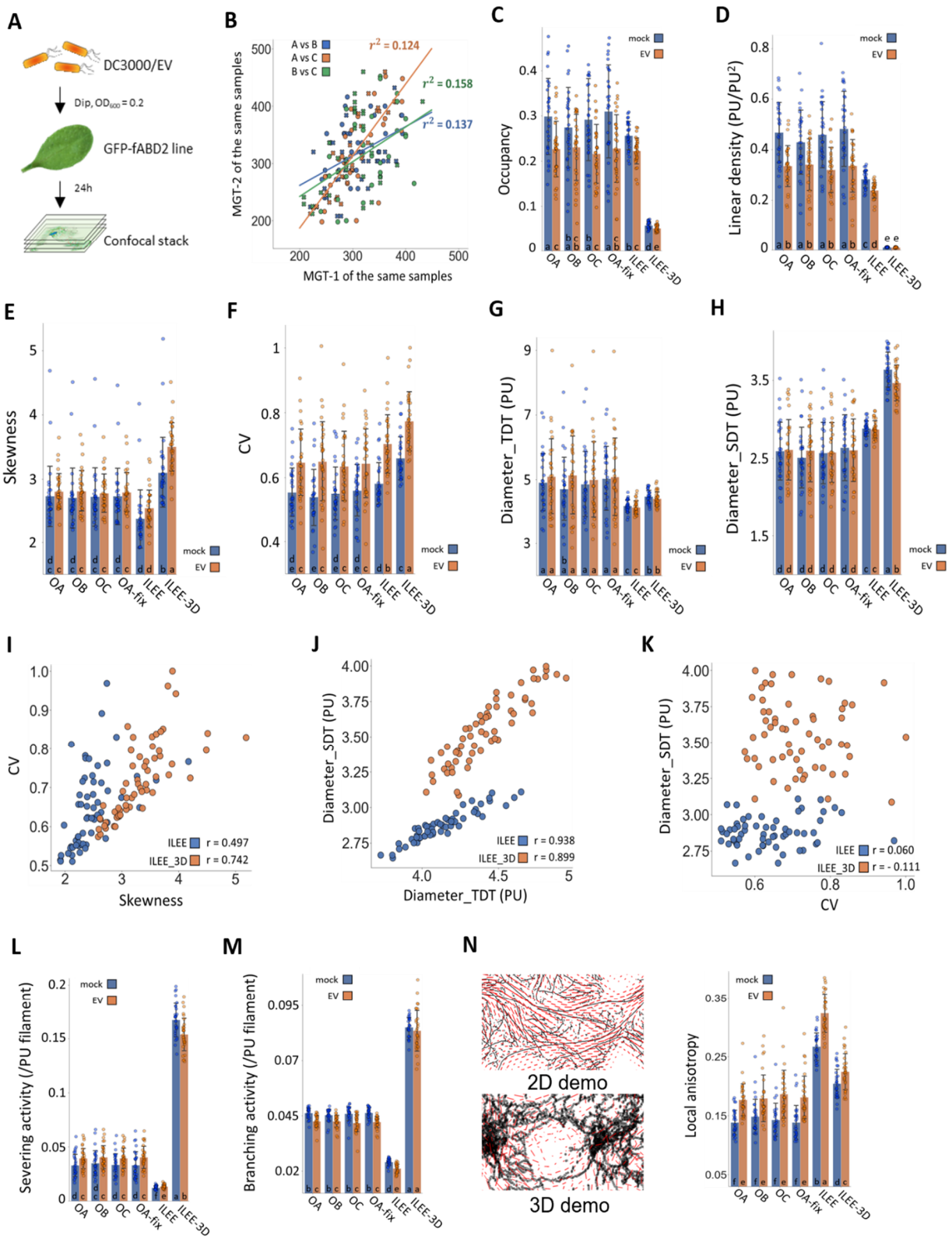

Figure 2-6: ILEE library enables the discovery of actin dynamic features of bacteria infected leaf tissue. Leaves of the Arabidopsis actin marker line Col-0/GFP-fABD2 were inoculated with mock or a…

Figure 2-6 (cont'd) … virulent bacterial pathogen, *Pseudomonas syringae* pv. tomato DC3000 with empty vector (EV, identical to wild type); images (*n* = 28 for mock, *n* = 31 for EV) of epidermal cells were captured by laser scanning confocal microscopy at 24 hours post-inoculation (hpi). MGT and ILEE were applied to generate binary images and all indices were computed using ILEE_CSK. Double-blinded samples were provided to 3 operators OA, OB, and OC for comparison. OA additionally provides data using a universal threshold (OA-fix). **A**, Experimental schematic diagram. **B**, Corelative comparison of MGTs of individual samples determined by different operators. A very low correlation between each pair of operators indicates MGT has an increased risk of bias and is potentially inaccurate. **C, D, E, F, G, H, L, M, N,** Output indices *occupancy*, *linear density*, *skewness*, *CV*, *diameter_TDT*, *diameter_SDT*, *severing activity*, *branching activity*, and *anisotropy*, respectively. Blue, mock; orange, EV. Multiple comparisons are conducted using a t-test without family-wise error correction (because image samples themselves are ground truth for all methods). Groups without overlapping letters have p_value lower than 0.05. For **n**, a visual illustration of the concept of local anisotropy is attached, where each red line segment points to the "averaged" direction of actin growth in the local area and the length shows the intensity of consistency of the direction. **I, J, K,** Comparisons of different indices in bundling class. *Skewness* and *CV* have medium-weak correlation; *diameter_TDT* and *diameter_SDT* have strong correlation; *diameter_SDT*, as a representative of direct indicator, and *CV*, as a representative of indirect indicator, have literally no correlation.

previous study (Lu et al., 2020) describing a bacterial infection experiment using Arabidopsis expressing an actin fluorescence marker (i.e., GFP-fABD2), followed by confocal imaging and data analysis by ILEE as well as MGT conducted by three independent operators (OA, OB, and OC) with rich experience in actin quantificational analysis (Figure 2-6). Additionally, because researchers sometimes apply a universal global threshold to all images from a batch of biological experiments to avoid tremendous labor consumption, I included this approach and aimed to observe its performance as well. In this experiment, the only categorical variant is whether sampled plants are treated with bacteria (EV) or not (mock). In total, nine indices that cover features of density, bundling, severing, branching, and directional order are measured and compared.

The first concern is whether bias generated by MGT will influence the result and conclusion generalized from raw image samples of the experiment. I thereby analyzed the correlation of individual MGT values set by the three operators and found only weak correlation between different operators (Figure 2-6B), which indicates MGT bias indeed has the potential to impact

quantitative results. Interestingly, while minor statistical discrepancies between MGTs by different operators are found in some indices (i.e., skewness and severing activity), most of the MGT results (both adaptive or fixed) shows the same trend as 2D ILEE, yet with far higher standard deviation, or lower stability (Figure AA-13A) over a certain biological treatment. This indicates that the historical data based on MGT should be majorly trustworthy despite the biased single data points, but an accurate conclusion must be based on high sampling number that balances the deviation of individuals. Since ILEE provides more stable results over biological repeats, I am also interested in whether it renders higher statistical power to identify potential significant differences. Therefore, I compared the p-values of t-tests conducted for each index (Figure AA-13B) and found that ILEE indeed has the superior statistical power to distinguish numerical difference over datasets. These aspects of evidence demonstrated ILEE as a better choice for actin segregation.

Next, I attempted to understand whether different indices of the same class, particularly density and bundling, can reflect the quantitative level of the class in accordance, or instead show inconsistency. For density, I correlated the *occupancy* and *linear density* values of all methods over actin images of both mock and EV groups, and found that *occupancy* and *linear density* measurements are in high conformity, with a Pearson coefficient at 0.98 (Figure AA-14). Interestingly, while both demonstrate high positive correlation, 2D ILEE and MGT do not share the same numeric relationship. Moreover, 3D ILEE has a weaker correlation, potentially due to cavities introduced by the skeleton image involved in *linear density* calculation. For bundling indices, I was interested in their level of conformity because direct indices (based on binary shape) and indirectly indices (based on relative fluorescence intensity) are completely different strategies to measure bundling. Using the same approach of correlating analysis, I found that *diameter_TDT* and *diameter_SDT* indeed display strong positive correlation, while *skewness* and *CV* have merely medium-low correlation, which echoes the previous report demonstrating *skewness* and *CV* have different performance on the bundling evaluation(Higaki et al., 2020). Unexpectedly, I

also found that *CV* (as a representative of indirect indices) and *diameter-SDT* (as a representative of direct indices) have a striking correlation of zero. This is perplexing, as it raises the question of whether *skewness* or *CV* should be regarded as an accurate measurement of bundling (see *Discussion*). This discrepancy is also reflected by the result of 3D ILEE, whose *CV* and *diameter-SDT* over mock versus EV reveals to the converse results at significant difference. In general, these results indicated that the biological conclusion that DC3000 treatment renders increased actin bundling level should be reconsidered with further inspection.

Last but not least, I sought to learn if additional features of plant actin cytoskeletal dynamics in response to virulent bacterial infection can be identified by the newly introduced indices and enhanced performance of ILEE. As shown in Figure 2-6D, significantly increased severing activity, local anisotropy, and decreased branching activity triggered by EV were observed, compared to the mock. At a minimum, these discoveries potentially lead to new biological interpretations, and as a result, may contribute to the identification of additional immune-regulated processes as a function of actin dynamics. However, while most of the 2D approaches were consistent and in agreement with the other indices, the severing activity estimated by 3D ILEE indicates a significant, but opposite, conclusion. After diagnosing the difference of each 2D ILEE and 3D ILEE sample, I concluded this is potentially due to information loss and misinterpretation by z-axis projection in the 2D-based approach. Therefore, it is not recommended to totally depend on the 2D mode for the analysis of filament severing at the current stage; a solid, clear conclusion awaits more data and insight from the community in the future.

ILEE has broad compatibility with various sample types

Cytoskeleton imaging from live plant samples is arguably one of the most difficult types of images to evaluate due to the dynamic topology and uneven brightness of actin filaments. While I demonstrated that ILEE shows a superior performance over plant actin samples, ILEE and the

ILEE_CSK library are generally designed for non-specific confocal images of cytoskeleton and are therefore applicable to other types of samples. To investigate the compatibility of ILEE to other types of image sample, I tested ILEE on both plant microtubules(Faulkner et al., 2017) and animal cell actin images (Figure AA-15). Importantly, I found ILEE can process, with high fidelity and accuracy, both plant and animal cytoskeletal features. This is encouraging, as animal cells generally possess a high volume of straight actin filament bundles, and therefore Hough transform-based feature detection is commonly applied to facilitate and/or enhance the performance of cytoskeleton segregation accuracy. However, this approach has certain limitations; specifically, they neglect and/or miscalculate curvy cytoskeleton fractions(Liu et al., 2020, 2018). With the advancement of ILEE, Hough transform will not be absolutely necessary, and the potential cytoskeleton indices that rigorously requires Hough transform can still utilize ILEE as a provider of binary image input for more accurate results.

In addition, images of single animal cell sometimes contain “void background” – areas that are truly blank without any cellular component. This is different from plant tissue whose total image field is sample area, which may negatively influence the accuracy of the computed indices. To solve this issue and further support animal cell sample, I developed a single-sell mode in the ILEE_CSK, which identifies the effective cell area using the statistical features of the brightness histogram, and hence secures accurate index output.

Finally, while ILEE was already tested on both of plant and animal image samples, the Github documentation website (https://phylars.github.io/ILEE_CSK/Help%20needed/) and ILLE_CSK main page are open for issue report (where ILEE cannot segregate cytoskeleton correctly). Such information greatly contributes to improving the compatibility of ILEE and the ILEE_CSK library in the future.

Discussion

Herein, I described the creation of ILEE, an accurate, stable, and robust filament segregation algorithm for the unguided quantitative analysis of the organization of the eukaryotic cytoskeleton. As presented, this approach supports the *in vivo* analysis of both 2D and native 3D data structures, enabling an unbiased evaluation of cytoskeletal organization and dynamics. In addition to the development of key methods, I also generated a publicly available Python library that supports the automated batch processing analysis of 13 filament indices from 5 classes of morphological features of the cytoskeleton. As described above, my data indicate that ILEE shows superior accuracy, robustness, and stability over current cytoskeleton image analysis algorithms, including the widely employed MGT approaches(Higaki et al., 2010; Lu and Day, 2017). As a result of these newly developed approaches, I, together with my team, have developed an open-access library to conduct ILEE based cytoskeleton analysis, which eliminates limitations imposed by popular 2D MGT approaches, including the introduction of user bias and information loss.

The gradient threshold (g_{thres}) defines the selected edge of actin filaments for implicit Laplacian transformation, the appropriateness of which greatly determines the performance of ILEE. To calculate g_{thres} without imposing a user-biased input, my strategy was to utilize feature values collected from NNES curve and human-guided MGT to train a prediction model for the rapid rendering of a coarse area of image background. Through this approach, I was able to deduce the corresponding g_{thres} by the mathematical relationship between the statistical distribution of the native pixel values and Scharr gradient magnitude of the coarse background (Figure AA-5, 6, 7, and *Methods*). This step might first appear unnecessary, since, alternatively, the most straight-forward strategy was to directly train a prediction model using the image gradient histogram and the human-determined g_{thres}. However, as the gradient operator (see *Methods*) for any given object pixel is influenced by the values of surrounding pixels, the calculated gradient on the edge

of the background is highly impacted (overestimated) by the contrast of foreground (cytoskeleton) versus the background. In other words, the frequency distribution of the background gradient will change at elevated cytoskeleton fluorescence levels, even though the background *per se* does not. The outcome of this is a significant decrease in the accuracy of gained g_{thres}. For this reason, I assert that g_{thres} should be mathematically deduced from a pre-determined region of background, rather than directly predicted via human-trained models, or calculated from a histogram of gradients using the pre-determined background.

The data generated in this study demonstrate that ILEE generally shows dominant robustness and accuracy for most of the indices when comparing to the manually portrayed ground truth binary image, but there are 3 indices (*linear density*, *severing activity*, and *branching activity*) where ILEE renders stable yet dramatically lower output than those derived from the ground truth images (Figure 2-5D). Since such inclination is very stable, I suspected this is due to certain systemic "bias" of the ILEE algorithm. After inspecting the binary images generated by ILEE compared with the ground truth, I identified a potentially critical reason: ILEE is less likely to presume unconfident branches inside the narrow space between two bright filaments. As demonstrated by Figure AA-16, while the ground truth and ILEE binary image look very similar, their skeleton images, which represent their topological structure, show contrast discrepancy between two bundles of bright filaments. Considering their procedure of generation, I speculate this is because: (1), ILEE fully outer-joins the binary results by a lower K_1 and a higher K_2 (Figure 2-3C), among which K_2 sacrifices the sensitivity to local filaments at high signal region to improve the sensitivity at low signal region, including the edge of thick filaments; and (2), human eyes tend to "hallucinate" imaginary filaments that do not statistically exist. Objectively speaking, there is no overwhelming evidence suggesting either 2D ILEE or the human eye is more accurate, as this comparison is conducted using 2D mode. However, 3D ILEE may solve this paradox because

most “adjacent” bright bundles are artifacts out of z-axis projection, which are distant enough in 3D space to offer ILEE with a satisfactory resolution to split.

For all indices, 2D ILEE agrees with MGT, while showing higher robustness and stability (Figure 2-6). However, this is not always the case for 3D ILEE. To understand this inconformity, I investigated the ILEE 3D algorithm as well as the rendered binary and skeletonized images. Based on the observation, I propose three key assertions: (1) the result of the 3D mode is a more accurate reflection of the nature of the cytoskeleton, as compared with the output of the 2D mode; (2) due to the limited computational power of most users’ personal computers, I did not introduce the oversampled binary image to compute the skeleton image for topological analysis, and therefore the accuracy of ‘*severing activity*’ and ‘*branching activity*’ may be negatively influenced; and (3) because of the 3D-specific sphere-cavity structures in the skeleton images, I used a different method to calculate *filament total length*, which indicates all indices that involve the *filament total length* in 3D mode are not strictly comparable to those calculated in 2D mode. Although the imperfectness due to reason (2) and (3) are solvable by improving the computational power of mainstream PCs and the skeletonization algorithm performance in the future, it is currently difficult to make a definite conclusion whether the current 2D or 3D mode is more accurate. Nonetheless, the 2D mode is inevitably an inaccurate and biased approach based on the nature of the image projection.

While ILEE has already remedied many disadvantages of traditional methods such as MGT, I, together with my collaborators, am still working to further advance the ILEE approaches presented herein. Our goal is to ultimately accomplish an analytic platform that provide highly trustworthy and informative results upon regularly updated ILEE algorithms as well as novel, representative indices. As such, I offer the following as an initial list of potential upgrades and applications to be integrated to our library:

- ILEE compatibility to *x-y-t* and *x-y-z-t* data, where *t* represents time. We are in the process of developing a 4D-compatible analysis of cytoskeletal dynamics that tracks filament organization over time. This approach will provide a temporal evaluation of supported indices with high accuracy and robustness.
- Deep learning-based cytoskeleton segmentation algorithm with “foreign object” removal. As presented herein, ILEE enables the generation of trustworthy binary images in large scale, which enables the construction of deep learning models to identify cytoskeleton components from confocal images with potentially better performance. The deep learning-based approach is also the key to solve the ultimate problem of all current cytoskeleton segmentation algorithms (including ILEE), which is the inability to detect and erase non-cytoskeleton objects with high fluorescence, such as the nucleus and cytoplasm. As one approach to circumvent this limitation, we are testing the feasibility of introducing 35S:mCherry as a cell-permeable false signal. This will enable us to further train our models to recognize and exclude the non-cytoskeleton-like foreign objects, to render ideally pure cytoskeletal datasets.
- Vectorized intermediate image. After generating the difference image (i.e., I_{dif}, Figure 2-3A) using ILEE, one computational limitation of the current algorithm is the tradeoff between the demand for unlimited high-resolution imaging versus limited computational power. Accordingly, an ideal strategy we propose is to transfer the pixel/voxel image to a 2D vector image or 3D polygon mesh for index calculation. We are currently working towards enabling this function at an acceptable requirement of computational power to further enhance the accuracy of ILEE.
- Regions of interest and organelle segmentation. There is currently a high demand in research of plant cell biology to quantify cytoskeletal parameters in stomatal guard cells, as well as additional plant cellular and subcellular architectures. In future releases of ILEE, we will

develop additional traditional and deep-learning approaches to enable recognition and selection of regions of interest, such as stomata, for various demand by the community.

Methods

Plant genotypes and growth

Arabidopsis thaliana Col-0 expressing the actin cytoskeletal marker GFP-fABD2 (Lu et al., 2020) was used in this study. Arabidopsis seeds were stratified for 2 d in the dark at 4°C then sown onto soil. All plants were grown in a BioChambers model FLX-37 walk-in growth chamber (BioChambers, Manitoba, Canada) at 20°C under long day conditions (16 h of light/8 h of dark) with 60% relative humidity and a light intensity of approximately 120 μmol photons $m^{-2}s^{-1}$.

Bacteria growth and plant inoculation

Pseudomonas syringae pv. *tomato* DC3000 (*Pst* DC3000) strains were grown as previously described (Lu et al., 2020). Antibiotics used in this study include kanamycin (GoldBio #K-120-5, 50 μg mL^{-1}), and rifampicin (GoldBio #R-120-1, 100 μg mL^{-1}). Bacterial treatments for actin dynamics analysis were conducted following previously described methods[36]. Briefly, 2-week-old Arabidopsis Col-0/GFP-fABD2 was dipped for 30s in Dip-inoculation solution (10 mM MgCl2 + 0.02% Silwet-77) with DC3000 with empty vector (EV) at a concentration OD_{600} = 0.2 (ca. 2 x 10^7 colony forming units/mL). Confocal images were collected at 24 hours post-inoculation.

Mouse cancer cells sample

Yale University Mouse Melanoma line YUMMER1.7D4 cells (EMD Millipore, #SCC243) were cultured in DMEM (ATCC # 30-2006) supplemented with 10% FBS (Gibco #10437-028), 1% Pen-strep (ThermoFisher, #15140122), and 1% NEAA (Gibco, #11140035). For staining actin stress

fiber, approximate 10,000 cells were seeded onto a glass coverslip maintained in a six-well plate overnight. First, semiconfluent cells were fixed with 3.7% formaldehyde for 15 min at RT, washed three times with PBS, then blocked in PBS supplemented with 2% BSA and 0.1% Triton for one hour at RT. Next, cells were incubated with 100 nM rhodamine-phalloidin (Cytoskeleton Inc, #PHDR1) in blocking buffer for 30 minutes at RT in dark, then washed with PBS three times each for 5 min with gentle shaking at RT. Stained cells on the coverslip were mounted in ProLong Glass Antifade Mountant with DAPI (ThermoFisher, #P36982). Slides were cured overnight at room temperature and were then imaged.

Confocal microscopy

For plant leaf actin images, 2-week-old Col-0/GFP-fABD2 plants were used for data collection and analysis. Images of epidermal pavement cells and guard cells were collected using laser confocal scanning microscope (Olympus FV1000D) by obtaining z-series sections at 0.5 μm intervals. Optical setting: 65x/1.42 PlanApo N objective with a 488 nm excitation laser and 510-575 nm emission filter. Images were collected at a resolution of 800 x 800 x 25 (*x*-*y*-*z*) and a 12-bit dynamic range. Voxel size was 0.132 μm at the *x*- and *y*-axis and 0.5 μm at the *z*-axis. For animal cell actin images, YUMMER1.7D4 stained by rhodamine-phalloidin were sampled by the same confocal system. Optical setting: 100x/1.40 UPLSAPO objective with a 559 nm excitation laser and 570-670 nm emission filter. Images were collected at a resolution of 800 x 800 x 10 (*x*-*y*-*z*) with voxel size of 0.039 μm at the *x*- and *y*-axis and 0.16 μm at the z-axis

Manually portrayed ground truth binary image

Seven raw projected images of 400x400 pixel size that have diverse visual appearance (e.g., actin density, shape, thickness, fluorescence brightness) were selected from the actin image database of my lab. Using a pen-drawing display (HUION KAMVAS 22 Plus, GS2202) and GIMP, we enhanced the brightness of low-value pixels to clarify the actin structure and carefully

portrayed the actin component of the selected image sample. The portrayed layer was extracted and transferred to binary format for further evaluation.

Double-blind MGT analysis

For the mock versus *P. syringae*-inoculated sample pool, we erased the sample name and randomized the order and distributed them to three independent scientists with rich experience in cytoskeleton analysis (referred to as OA, OB, and OC) to let them determine the global threshold value of each sample manually using the approach described previously[35]. Once completed, we restored the grouping of the samples for batch analysis. We use Python to mimic the MGT pipeline generally conducted by ImageJ after the determination of a specific thresholding value. OA also provided a universal threshold value (referred to as OA_fix) that applies to all samples as a commonly used fast MGT approach.

Statistical analysis and data visualization

All data analysis was conducted in the Python 3.8 environment and was described in figure legends.

Determination of K_2 for sample batches

For both 2D and 3D modes of ILEE, each 12-bit single-channel 3D image $I(x, y, z)$ in a batch of samples was transferred into 2D image $I_{proj}(x, y)$ by z-axis maximum projection, where each pixel $I_{proj}(x, y) = \max\{I(x, y, z)|z \in N^+, z < z_{max}\}$. I_{proj} was processed by a Niblack thresholding function[16] (library API reference [1]) to render $I_{nibthres}(x, y)$, with parameter k = -0.36 and $window\_size = 2\ int(25\ l) + 1$, where l is the mean of x and y resolution of I_{proj}. A binary image defined as $I_{binary}(x, y) = \{1, if\ I_{proj}(x, y) > I_{nibthres}(x, y); 0, else\}$ was generated. The binary image was processed through Euclidean distance transformation (library API reference

[2]), and the mean of the highest 5% values were used as the input of the K_2 calculation function (see Figure 2-3) that outputs individual recommended K_2. Finally, the mean of all individual K_2 will be output as the recommend K_2 for the total batch.

ILEE

An abbreviated workflow of ILEE is illustrated in Figure 2-3B. Here, we describe the overall process in further detail. For 2D mode, input image structure is $I(pix) = I_{proj}(x,y) = \max\{I(x,y,z)|z \in N^+, z < z_{max}\}$. For 3D mode, $I(pix) = I(x,y,z)$. First, I is treated by a significant difference filter (SDF; Figure AA-4) to render I_{SDF}, where:

$$I_{surround} = \{I(x \pm 1, y(,z)),\ I(x, y \pm 1(,z)),\ (0.293\ I(\mathrm{x,y(,z)}) + 0.707\ I(x \pm 1, y \pm 1(,z)))\}$$

$$I_{SDF}(x,y(,z)) = \begin{cases} I(x,y(,z)), & if\ |Mean(I_{surround}) - I(x,y(,z))| < 2\ STD(I_{surround}) \\ Mean(I_{surround}), & else \end{cases}$$

In other words, it substitutes a pixel by the mean of the 8 adjacent pixels if the absolute difference between it and that mean is higher than 2-fold of the standard deviation of the surrounding pixels. Then, I_{SDF} is input to a discrete gaussian filter with a 3x3(x3) weighting kernel at σ = 0.5, to render $I_{pre} = Gauss(I_{SDF})$, which is the smoothed pre-processed image. Since confocal microscopy has different resolutions on x/y and z axis (hereby named as U_{xy} and U_z), we adjusted the weighting kernel from O_{Gauss} to O'_{Gauss} in 3D mode particularly by a scaling operator, as below:

$$f = U_{xy}/U_z$$

$$O_{scalar} = \frac{3}{1+2f} \left[\begin{bmatrix} f & f & f \\ f & f & f \\ f & f & f \end{bmatrix} \begin{bmatrix} 1 & 1 & 1 \\ 1 & 1 & 1 \\ 1 & 1 & 1 \end{bmatrix} \begin{bmatrix} f & f & f \\ f & f & f \\ f & f & f \end{bmatrix} \right]$$

$$O'_{Gauss} = O_{Gauss} \circ O_{scalar}$$

From I_{pre}, the gradient magnitude image *G* is rendered through Scharr operator as:

$$G_x = \begin{bmatrix} 3 & 0 & -3 \\ 10 & 0 & -10 \\ 3 & 0 & -3 \end{bmatrix} * I_{pre}$$

$$G_y = \begin{bmatrix} 3 & 10 & 3 \\ 0 & 0 & 0 \\ 3 & -10 & -3 \end{bmatrix} * I_{pre}$$

$$G = \frac{\sqrt{G_x^{\circ 2} + G_y^{\circ 2}}}{32\sqrt{2}}$$

for 2D mode, or:

$$G_x = \begin{bmatrix} \begin{bmatrix} 9 & 0 & -9 \\ 30 & 0 & -30 \\ 9 & 0 & -9 \end{bmatrix} \\ \begin{bmatrix} 30 & 0 & -30 \\ 100 & 0 & -100 \\ 30 & 0 & -30 \end{bmatrix} \\ \begin{bmatrix} 9 & 0 & -9 \\ 30 & 0 & -30 \\ 9 & 0 & -9 \end{bmatrix} \end{bmatrix} * O_{scalar} * I_{pre}$$

$$G_y = \begin{bmatrix} \begin{bmatrix} 9 & 30 & 9 \\ 0 & 0 & 0 \\ 9 & -30 & -9 \end{bmatrix} \\ \begin{bmatrix} 30 & 100 & 30 \\ 0 & 0 & 0 \\ -30 & -100 & -30 \end{bmatrix} \\ \begin{bmatrix} 9 & 30 & 9 \\ 0 & 0 & 0 \\ -9 & -30 & -9 \end{bmatrix} \end{bmatrix} \circ O_{scalar} * I_{pre}$$

$$G_z = \begin{bmatrix} \begin{bmatrix} 9 & 30 & 9 \\ 30 & 100 & 30 \\ 9 & 30 & 9 \end{bmatrix} \\ \begin{bmatrix} 0 & 0 & 0 \\ 0 & 0 & 0 \\ 0 & 0 & 0 \end{bmatrix} \\ \begin{bmatrix} -9 & -30 & -9 \\ -30 & -100 & -30 \\ -9 & -30 & -9 \end{bmatrix} \end{bmatrix} \circ O_{scalar} * I_{pre}$$

$$G = \frac{\sqrt{G_x^{\circ 2} + G_y^{\circ 2} + G_z^{\circ 2}}}{256}$$

for 3D mode. Next, to calculate the gradient threshold (g_{thres}) as an input for ILEE, a global threshold t_{cbg} to determine the coarse background (I_{cbg}, as flattened image) is calculated by the NNES (non-connected negative element scanning) function that satisfies:

$$I_{binary.NNE}(x) = \{I(pix) | I(pix) > x\}$$

$$Count.of.NNE\left(I_{binary.NNE}(x_{peak})\right) = Count.of.NNE\left(I_{binary.NNE}(x)\right)_{max}$$

$$t_{cbg} = \begin{cases} 1.163\, x_{peak} + 101.68, & if\ I\ is\ 2D\ (\text{see Sup. Fig 1}\mathbf{b}) \\ 7.33\, x_{peak}, & if\ I\ is\ 3D\ (\text{see Sup. Fig 2}\mathbf{b}) \end{cases}$$

$$I_{cbg} = \{I(pix) | I(pix) \leq t_{cbg}\}$$

If *I* is processed using the 2D mode, as demonstrated previously (see Figure AA-5), the statistical mean and STD of gradient magnitude of I_{cbg} ($\mu_{G.cbg}$ and $\sigma_{G.cbg}$, respectively) are univariate proportional functions of the STD of I_{cbg}, σ_{cbg}, not influenced by the mean of I_{cbg}. Particularly, μ_G and σ_G, of the coarse background area of the gradient image is:

$$\mu_{G.cbg} = 0.8542\ \sigma_{cbg}$$

$$\sigma_{G.cbg} = 0.4469\ \sigma_{cbg}$$

With these, we established a g_{thres} estimation model, where g_{thres} = $\mu_{G.cbg}$ + *k* (σ_{cbg}) σ_G. Using the optimized parameters described in Figure AA-7, g_{thres} is deduced as:

$$k(\sigma_{cbg}) = 0.040018\ \sigma_{cbg}$$

$$g_{thres} = \mu_{G.cbg} + k(\sigma_{cbg})\ \sigma_{G.cbg}$$

If *I* is processed by the 3D mode, the inconformity of U_{xy} and U_z will not only impact the weighting of Scharr operator, but also influencing the proportional coefficient of σ_{cbg} to μ_G and σ_G. We simulated the accurate mathematical relationship between the proportional coefficient k_s and U_z/U_{xy} (see Figure AA-6), so g_{thres} for 3D can be calculated as:

$$\mu_{G.cbg} = k_{s.\mu}\, \sigma_{cbg}$$

$$\mu_{G.cbg} = k_{s.\sigma}\, \sigma_{cbg}$$

$$k(\sigma_{cbg}) = 0.040519\, \sigma_{cbg}$$

$$g_{thres} = \mu_{G.cbg} + k(\sigma_{cbg})\, \sigma_{G.cbg}$$

The total process above to computer g_{thres} is referred as function $g_{thres}.estimate(I_{pre},\ I_{cbg})$ in Figure 2-3A (1.3).

The critical step to generate the threshold image of the input sample *I* is implicit Laplacian smoothing. This algorithm builds a linear system using the Laplacian operator to achieve local adaptive thresholding based on edges of cytoskeletal components. Leveraging the spectral characteristics of discrete Laplacian operators, we could filter out high-frequency components (aka, high fluorescence fractions of cytoskeleton) while preserving the low-frequency salient geometric features of background fluorescence. First, an edge image is defined as $I_{edge}(pix) = I_{pre}(pix),\ if G(pix) > gthres; 0, else$, but we transform I_{edge} into a flattened image vector $\overrightarrow{I_{edge}}$, and hence it can be further be represented as:

$$\overrightarrow{I_{edge}} = S\, \overrightarrow{I_{pre}}$$

where *S* is a (sparse) selection matrix, which is a diagonal matrix with i-th diagonal entry being 1 if the i-th pixel has a gradient above g_{thres}.

Next, according to the concept of Laplacian operator, we constructed the (sparse) Laplacian matrix *L* that satisfies:

$$L = \begin{cases} L_4 \ \overrightarrow{I_{flt}} = \triangle_{p\_4} * I(x,y) & (2D\ alternative) \\ L_8 \ \overrightarrow{I_{flt}} = \triangle_{p\_8} * I(x,y) & (2D\ default) \\ L_6 \ \overrightarrow{I_{flt}} = \triangle_{p\_6} * I(x,y,z) & (3D) \end{cases}$$

where the Laplacian operators in different modes are defined as:

$$\triangle_{p\_4} = \begin{bmatrix} 0 & -1 & 0 \\ -1 & 4 & -1 \\ 0 & -1 & 0 \end{bmatrix}$$

$$\triangle_{p\_8} = \begin{bmatrix} -\sqrt{2}/2 & -1 & -\sqrt{2}/2 \\ -1 & 4+2\sqrt{2} & -1 \\ -\sqrt{2}/2 & -1 & -\sqrt{2}/2 \end{bmatrix}$$

$$\triangle_{p\_6} = \begin{bmatrix} \begin{bmatrix} 0 & 0 & 0 \\ 0 & -1 & 0 \\ 0 & 0 & 0 \end{bmatrix} \\ \begin{bmatrix} 0 & -1 & 0 \\ -1 & 6 & -1 \\ 0 & -1 & 0 \end{bmatrix} \\ \begin{bmatrix} 0 & 0 & 0 \\ 0 & -1 & 0 \\ 0 & 0 & 0 \end{bmatrix} \end{bmatrix}$$

Therefore, we can establish an implicit Laplacian linear system that targets the edge:

$$(L + kS)\ \overrightarrow{I_{thres}} = \overrightarrow{I_{edge}} = S\ \overrightarrow{I_{pre}}$$

where $\overrightarrow{I_{thres}}$ is the unknown to be solved by conjugate gradient method and restored to 2D/3D array I_{thres}, and *K* is a weight that adjusts the influence Laplacian operator has on the result (see Figure 2-3B).

Finally, a difference image I_{dif} is calculated as I_{dif} = $I_{pre} - I_{thres}$. To further clean the noise, a temporary binary image $I_{binary.temp}(pix) = \{1, if\ I_{dif}(pix) > 0; 0, else\}$ is generated and the sizes of all positive connected component (element) are counted. An adjusted difference image I_{dif_adj} is generated by lowering the values of potential noise into the mean of negative pixels:

$$I_{dif\_adj} = \begin{cases} I_{dif}(pix),\ if\ element\ size \geq 3 \\ Mean\big(I_{dif}(pix) \mid I_{dif}(pix) < 0\big), else \end{cases}$$

Using I_{dif_adj}, the various versions of the binary image for computation of different indices are calculated as:

$$I_{binary}(pix) = \{1, if\ I_{dif\_adj}(pix) > 0; 0, else\}$$

$$I_{binary.ovsp}(pix) = \{1, if\ Interp_{3,3}(I_{dif\_adj}(pix)) > 0; 0, else\}$$

for the 2D mode, where $Interp_{3,3}$ (I_{dif}) is an oversampled image by bicubic interpolation whose resolution on both x- and y-axis are upscaled for 3 folds, or

$$I_{binary.ori}(pix) = \{1, if\ I_{dif}(pix) > 0; 0, else\}$$

$$I_{binary}(pix) = \{1, if\ Interp_{1,1,1/f}(I_{dif}(pix)) > 0; 0, else\}$$

$$I_{binary.ovsp}(pix) = \{1, if\ Interp_{3,3,3/f}(I_{dif}(pix)) > 0; 0, else\}$$

for the 3D mode, where $Interp_{1,1,1/f}(I_{dif}(pix))$ aims to restore the voxel to cubic shape by only interpolate z axis to 1/*f* folds of its original resolution and $Interp_{3,3,3/f}(I_{dif})$ additionally enhance 3 folds of resolution for all three axes.

Computation of cytoskeletal indices

- ***Occupancy*:** the frequency of the positive pixels in the computed binary image, or $\sum I_{binary}(pix)/N$ for 2D mode and $\sum I_{binary.ori}(pix)/N$ for 3D mode, where *N* is the number of total pixels.
- ***Linear density*:** the length of the skeletonized filament per unit of 2D or 3D space. For 2D mode, $I_{binary.ovsp}$ is skeletonized using Lee's approach[18] to render the skeletonized image I_{sk} . Then, *linear density* is calculated as:

$$linear\ density = \sum length(x,y)/N.$$

$$length(x,y) = \begin{bmatrix} \sqrt{2}/2 & 1/2 & \sqrt{2}/2 \\ 1/2 & 0 & 1/2 \\ \sqrt{2}/2 & 1/2 & \sqrt{2}/2 \end{bmatrix} * I_{sk}(x,y)$$

  For the 3D mode, I_{sk} is rendered by I_{binary}, and we use the sum of the Euclidean lengths of all (graph theory defined) branches obtained by Skan library[22] as the total length of skeletonized filament and divide it by *N*. This is because sphere-cavities structures existent in the 3D skeletonized images are not applicable to the concept of length.
- ***Skewness*:** the (statistical) skewness of the fluorescence value of positive pixels, or mathematically:

$$skewness = \frac{1}{N_{pos}} \sum_{I_{binary}(pix)==1} \left(\frac{I(pix) - \mu_{pos}}{\sigma_{pos}} \right)^3$$

  where $\mathrm{N_{pos}}$, μ_{pos}, and σ_{pos} represents the count, mean, and standard deviation of positive pixels in the raw image I.
- ***CV*:** the (statistical) coefficient of variance of the fluorescence value of positive pixels, or mathematically:

$$CV = \frac{\sigma_{pos}}{\mu_{pos}}$$

- ***Diameter_TDT***: average filament diameter estimated by Euclidian distance transformation of total binary image. The Euclidian distance transformation map I_{dis} is calculated as an image with the same shape of $I_{binary.ovsp}$, but the value of each pixel is:

$$I_{dis}(x,y(,z)) = \begin{cases} \sqrt{\sum_{i=x,y(,z)} \left(i - i_{nnp}\right)^2}, & if\ I_{binary.ovsp}(x,y(,z)) = 1 \\ 0, & if\ I_{binary.ovsp}(x,y(,z)) = 0 \end{cases}$$

where i_{nnp} is the coordinates of the nearest negative pixel to (*x,y,z*). Therefore, the *Diameter_TDT* is mathematically defined as:

$$\textit{Diameter\_TDT} = \text{Mean } \{I_{dis}(pix) | I_{dis}(pix) > 0\}$$

- ***Diameter_SDT***: average filament diameter estimated by Euclidian distance transformation values of $I_{binary.ovsp}\ but\ sampled\ using\ only$ positive pixels on I_{sk}, or mathematically as:

$$\textit{Diameter\_SDT} = \text{Mean } \{I_{dis}(pix) | I_{sk}(pix) = 1\}$$

- ***Severing activity***: the count of connected components in binary image per unit length of skeletonized filament. For images captured in 2D mode, it is $Count.of.NNE\left(I_{binary.ovsp}\right)/\sum length(x,y)$. In 3D mode, both the count of non-connected elements and the length of skeletonized filament are called from the Skan library using I_{sk} computed from I_{binary} as the input.

- ***Branching activity*:** the branching point count per unit length of skeletonized filament. I_{sk} is obtained from $I_{binary.ovsp}$ for 2D mode or I_{binary} for 3D mode respectively and is next input into Skan library. The total number of type-3 and type-4 branches[22] is collected and then divided by the length of the skeletonized filament.
- ***Local anisotropy*:** We performed a local averaging of filament alignment tensor, which is constructed as follows. First, we calculate the unit direction vector for each straight filament segment g_i. Then, the covariance matrix for each segment is obtained from the following equation:

$$t_i = g_i g_i^t$$

This rank-2 tensor is independent of the orientation of the line segment, and can thus be averaged over a region containing a collection or unoriented line segments. We weight each filament tensor in a circular/spherical neighborhood by the length of every filament to produce a smoothed tensor field. The eigenvector corresponding to the largest eigenvalue indicated the primary orientation of filaments in this region. The difference between the maximum and the minimum eigenvalues is an indicator of the anisotropy in this region. If all the eigenvalues are the same, the indicator is 0, which implies an isotropic region. If the eigenvalues other than the maximum are all nearly 0, all the filaments in this region are parallel to each other. In this case, they are all aligned with the maximum eigenvector, the dominant filament direction of this region.

Methods Library API reference:

[1] https://scikit-image.org/docs/stable/api/skimage.filters.html#skimage.filters.threshold_niblack

[2]https://docs.scipy.org/doc/scipy-

0.14.0/reference/generated/scipy.ndimage.morphology.distance_transform_edt.html

Chapter 3: The nuclear-cytoplasmic function of actin depolymerization factors (ADFs) in plant Immunity

Chapter abstract

Plant immunity is a systemic response that immobilizes and integrates multiple signaling pathways, including the one that regulates the architecture of the actin cytoskeleton (a.k.a., actin remodeling). The general output of immune-triggered actin remodeling is related to the directionality of organelles and immune-related molecules to the host-pathogen interface, but it is unclear whether another important portion of the actin cytoskeleton – the nuclear actin and its associated proteins – is involved in the immune regulation. Besides, while previous studies revealed a genetic relationship between Arabidopsis actin depolymerization factors (ADFs), a group of actin-associated proteins, and the resistance against pathogens, they failed to explain why ADF seems to contribute to the pro-immune transcription and loses activity when exported from the nucleus. To answer these questions, my research herein focused on the identification of a novel activity of ADF – the capability to interact with WRKY transcription factors that control the pro-immune transcriptome. In this study, I proved that certain ADF can form a complex with WRKYs that bind to the targeted promoters, hence regulating the activity of WRKYs and playing a positive role in the immune response. In brief, ADF2/3/4 in the nucleus can interact with certain WRKY transcription factors, such as WRKY22/29/48, at the WRKY-regulated promoters in charge of immune genes. Further inspection discovered that ADF can enhance the activity of WRKY, stabilize it, and alter its targeting spectrum, a process that is potentially regulated by phosphorylation triggered by immune signaling. This work demonstrated that ADF moonlights as a direct TF regulator, which serves to mediate a pattern of the nuclear-cytoplasmic regulation on the plant immune response.

Introduction and rationale

Plants use a systemic strategy to fine-tune immune signaling, which requires cohesive cooperation between cytosolic and nuclear signaling cascades. Generally, the immune receptors locate in PM and cytosol, which release signal to fast, non-transcriptional "effectors" and simultaneously transduce the signal to TFs in charge of transcriptional reprogramming in the nucleus. Suppose we apply this model to the actin cytoskeleton; the vast majority of discoveries on the immune function of the actin cytoskeleton only reflect the fast cytoplasmic response – for example – immune-regulated actin reorganization to transport defense molecules to the pathogen-host interface. However, it is well acknowledged that actin and actin-associated proteins (ACPs) also play critical functions in the nucleus in the mammalian system, as aforementioned in *Chapter 1*. Therefore, it is possible that the nuclear actin cytoskeleton also plays a critical role in plant immunity, potentially working with cytosolic actin as a collaborative system under the regulation of immune signals.

While the nuclear function of actin and ACPs is rarely identified in either plant system or immune processes several previous studies indeed suggested the existence of this possibility. First, Arabidopsis ADF4 (Actin Depolymerization Factor 4) was previously reported to be critical for the robust expression of NB-LRR protein RPS5 (Porter et al., 2012). If the only molecular activity of ADF4 is to depolymerize/sever actin, it is difficult to conceptually link such function(s) to the nuclear event (i.e., regulation of *RPS5* expression). Second, as a more direct piece of evidence, subclass I ADFs of Arabidopsis (ADF1/2/3/4) have been shown to genetically contribute to resistance against powdery mildew (Inada et al., 2016) only when they enter the nucleus. However, the molecular mechanism(s) remains largely unknown. Regarding these, one of the most obvious potential mechanism(s) is that certain ADFs may be involved in the transcription events because ADF, by nature, can bind to actin, and actin is previously shown to function as a

scaffold for the transcription pre-initiation complex and chromatin remodeling (Wei et al., 2020; Kyheröinen and Vartiainen, 2020). If this hypothesis is proven valid, then a novel nuclear-cytoplasmic mechanism of plant immune regulation will be revealed, conceptually linking the cytosolic and nuclear actin cytoskeleton as a collaborative signaling platform. Moreover, rather than being limited to the framework of plant immunity, such a regulatory pattern may generally apply to eukaryotes and other signaling pathways, which introduces a new perspective to understand cytoskeleton functionality.

Based on the hypothesis and preliminary evidence above, I hereby propose that Arabidopsis ADFs have moonlighting functions in the nucleus, which contributes to immunity and potentially involves the nuclear actin cytoskeleton. To broadly test this hypothesis, I designed and conducted a series of experiments to identify the nuclear function of Arabidopsis ADFs, as introduced in *Chapter 3* below in detail. In brief, I found that certain nuclear ADFs can interact with certain WRKY transcription factors and form an ADF-WRKY-DNA complex at the WRKY-regulated promoters of immune response genes. ADF can enhance the activity of WRKY, stabilize it, and alter its targeting spectrum. At the same time, this event is regulated by phosphorylation that prohibits its actin severing/depolymerization activity while enhancing the WRKY-boosting activity, triggered by immune signaling. The work presented herein demonstrated that ADFs moonlight as direct TF regulators, which serves as a critical piece of the jigsaw puzzle to envision the nuclear-cytoplasmic function of the actin cytoskeleton.

Results

WRKY transcription factors are potential ADF interactors

As introduced above, previous studies had suggested the possibility that ADF4 may contribute to the immune response in a manner related to unknown transcriptional regulation in the nucleus

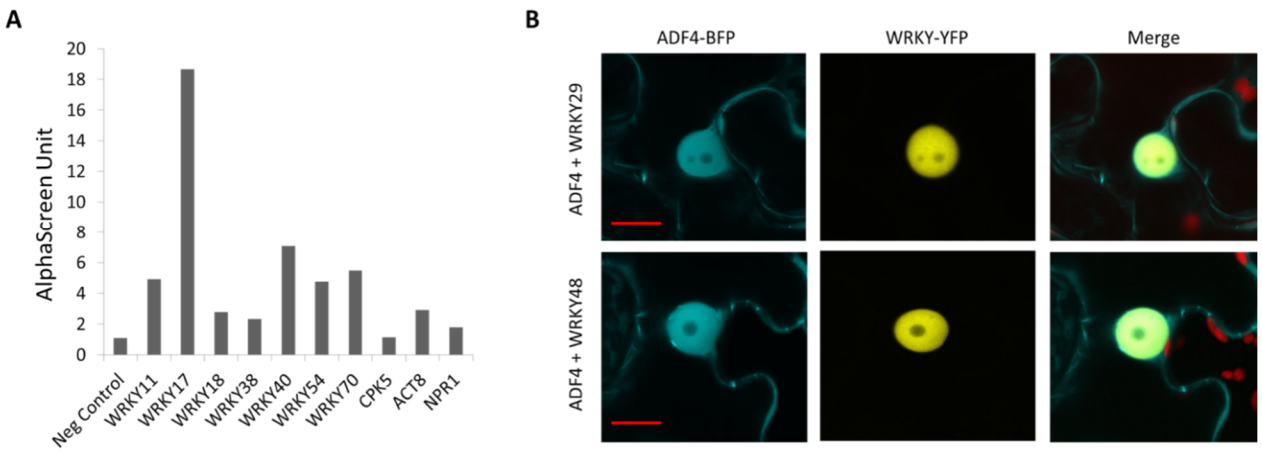

Figure 3-1: AlphaScreen and co-localization assay reveal potential existence of ADF-WRKY interaction. A, AlphaScreen of ADF4 interactor. Bi-luminescence fusion of ADF4 and selected genes are co-expressed in a wheat germ cell-free system to detect potential interaction. Relatively high signal in some WRKY samples are observed. **B**, nuclear co-localization of ADF4 and WRKY29/48. ADF4-BFP and WRKY-YFP are co-transformed into *N. benthamiana* leaves by Agro-infiltration. While ADF4 exist in both cytoplasm and nucleus, a perfect nuclear ADF-WRKY co-localization *in planta* is visible.

(Inada et al., 2016; Porter et al., 2012). Therefore, one possibility is that ADF participates in certain pro-immune transcriptome reprogramming events mediated by TFs that control this process. Driven by this hypothesis, a previous doctoral student, Alex Corian of the lab, conducted an amplified luminescent proximity homogeneous assay (AlphaScreen; Nomoto, Tada, and Tsukagoshi 2019) to screen for ADF4 interactors, using selected genes known to involve in plant immunity. This method uses a wheat germ cell-free system to co-express ADF4 and candidate proteins to detect the interaction intensity via a bi-luminescence approach. As a result, several members in the WRKY gene family are revealed as potential interactors of ADF4 (see Figure 3-1A). As WRKYs are plant-specific TFs generally regulating the stress response (Birkenbihl et al., 2017), it is reasonable to suspect that the moonlighting function of ADF in the immune response is mediated by particular ADF-WRKY interaction. However, because both the accuracy and specificity of the AlphaScreen result was uncertain, and the selected candidates, ADF4 and the

seven WRKYs, may not represent the general properties of members in their protein families. Therefore, I initiated this project to examine the hypothetic nuclear function of Arabidopsis ADFs. As a preliminary attempt to confirm whether ADF is (at least partially) a nuclear protein, I conducted a subcellular co-localization assay using ADF4 and WRKYs. Specifically, ADF4, WRKY29, and WRKY48 are cloned to Agrobacteria binary vector containing 35S::-BFP or 35S::-EYFP fusion, respectively, to transform *N. benthamiana* leaf for observation. As demonstrated in Figure 3-1B, ADF4, as a representative member of the ADF/cofilin family, displayed both cytoplasmic and nuclear signal. The robust nuclear signal co-localized with WRKY29 and WRKY48, which indicates that ADF4 indeed exists in the nucleus, spatially allowing it to interact with members of the WRKY family.

The Expression pattern of ACT, ADF, and WRKY

The introduction and preliminary study above suggest that ACT, ADF, and WRKY may form a complex interactome to mediate any pattern of nuclear-cytoplastic regulation. This is because all three groups – actin, ADF/cofilin, and WRKY – have an intricate protein family in terms of isoform numbers of expression pattern, and this approach cannot confirm which among them are critical or typical interactor pair(s) for biological function. Particularly, Arabidopsis has 11 ADFs (6 expressed in leaf; Ruzicka et al. 2007), 12 ACTs (3 expressed in leaf; 2 pseudogenes; McDowell et al. 1996), and more than 74 WRKYs (Li et al., 2020b). Hence, to study their joint function, my first step was to select members as representative candidates.

Since our organismic platform is Arabidopsis, the primary strategy is to understand which members of these families are expressed in Arabidopsis rosette leaf, our major experimental material. Therefore, I conducted a preliminary screening by analyzing leaf transcriptome datasets under PTI and ETI conditions using bioinformatic approaches. Briefly, the wild-type (Col-0) portion of the published mRNA-seq datasets GSE85932 (Birkenbihl et al., 2017; describing leaf tissue

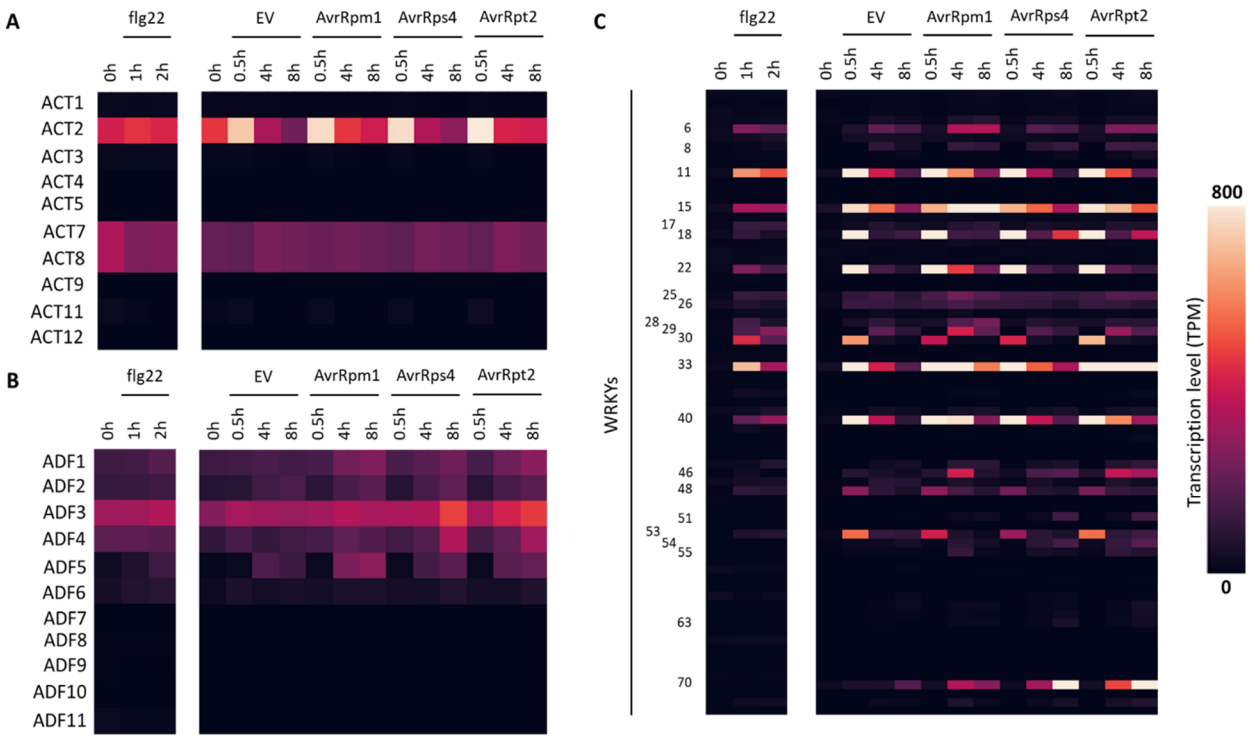

Figure 3-2: Expression pattern of all ACTs, ADFs, and WRKYs in Arabidopsis leaves upon immune signaling. Arabidopsis mRNA-seq dataset GSE85932, of flg22 (PTI inducer) treated Col-0 leaf, and GSE151885, of (a/)virulent bacteria (ETI inducer) treated Col-0 were downloaded, trimmed by Trimmomatic, and the reads were quantified by Salmon, using Galaxy platform. ACT2/7/8 (**A**) and ADF1/2/3/4/5/6 (**B**) are constitutively expressed; multiple WRKYs (**C**, marked by numbers) are induced by PTI and/or ETI signal.

upon PTI signaling) and GSE151885 (Saile et al., 2020; describing leaf tissue upon ETI signaling) were downloaded, cleaned, and evaluated, as presented in Figure 3-2. It is clear that ACT2/7/8, ADF1/2/3/4/5/6, and dozens of WRKYs are capable of being expressed in the leaf. For ADFs, most of these members are relatively constitutive if not minorly up-regulated, except for ADF5, which can be significantly up-regulated ~6 fold by both PTI and ETI signals. For ACTs, all three follow a pattern of up-and-down pattern, while ACT2 meets the peak earlier than ACT7/8. Besides, the amplitude of transcriptional regulation is not very high, as actin is commonly regarded as a constitutive expresser. These data generally align with the early studies of expression patterns observed by traditional approaches (McDowell et al., 1996; Ruzicka et al., 2007). For WRKY,

Selected WRKYs in this study

Gene	Group*	Involved Immune Processes
W4	Ia	Susceptibility to virulent *P. syringae* and Botrytis
W33		Resistance against Botrytis
W8	Ib	ETI; susceptibility to virulent *P. syringae*
W28		Potentially ETI
W48		ETI; susceptibility to virulent *P. syringae*
W18	IIa	Susceptibility to virulent *P. syringae* and powder mildew
W40		
W6	IIb	-
W11	IIc	Susceptibility to virulent *P. syringae*; ISR by rhizobacteria
W17		
W22	IId	PTI ; Resistance to *P. syrinage* after water submerge
W29		PTI
W30	IIIa	-
W46		Basal defense
W70		SA-JA Crosstalk; Resistance against *P. syringae* and *Hyaloperonospora parasitica*
W38	IIIb	Susceptibility to virulent *P. syringae*

*Based the phylogenic relationship measured by the sequence of WRKY domain (Wu et al., 2015).

Table 3-1: selected WRKYs and their phylogenic groups. WRKY candidates for interaction analysis are selected based on a comprehensive consideration of expression pattern, coverage of all categorical groups, and reports of genetic function(s) in immunity. See reference in the text.

most of those expressed in leaves are greatly induced by both PTI and ETI. While some rapidly boost and reach the peak within 30-60 min post-treatment and then fast decay, others are up-regulated in the later phase. Such pattern conforms with the general identities of WRKYs – anti-stress TFs with a multi-phase network.

The preliminary candidates for ADF-WRKY interaction by molecular approaches are selected according to the expression above. For the ADF side, ADF1/2/3/4/5/6 are chosen because they are significantly expressed in the leaf; for the WRKY side, I additionally considered their reported genetic functions, and made sure that all subgroups of members in this family are covered by at

least one representative (Lai et al., 2008; Zheng et al., 2006; Gao et al., 2013; Hsu et al., 2013; Hu et al., 2012; Journot-Catalino et al., 2006; Schön et al., 2013; Asai et al., 2002; Kim et al., 2008), as summarized in Table 3-1. The strategy above made sure that representative interactors with potential significant function are included at the best possibility.

The interaction specificity of Arabidopsis leaf ADF-WRKY interactome

To understand the interaction specificity of ADF and WRKY on a large scale, I decided to use semi-quantitative BiFC to directly evaluate the interaction levels of ADF-WRKY pairs. To prepare, all selected ADFs and WRKYs, aforementioned in the previous section, are cloned from Arabidopsis cDNA into BiFC vectors pM1089 or pH1097 for fusion with MYC-nEYFP(nY) or HA-cEYFP(cY), respectively. First, nY-ADF4, together with similar quantities of each of the individual WRKYs, was co-transformed into Arabidopsis protoplast. Afterward, the multiple images at a large scale with low magnification were taken by confocal microscope. The interaction intensity is measured by total BiFC fluorescence per unit of chlorophyll fluorescence, as a normalized matrix. As shown in Figure 3-3A, half of the WRKY candidates showed visible interaction (descending group greater than “e”) with ADF4, while their interaction intensities had contrast variation. Herein, I define WRKY29/22/48 as strong interactors and WRKY6/8/18/28/33 as medium interactors. Interestingly, strong and medium interactors concentrated in certain WRKY clades (e.g., clade Ib and IId), indicating that such interaction is structure-based, and certain features in these clades are responsible for this interaction. Herein, I choose WRKY29 and WRKY48 as primary and secondary objectives of the study, as these strong interactors can represent two different cases of Clade Ib and IId in the WRKY family.

Next, to understand the interaction specificity among the Arabidopsis leaf-expressed ADFs, I conducted a similar BiFC assay using each individual of ADFs in combination with either of WRKY29, 40, and 48, wherein WRKY29/48 are strong interactors, and WRKY40 is a non-

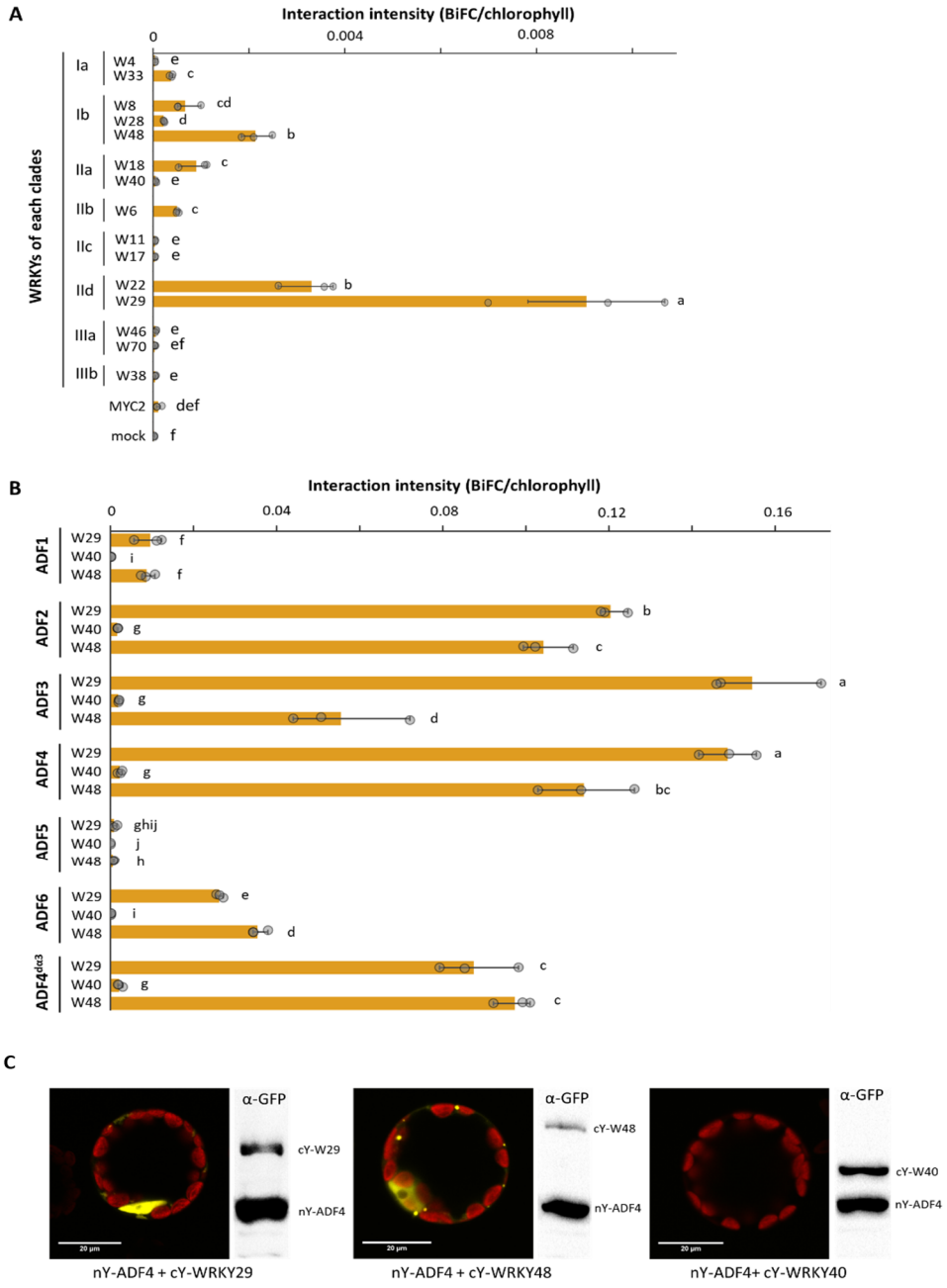

Figure 3-3: ADF-WRKY interaction intensity of selected family members of Arabidopsis. Vector containing nY-ADF4 and cY-WRKY are co-transformed into Arabidopsis protoplast. Photos (n=3) of large scale (low magnification), covering closely distributed protoplasts are captured 12h post-transformation. The BiFC (YFP) fluorescence per unit of chlorophyll fluorescence is used to measure interaction intensity (see *Method*). Non-overlapped alphabet indicates significant difference, defined as one-way ANOVA with $p < 0.001$ followed by multiple comparison of t-test corrected by Benjamini–Hochberg method with $p < 0.05$. **A,** ADF4 interaction intensities with selected WRKYs covering all phylogenic clades of WRKY family of Arabidopsis. **B,** WRKY29/48 interaction intensities with leaf-expressed ADFs. **C**, classic demonstration of BiFC by single protoplast fluorescence. The α-GFP (for eYFP fractions) indicates both WRKY and ADF4 is robustly expressed. Bar = 20 μm.

interactor as a negative control, as illustrated before. In addition, in order to understand whether the ADF-WRKY interaction requires ADF to interact with ACT simultaneously to form a triplex, I constructed an ADF4 mutant, ADF4-R91A/K93A, referring to previous studies (Du et al., 2016; Tanaka et al., 2018). Theoretically, this mutant is not able to interact with ACT because the two mutated residues disrupted the hypothetical ACT-ADF interaction interface. Therefore, I name this mutant as ADF4$^{d\alpha3}$ (for "disrupted alpha-helix III"). If ADF4$^{d\alpha3}$ can interact with WRKYs, it indicates the ADF-WRKY interaction does not necessarily require ACT (as a scaffold). As shown in Figure 3-3B, all of ADF2/3/4 showed strong interaction with WRKY29/48 and no interaction with WRKY40. Also, ADF6 was a medium interactor; ADF1 was a weak interactor; ADF5 was absolutely a non-interactor. Since all ADFs displayed no differentiation of interaction pattern among three WRKYs, it is deducible that the interaction pattern of WRKY29/48 with positive ADFs are the same. Also, it is noticeable that ADF4$^{d\alpha3}$ still had a high interaction intensity at a level close to wild type ADF4, which indicates that ADF-WRKY interaction represents a moonlighting independent from classic ADF-ACT interaction.

ADFs interact with WRKY-DNA complex

The studies above identified a strong interaction between WRKY29/48 and ADFs, which leads the question to the outcome of this interaction from the perspective of their molecular functionality. Here, I hypothesized that ADFs can regulate the activity of targeted WRKYs by such physical interaction. According to current knowledge, the primary function of WRKYs is mediating transcription as a TF that binds to the W-box motif ((T)TGAC(C/T)) in the promoter sequence of stress-responsive genes (Jiang et al., 2017a). Hence, one of the potential approaches for ADF to impact WRKY activity is to regulate in the WRKY-mediated transcription initiation. It is important to understand whether the ADF-WRKY complex can occur while WRKY binds to its objective promoters.

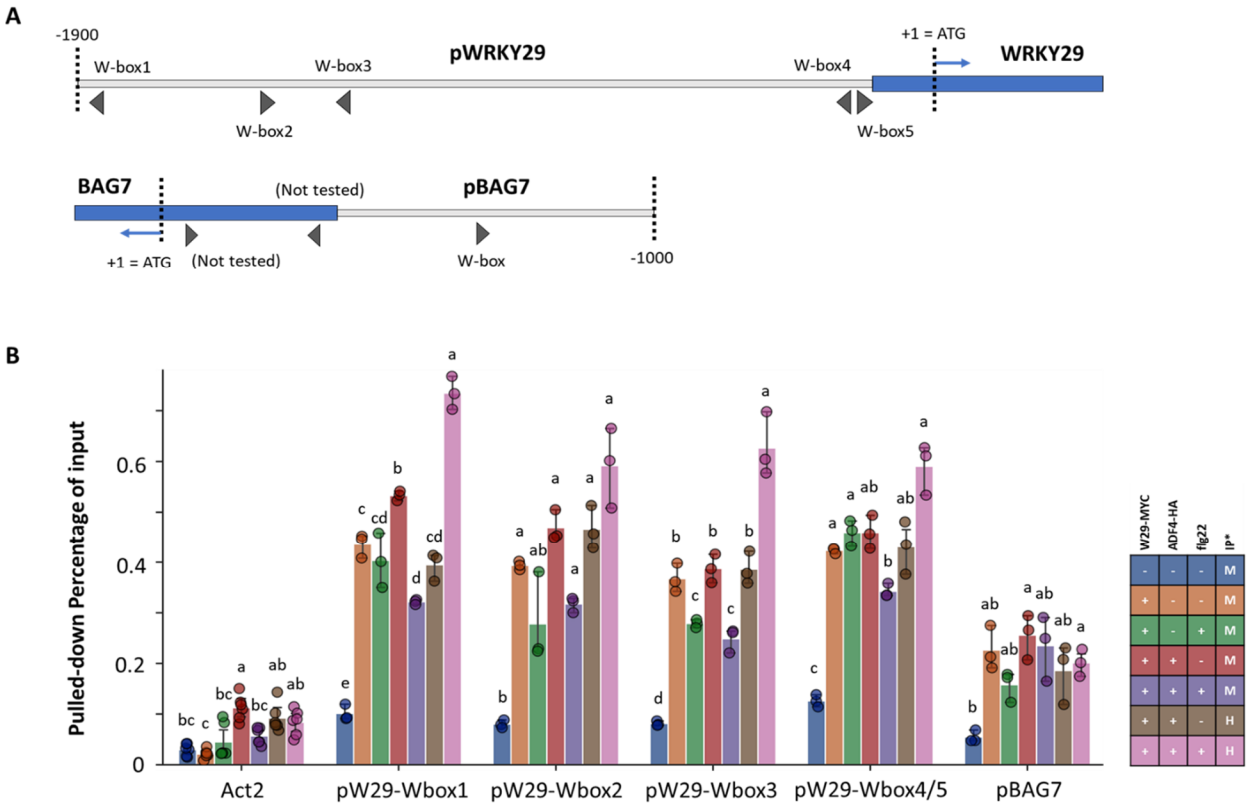

Figure 3-4: ADF4 co-localizes with WRKY29 on WRKY29-targeted promoters. A, distribution of W-boxes in the promoter of WRKY29 and BAG7. The existence of W-box (WRKY-binding motif) in the promoter of these genes suggest the potential of WRKY-regulated gene expression. **B**, ChIP-qPCR to detect quantify of DNA fraction of hypothetic WRKY-targeted promoters. Combinations of W29-MYC and ADF4-HA are transformed into the protoplast of *wrky29/adf4* double mutant, and α-MYC(M) or α-HA(H) ChIP are then conducted. Both pW29 and pBAG7 are targeted by WRKY29, and ADF4 also binds to these promoter together with WRKY29. Act2 is a general negative control. Non-overlapped alphabet indicates significant difference defined as ANOVA of $p<0.001$ followed by t-test with Benjamini-Hochberg correction of $p<0.05$. Error bar means 95% confidence interval.

To answer this question, I conducted a chromatin immunoprecipitation (ChIP) experiment using protoplast co-expressing ADF4 and WRKY29, the primary candidate pair of strong interaction (Figure 3-4). Multiple combinations using ADF4-HA and/or WRKY29-MYC are co-transformed into *adf4/wrky29* double mutant, and the samples are harvested to crosslink the DNA with adjacent protein by formaldehyde to pull down the DNA fractions that interact with ADF4/WRKY29, which can be measured by qPCR. There was no systemic study published to elucidate the

objective genes regulated by WRKY29, so it was unclear which promoter fractions would be tested to verify whether ADF4 and WRKY co-localize on the chromatin. However, it was previously reported that WRKY18/40/60 use a self and cascaded negative feedback mechanism to prevent excessive expression (Liu et al., 2012). Accordingly, it is possible that WRKY29 also utilizes such mechanism by binding to the promoter of WRKY29 (pW29). Therefore, I searched the promoter of WRKY29 (pWRKY29/pW29) and found 5 W-boxes (see figure 3-4A). For each of them, a pair of qPCR primers with high specificity was designed to cross the W-box. Additionally, in a study focusing on AtBAG7, a ER-nuclear co-chaperone involved in unfolded protein response, it was reported that WRKY29 can bind the promoter of BAG7 (Li et al., 2017b), so I included the W-box identified in pBAG7 as another potential pull-down targeted by WRKY29 and ADF4 (see Figure 3-4A).

As shown in Figure 3-4B, each of the W-box fractions in pW29 was significantly enriched by IP of WRKY29-MYC, when compared with the negative control groups Act2 and the mock (shown as blue). This demonstrated that WRKY29 indeed binds to the W-boxes in its own promoters, and further verified the technical feasibility of this experiment. Interestingly, when co-expressing WRKY29-Myc and ADF4-HA, both α-HA and α-Myc IP were able to significantly enrich the same pW29 fractions, which indicated that WRKY29 and ADF4 not only bind to each other, but also form a complex together with DNA – the W-boxes targeted by WRKY29. In addition, because sometimes pro-immune transcription requires specific immune signal(s) as a trigger, I also included the treatment of flg22 as a variable. However, the impact of flg22 was not obvious and stable, which suggested that the PTI signal is not a prerequisite to trigger the ADF4-WRKY29-DNA interaction at the experiment condition. However, the possibility was not excluded that this interaction can be enhanced by specific immune signal(s) when ADF4 and WRKY29 are not overexpressed. Another potential target of WRKY29, pBAG7, was also generally enriched, but

the amplitude was minor, and some groups did not show a significant difference, which indicates the W-box affiliation of pBAG7 was not as strong as pW29 in the experimental condition.

Certain ADFs enhance the transcription promoting activity of WRKYs

Since the study above suggested that the ADF-WRKY interaction occurs on the promoter of the WRKY-regulated genes, it is natural to conceptually associate such interaction to the regulation of activity of corresponding WRKYs. In order to test whether the activity (i.e., the capability of transcription activation) of WRKY is alternated by the strong ADF interactors, I designed a promoter reporter system to track the activity of WRKY in the presence/absence of ADFs.

The promoter reporter system is comprised of 3 vectors, which contains 35S::WRKY-BFP, 35S::ADF-RFP, and GFP driven by WRKY-targeted promoter, respectively (see Figure 3-5A). When the GFP reporter vector is co-transformed with the combinations of WRKY-BFP and/or ADF-RFP into protoplasts, all three fluorescence signals can be measured by confocal microscopy to get quantitative data at a large scale like semi-quantitative BiFC, and therefore the differentiated levels of GFP can be explained as a result of different transcription enhancing function of corresponding ADFs. For WRKY29, I still used pW29 and pBAG7 to drive the GFP expression, as these two promoters were proved to interact with WRKY29 in the section above. At the same time, I introduced pW48 (potential self-regulation) and pW46 (Gao et al., 2013) to drive the GFP expression for measurement under the regulation of ADF-WRKY48 complex. Null mutant *wrky29* and *wrky48* were used as the source of protoplast to eliminate the background WRKYs that were unmeasurable.

As expected, WRKY29 was able to significantly boost the expression of pW29::GFP, and ADF4 up-regulated the transcription activation capability when co-transformed with WRKY29. Similarly, WRKY48 was able to trigger the expression of pW48::GFP and pW46::GFP, while the activation on pW46 was far more robust than pW48, which suggested that WRKY48 may play critical

function in the activation of pW46 by its nature. As for pBAG7, although it can be significantly up-regulated at the presence of both WRKY29 and ADF4, there was only a ~2.5 fold upregulation, which indicates pBAG7 was not a target of WRKY29 at the experiment condition, the same as suggested by the ChIP-qPCR experiment (Figure 3-4).

Next, I substituted ADF4 in the reporter system with each of the individual ADF candidates. Besides ADF1/2/3/4/5/6, I also introduced ADF-NLS (fusion protein of ADF-BFP-FLAG-NLS) and ADF-NES (ADF- BFP-FLAG-NES), where NLS/NES stands for "nuclear localization/export signal". These signal peptides can compel the protein to be imported into or exported from the nucleus, thereby rendering almost complete nuclear/cytoplasmic localization, which assists in evaluating the contribution of nuclear ADF to the transcription activation by WRKY. In addition, ADF4$^{d\alpha 3}$ was also included to understand whether this activity requires actin as a co-factor.

As shown in Figure 3-5C, ADF2, ADF3, and ADF4 indeed enhanced the transcription activation activity of WRKY29, while ADF1 and ADF5 showed a lower transcription level compared with the WRKY-only group in the absence of ADF. At the same time, the ADF4-NLS group had the highest expression level among all the groups, which fully supports the hypothetic mechanism that ADFs enhance the function of WRKY by directly binding WRKY at the targeted promoters inside the nucleus. However, ADF4-NES also got a relatively high reporter signal like ADF4, which was confusing. After a thorough inspection into the dataset, I found the most probable reason was that the ADF-NES group had twice the cell number and three times the total WRKY quantity compared to ADF4, which might generate certain levels of inaccuracy when simply comparing the GFP level normalized by chlorophyll fluorescence. Besides, ADF4$^{d\alpha 3}$ was also able to enhance the activity of WRKY29 a level identical to ADF4, indicating that the WRKY enhancement activity of ADF4 does not require the physical interaction with ACT at the same time, which echoed the result of

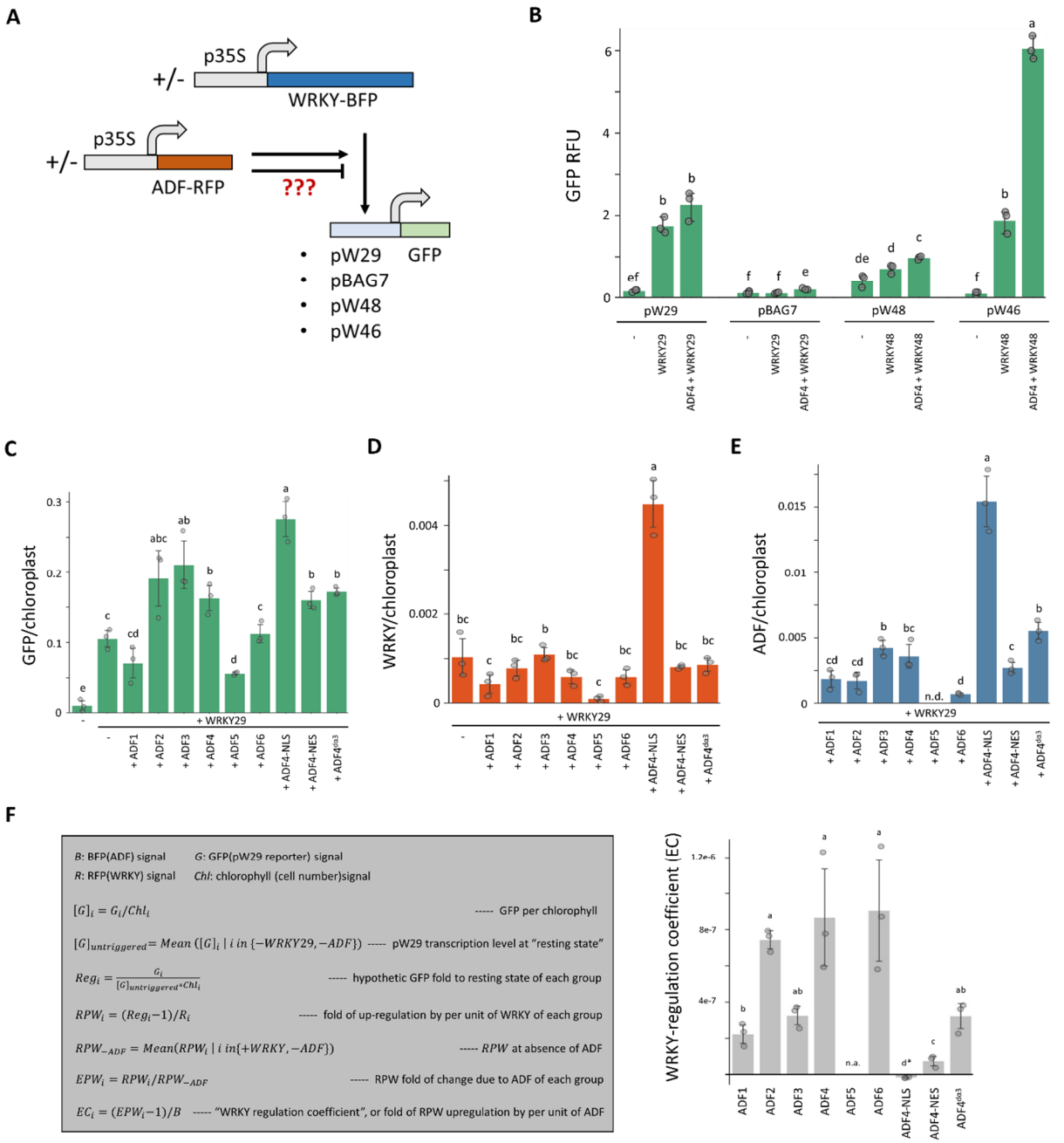

Figure 3-5: ADF can boost the transcription activation capability of interacted WRKYs. Non-overlapped alphabet indicates significant difference defined as ANOVA of p<0.001 followed by t-test with Benjamini-Hochberg correction of p<0.05. Error bar means 95% confidence interval. **A**, design of promoter reporter system using GFP driven by WRKY targeted promoters. **B**, ADF4 is able to boost the activity of both WRKY29 and WRKY48. *adf4* protoplast was used to lower the background level of ADF4. **C**, WRKY29 activities upon treatment of multiple ADF variants. ADF2/3/4/dα3 can strongly enhance the activity of WRKY29. Nuclear-exclusive ADF4 has higher activity to enhance WRKY function than wild type or cytoplasmic-exclusive ADF4. **D, E**, the expression level of WRKY29 and ADF of **C**. **F,** the mathematical model of WRKY enhancing coefficient (EC) to estimate the normalized activity of per unit of ADF to per unit of WRKY.

the BiFC conclusion that ADF-WRKY interaction does not require ACT in the complex (Figure 3-3B).

In order to further inspect whether the expression level of the pW29-driven GFP is comparable, I also computed the expression level of WRKY29 and ADFs of each group. As illustrated in Figure 3-5D, while the expression level of WRKY29 was similar in most groups, it turned significantly low when co-expressed with ADF1 or ADF5, and the ADF-NLS group were significantly high. On the other hand, the ADF expression levels were not perfectly identical among all groups (Figure 3-5E). Over a comprehensive consideration on these data, it is concluded that ADF2/3/4, as strong WRKY interactors, have the capability of enhancing the activity of WRKYs. However, they may have a stabilizing effect on WRKY simultaneously, which explains why the weak interactor ADF1 and non-interactor ADF5 rendered relatively low WRKY expression.

To avoid worse tangled situations of quantitative interaction of the three components, I did not change the quantity of protoplast and three transformed vectors of individual groups – which had been rigorously controlled – to re-balance the ADF and WRKY expression. Instead, I designed a mathematical model to further dissect the contribution of ADF to boost the activity of WRKY by defining a WRKY enhancement coefficient (EC), which evaluates the impact of per unit of ADF on per unit of WRKY, as an index reflecting the nature of ADFs regardless of the quantity of ADFs and WRKYs. The mathematical definition is stated in Figure 3-5F. In brief, this approach subtracts the non-WRKY-triggered transcription of each group and computes how much fold enhancement of WRKY-triggered transcription was due to per unit of ADF, compared to the absence of ADF. As shown, the trend of EC generally conformed with the expression level of pW29::GFP (Figure 3-5C) but with certain adjustments. First, ADF6 got an unexpected high EC while ADF3 and ADF4$^{d\alpha 3}$ got lower than ADF2 and 4. As these differences were not significant, one of the potential possibilities is that these differences were generated by the amplified error of measurement and

nonlinear relationship between the florescence and protein quantity in the model. Second, ADF4-NLS and ADF4-NES both got low EC. While the situation of ADF4-NES may reflect the fact that cytoplasmic ADF cannot effectively enhance the activity of WRKY, the abnormal value of the NLS group actually suggested that ADF4 and WRKY29 concentration (Figure 3-5D, E) reached the saturation level for a limited quantity of pW29 promoter. Hence, the data did not contradict the conclusion that ADF actually enhances the WRKY activity in the nucleus.

In summary, the data above support the hypothetic mechanism that certain ADF can enhance the transcriptional activation capability of interactive WRKYs. These ADFs include ADF2, ADF3, and ADF4, which are exactly the strong WRKY interactors, indicating that the direct physical interaction can explain the enhancement of the activity of WRKYs. It is highly possible that ADF contributes to plant immunity by this mechanism, in addition to mediating actin remodeling in the cytoplasm, as aforementioned in *Chapter 1*.

ADF4 stabilizes the interacted WRKYs

As shown in Figure 3-5D, E above, a trend emerged that when a strong ADF interactor of WRKY reached high quantity in the sample, the expression level of WRKY would also gain a relatively high level. This phenomenon suggests a possibility that ADF may be able to stabilize the WRKY that it interacts with, which serves as another potential mechanism for ADF to enhance the overall function of WRKYs. Similarly, in an inspection of protein expression level for the aforementioned BiFC experiment (Figure 3-3B) by western blot, I also repeatedly observed an increased quantity of cY-WRKY29 when co-transformed with strong interactor ADF4, but not the non-interactor ADF9(Figure 3-6A). However, this observation may not be rigorous enough to deduce any solid conclusion, because the fluorescence protein fractions in the fusion protein introduce an extra weak interaction affinity that may have unpredictable impact(s).

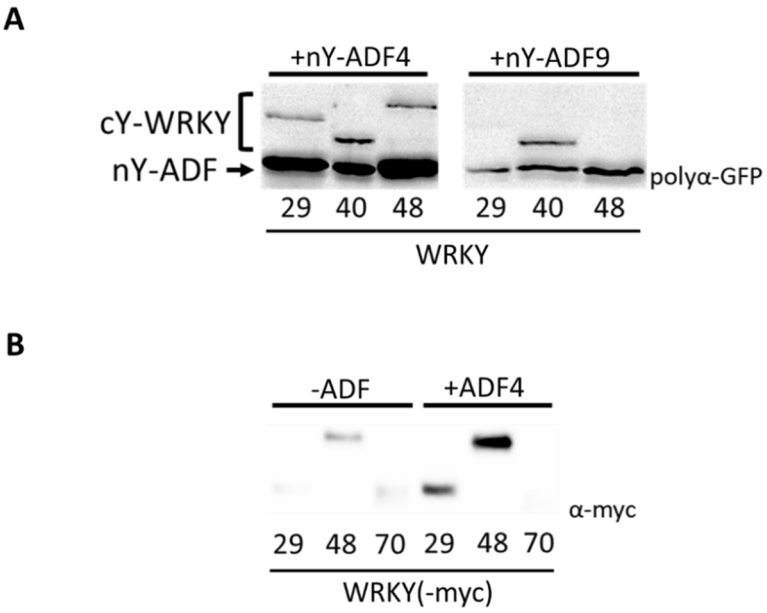

Figure 3-6: ADF4 can stabilize interacted WRKY exclusively. A, WRKY and ADF level of *adf4* protoplast samples transformed by BiFC vectors expressing nY-ADF and cY-WRKY. **B**, WRKY and ADF level of adf4 protoplast sample expressing WRKY-MYC at the presence or absence of ADF-HA. Small epitope tag minimizes unknown impact of fusion fractions. For both data, ADF4 can stabilize its strong interactor WRKY29/48, but not its non-interaction WRKY40/70.

In order to confirm whether the stabilization effect by ADF exists, I used the protoplast system to co-transform the combinations of 35S::WRKY-MYC and 35S::ADF4-HA to measure the protein quantity by western blot. The simple epitope tag can minimize the influence of the introduced fusion structure, ensuring that any experiment result is caused by the nature of WRKY and ADF *per se*. As a result, ADF4 indeed enhanced the expression of the strong interactor WRKY29 and WRKY48, but not the weak interactor WRKY70. Given that all proteins are expressed via the constitutive *35S* promoter, whose transcription rate is stable, the simplest interpretation of such result is that ADF4 can indeed stabilize its interactive WRKYs from degradation. While other ADFs are not tested, they potentially follow that same pattern as ADF4: obvious stabilization effect exists between any ADF-WRKY pair with strong interaction. Therefore, the stabilization effect is indeed one of the mechanisms for ADFs to enhance the total activity of WRKY. As previously discussed

in the description of the EC model (Figure 3-5F), currently it is very difficult to dissect the contribution of the stabilization effect from the total activity enhancement of WRKYs by ADF at ideal accuracy, but the gross activity of strong WRKY interactors is indeed boosted by strong ADF interactors as a result of their physical protein-protein interaction.

Nuclear ADF4 contributes to resistance against pathogen

The studies above demonstrated that the ADF-WRKY interaction enhances the transcriptional activation activity of WRKY, and strong interactors are identified as ADF2/3/4 and WRKY29/48. Because WRKY29/48 and other interacted WRKYs are stress-responsive TF that mediate pro-immune transcriptome reprogramming, it is reasonable to ask whether ADF indeed contributes to plant immunity by such mechanism.

To prepare the material to inspect the genetic function of nuclear ADF using ADF4 as a representative, I screened and finally obtained an *adf4-2* mutant that is Col-0 background and free of a contaminated exon insertion on AT1G77500, from the ABRC seed line SALK_121647. Then, *adf4-2* was back-crossed with Col-0 to further clean the background. Then, 35::ADF-BFP-FLAG-NES/NLS were transformed into *adf4-2*, and two T2 homozygous lines with stable expression of NES/NLS-tagged ADF4 were selected to test their resistance against pathogen.

Because previous reports suggested that the *adf4* mutant has impaired resistance against *Pseudomonas syringae* pv. tomato DC3000 expressing the avirulent effector AvrPphB (DC3000/AvrPphB), I also chose DC3000/AvrPphB as the test pathogen to infect Arabidopsis. As shown in Figure 3-7, *adf4-2* supported increased bacterial growth compared with WT Col-0, which can be complemented by expressing ADF4 in the nucleus but not the cytoplasm. This result indicates that ADF4 indeed contributes to the ETI against AvrPphB only when a certain level of ADF4 exists in the nucleus, rather than cytoplasm, at the experimental condition. The conclusion

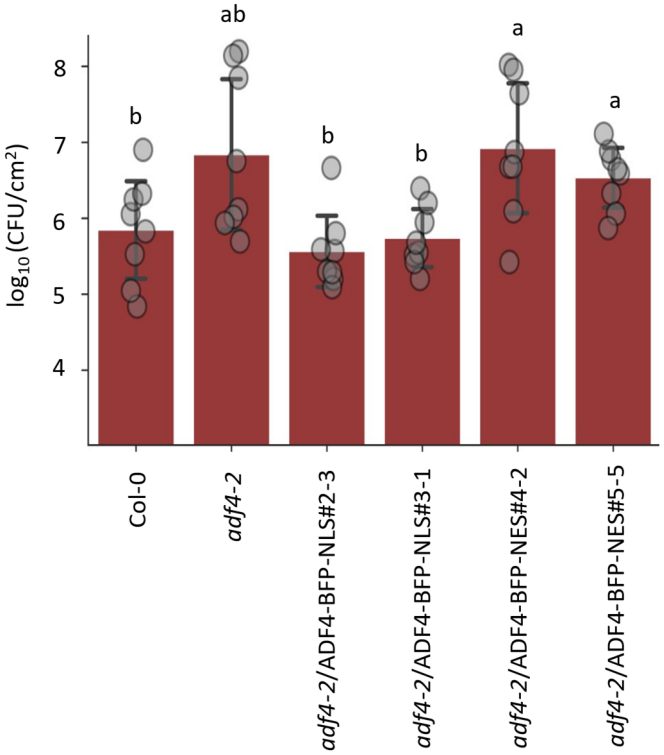

Figure 3-7: Bacteria growth assay of nuclear and cytoplasmic-exclusive complementation lines of ADF4. Two independent lines of homozygous adf4/35S::ADF4-BFP-FLAG-NLS/NES, which expresses ADF4 with nuclear localization/export tag were constructed. DC3000/AvrPphB of 10^6 CFU is inoculated by hand infiltration and bacteria growth is measured 3dpi (n=8). ADF-NLS, rather than NES, can significantly enhance the resistance against AvrPphB. Non-overlapped alphabet indicates significant difference defined as ANOVA of $p<0.001$ followed by t-test with Benjamini-Hochberg correction of $p<0.05$. Error bar means standard deviation.

agrees with the proposed molecular mechanism that ADF4, and potentially ADF2 and 3, function in plant immunity by interacting with and enhancing the function of WRKYs.

To further inspect and evaluate genetic function(s) of ADFs in greater detail, a series of high-order ADF mutants have been under construction, using CRISPR/Cas9 system. The proposed plan and current process are described in *Appendix A*.

ADF4, while binding WRKY29, targets immune-regulatory genes genome-widely and regulate WRKY29 activity and targeting spectrum

It is revealed in the studies above that nuclear ADFs contribute to plant immunity potentially by interaction with WRKYs to enhance their transcriptional activation function. However, while the interaction pair of WRKY29-ADF4 was deeply inspected, it is difficult to further explore the mechanism of the immune functionality of the ADF-WRKY complex with current knowledge, because the function of WRKY29 remains largely unknown. Therefore, to directly solve this problem and clarify the contribution of WRKY29 and ADF4 in plant immunity, I constructed a *wrky29/adf4* double mutant line and conducted a series of ChIP-seq assays using protoplasts system derived the mutant.

In brief, this experiment uses a strategy similar to the ChIP-qPCR experiment but a simpler experiment setting (Figure 3-8A): the transformation of ADF4-HA only for α-HA IP (cyan), transformation of WRKY29-MYC only for α-MYC IP (green), and co-transformation of WRKY29-MYC and ADF4-HA for both α-MYC and α-HA IP (purple and red). The experiment was biologically repeated 3 times, and the results were merged and screened before analysis. As the first study that systematically reveals the targeting spectrum of WRKY29, I have identified totally 3704 WRKY29 targeted genes that passed the screening filter (see Figure 3-8A). When ADF4 was co-transformed with WRKY29, the coverage of the WRKY29-targeted gene expanded, and ADF4 also gained the ability to bind the promoters of WRKY29 simultaneously.

Next, to determine whether WRKY29 and ADF4 tend to bind DNA as a complex, I conducted a quantitative co-localization analysis by correlating the quantity of promoter fractions pulled down by WRKY29 and ADF4. As shown in Figure 3-8B, there is a strong positive linear correlation between the WRKY29 pulled-down fraction and ADF4 pulled-down fraction among all the shared

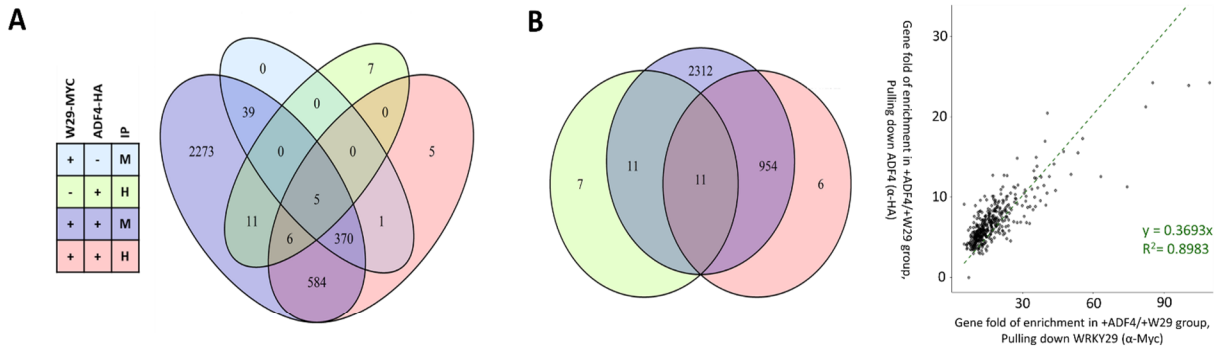

C

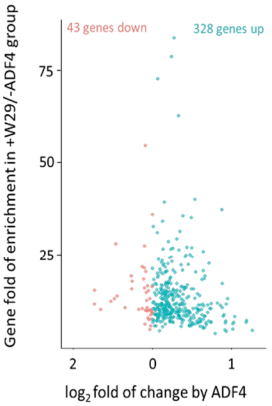

Top-15 enriched genes with up-reg. affinity to ADF4

TAIR_ID	Gene	FoE
AT1G51800	IOS1	90.51
AT1G30690	PATL4	85.1
AT1G61470	CAF1-5	78.63
AT1G51880	RHS6	67.82
AT1G72520	LOX4	43.47
AT1G11310	MLO2	42.67
AT1G61380	SD129	40.53
AT1G11190	ENDO1	38.72
AT4G31500	CYP83B1	38.1
AT1G62300	WRKY6	37.1
AT3G51380	IQD20	35.56
AT1G65520	ECI1	34.13
AT4G03510	RMA1	33.73
AT4G01250	WRKY22	31.91
AT2G23320	WRKY15	31.1

Genes of top-15 genes up-reg. affinity to WRKY29

TAIR_ID	Gene	FoC
AT3G50610	CEP9	2.398
AT4G16780	HAT4	2.284
AT3G48360	BT2	2.277
AT3G15520	CYP37	2.053
AT5G45090	PP2A7	2.037
AT2G17520	IRE1A	2.027
AT2G32800	LECRKS2	2.024
AT5G05340	PER52	1.933
AT3G56310	AGAL3	1.914
AT1G52300	RPL37B	1.911
AT3G61310	AHL11	1.901
AT2G26950	MYB104	1.893
AT5G54380	THE1	1.887
AT1G74430	MYB95	1.876
AT5G60740	ABCG28	1.858

Top-15 enriched genes with down-reg. affinity to ADF4

TAIR_ID	Gene	FoE
AT5G39040	ABCB27	59.11
AT4G19960	KUP9	39.09
AT2G25470	AtRLP21	29.81
AT5G11100	SYTD	30.55
AT1G78870	UBC35	23.68
AT1G17420	LOX3	23.24
AT1G61620	CSU1	22.14
AT1G35350	PHO1-H8	19.92
AT4G01720	WRKY47	17.75
AT1G68370	ATJ15	20.91
AT1G55970	HAC04	18.1
AT4G39940	APK2	17.39
AT1G76930	ATEXT4	19.29
AT3G13380	BRL3	16.65
AT5G37600	GLN1-1	16.14

Genes of top-15 genes down-reg. affinity to WRKY29

TAIR_ID	Gene	FoC
AT5G64410	OPT4	0.601
AT2G25230	MYB100	0.602
AT2G24220	ATPUP5	0.636
AT4G00900	ECA2	0.694
AT3G23820	GAE6	0.715
AT5G11100	SYTD	0.725
AT3G51670	PATL6	0.735
AT4G31820	NPY1	0.787
AT1G68370	ATJ15	0.831
AT2G24200	LAP1	0.833
AT1G76930	ATEXT4	0.836
AT2G32100	OFP16	0.885
AT1G78870	UBC35	0.915
AT3G24480	LRX4	0.915
AT1G35350	PHO1-H8	0.924

D

Selected Enriched pathway by WRKY29 targeted genes

GO ID	Pathway	Gene Ratio	Background Ratio	p-value	p.adjust	q-value
GO:0010200	response to chitin	25/385	141/21845	3.66E-18	2.6E-15	2.12E-15
GO:0002376	immune system process	34/385	417/21845	1.27E-13	3.61E-11	2.96E-11
GO:0045087	innate immune response	31/385	365/21845	5.46E-13	1.29E-10	1.06E-10
GO:0042742	defense response to bacterium	34/385	442/21845	6.7E-13	1.36E-10	1.11E-10
GO:0006955	immune response	31/385	379/21845	1.47E-12	2.62E-10	2.14E-10
GO:0052542	defense response by callose deposition	8/385	29/21845	2.69E-08	3.82E-06	3.12E-06
GO:0009682	induced systemic resistance	8/385	30/21845	3.61E-08	4.66E-06	3.81E-06
GO:0009620	response to fungus	22/385	336/21845	1.54E-07	1.82E-05	1.49E-05
GO:0050832	defense response to fungus	19/385	266/21845	2.9E-07	3.07E-05	2.51E-05
GO:0052482	defense response by cell wall thickening	6/385	17/21845	3.03E-07	3.07E-05	2.51E-05
GO:0009814	defense response, incompatible interaction	16/385	202/21845	6.46E-07	6.11E-05	5E-05
GO:0052545	callose localization	8/385	44/21845	8.81E-07	7.82E-05	6.39E-05
GO:0012501	programmed cell death	13/385	141/21845	1.34E-06	0.000112	9.13E-05
GO:0009611	response to wounding	16/385	216/21845	1.57E-06	0.000117	9.6E-05
GO:0009753	response to jasmonic acid	15/385	199/21845	2.68E-06	0.00019	0.000156
GO:0008219	cell death	14/385	178/21845	3.51E-06	0.000238	0.000194
GO:0009751	response to salicylic acid	12/385	161/21845	2.98E-05	0.001514	0.001238

Figure 3-8: ChIP-seq identifies of genome-wide target of WRKY29 and the enhancement of WRKY29 promoter bind by ADF. Combinations of vector expressing WRKY29-MYC and ADF4-HA are transformed into protoplasts of wrky29/adf4 double mutant. DNA fractions bond to ADF/WRKY are pulled-down following Illumina sequencing. **A**, Venn diagram showing the overlapping of different samples. 415 and 3704 targets of WRKY29 are identified at the absence/presence of ADF4, respectively. **B**, ADF4 and WRKY largely colocalize with each other at the presence of WRKY29, suggesting that ADF4 and WRKY29 forms a complex at the promoters of targets of WRKY29. **C**, ADF4 can up- and down- regulate the overall promoter affinity of WRKY. Up- and down-regulated promoters with top-15 overall promoter binding and top-15 regulated fold are listed. **D**, WRKY29 (and ADF4) largely targets genes participating immune process. GO pathway enrichment analysis on WRKY29 targeted genes suggests high enrichment of pathways related to plant immunity.

genes by the two methods, which indicates that WRKY29 and ADF4 indeed co-localize on the targeted promoter loci, and generally form a WRKY29-ADF4-DNA complex.

From the perspective of ADF4 functionality, another question is whether ADF4 can generally regulate the promoter binding affinity (as previously proved in Figure 3-4) and regulate the targeting spectrum of WRKY29. Indeed, in the presence of overexpressed ADF4, the number of identified targets by WRKY29 was largely expanded from 415 to 3704, compared with the condition without ADF4. At the same time, for those promoters significantly detected by both +WRKY29/-ADF4 and +WRKY29/+ADF4 group, ADF4 was capable of regulating the promoter binding affinity by WRKY29 onto the promoter loci (see Figure 3-8C). Among the 371 promoters targeted by both ADF4 and WRKY29 (present in both -ADF and +ADF), 328 promoters got up-regulated affinity, while 43 promoters got down-regulated. The top-15 enriched genes and the top-15 regulated genes were listed aside, many of which were reported to be involved in plant immunity. While such data cannot be directly interpreted as a change of transcription level of these genes, they do suggest that ADF4 has the potential to influence the transcription as a result of the regulated WRKY-DNA affinity.

Last, in order to learn which biological processes are potentially influenced by the targeted genes of the WRKY29-ADF4 complex, I conducted a biological pathway enrichment assay. The 385 genes targeted by WRKY29 on both the presence and absence of ADF4 were input for gene ontology (GO) enrichment analysis. Interestingly yet as expected, almost all aspects of immune processes – covering immune response against both bacterial and fungal pathogen, resistance against wounds, and programmed cell death – are enriched within the WRKY29-targeted genes. Such result fully conforms with the general features of WRKY proteins as the stress-responsive, immune regulator. In summary, the study above identified the target genes of WRKY29 in

Arabidopsis genome, and further demonstrated that ADF4 can enhance the promoter affinity and expand the targeting spectrum of WRKY29 by forming a co-regulatory complex.

Inspection of the ADF interaction interface

One of most important questions is how ADFs with strong affinity to WRKYs mediate this interaction, from the perspective of its protein structure. It was revealed by the aforementioned studies (Figure 3-3 and 3-5) that only ADF2, 3, and 4 can strongly interact with WRKY29/48 among all ADFs expressed in the leaf, while ADF1 and ADF5 are weak and non-interactor, respectively. Such conclusion is refreshingly interesting, because among all 11 ADF isoforms of Arabidopsis, ADF1 has the closest phylogenic relationship with ADF4 but dramatically different WRKY-interaction features. Therefore, inspection on the sequential difference between ADF1 and ADF4 can be a critical strategy to identify the interaction interface on ADF. From a different perspective, it was previously reported that immune signals can trigger the phosphorylation on ADF4 by CPK3, a mechanism to regulate its functionality (Lu et al., 2020); meanwhile, certain phosphomimic variants of ADF4 can rescue the dampened ETI against AvrPphB (Porter et al., 2012). Therefore, it is highly possible that phosphorylation(s) triggered by immune signal occur(s) on the residues of ADF-WRKY interface, which serves as an alternative strategy to inspect the ADF-WRKY interaction mechanism.

Following the first strategy, I compared the protein sequence of ADF1 versus ADF4, as shown in Figure 3-9A. As suggested by their phylogenic relationship, ADF1 and ADF4 have almost identical sequences, with a subtle difference of only eight residues, among which only three residues have strong difference of chemical properties. Therefore, I generated 3 mutants of ADF4 referring to ADF1, $ADF4^{48\text{-}51QPIQ}$ (abbr. QPIQ), $ADF4^{S59C}$, and their combination $ADF4^{48\text{-}51QPIQ/S59C}$ (abbr. QPIQ/S59C), and conducted a semi-quantitative BiFC experiment with WRKY29. Unexpectedly, although both S59S and QPIQ/S59C display a significantly decreased interaction intensity with

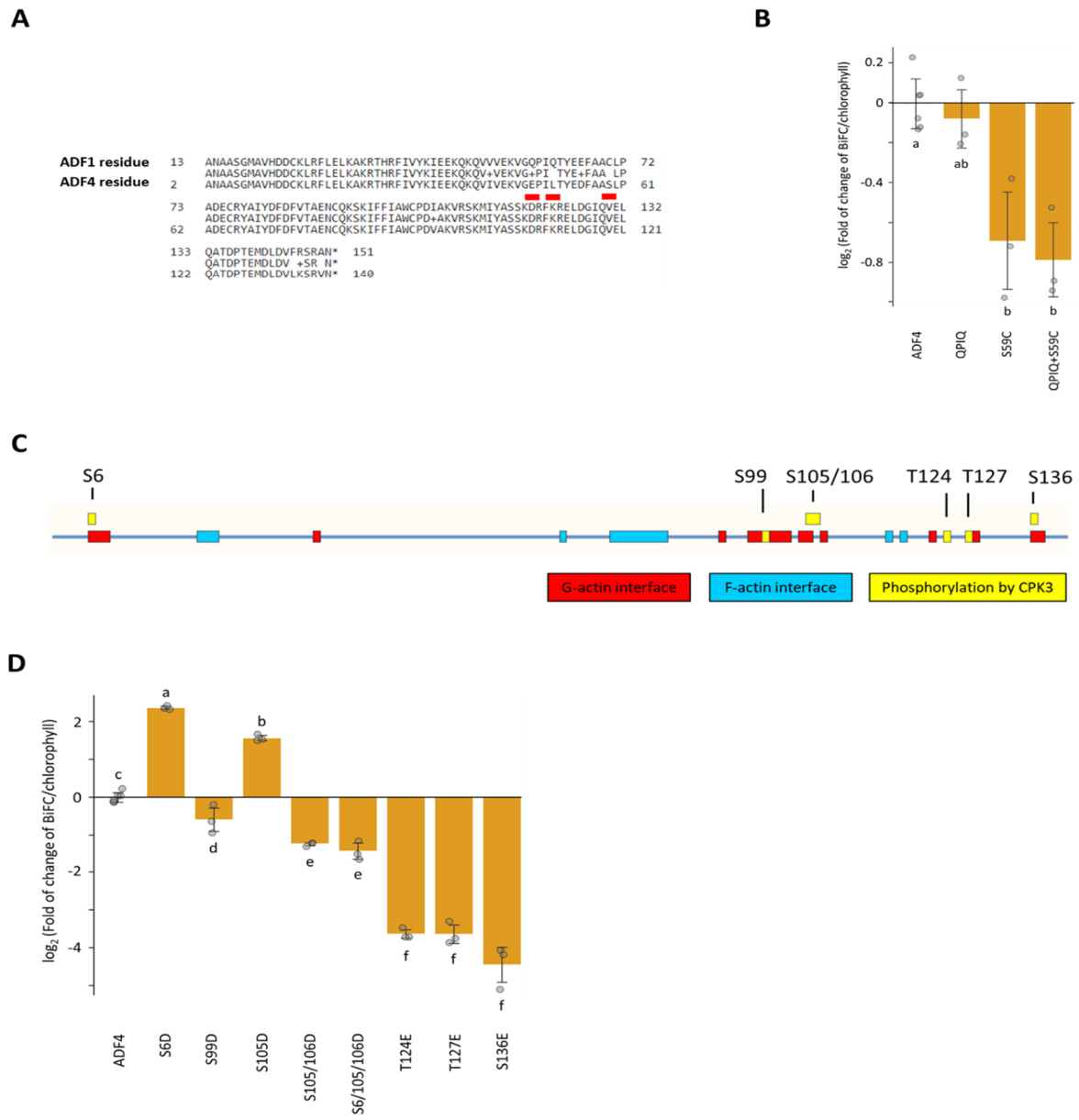

Figure 3-9: inspection on potential mechanism of ADF-WRKY interaction. A, protein sequence alignment of ADF4 vs ADF1. ADF4 and ADF1 have very few difference but dramatically different affinity to WRKY29. Red color marks 3 residues of major difference in chemical property, as hypothetic ADF-WRKY interface. **B**, BiFC interaction intensity of mutants on these residues with WRKY29. The minor decrease of interaction infinity cannot explain the contrast difference between ADF4 and ADF1. **C**, ADF4 phosphorylation by CPK3 in vitro. The G- and F-actin interface is deduced by aligning with published crystal model of cofilin-actin complex. Some of the phosphorylation occur on the ADF-ACT interface, potentially inhibit this interaction. **D**, BiFC interaction intensity of ADF4 phosphomimic mutants with WRKY29. Both up- and down- regulation of interaction by phosphorylation on various residues are detected. Non-overlapped alphabet indicates significant difference defined as ANOVA of $p<0.001$ followed by t-test with Benjamini-Hochberg correction of $p<0.05$. Error bar means standard deviation.

WRKY29 (approximately 1.5-fold down-regulation), it was still a strong interaction compared to the intensity ADF1 (approximately 16 fold lower, Figure 3-3B). Therefore, these three residues are not critical to the difference between ADF1 and ADF4; a valid explanation should be proposed from a different perspective.

As for the second strategy, I inspected the unpublished data generated by the former lab member Dr. Yi-Ju Lu, which described the *in-vitro* ADF4 phosphorylation sites by CPK3, identified by mass spectrometer (MS). As illustrated in Figure 3-9C, seven residues were selected according to the data, namely S6, S99, S105, S106, T124, T127, and S136. Single and multiple phosphomimic mutants (S/T to D/E) of these residues were made and cloned into BiFC vectors with nEYFP fusion, to be co-transformed with cY-WRKY29. As suggested by Figure 3-9D, two phosphomimic mutants, S6D and S105D had increased interaction intensity with WRKY29 by 4-fold and 3-fold, respectively, while other mutants got significantly down-regulated interaction. Particularly, three phosphomimic mutants at the C terminal of ADF4, T124E, T127E, and S136E, rendered intense down-regulation of this interaction to a level of weak WRKY interactor like ADF1. These results suggested that these five residues are critical for mediating the interaction with WRKY29, potentially acting as phosphoregulatory sites by immune-regulated kinases, such as CPK3. Interestingly, the introduction of S106D overshadowed the up-regulatory impact by S6 and S105, which suggests that the phosphor-regulation mechanism is relatively complex and requires a finer methodology to examine. In addition, because the *in-planta* phosphorylation sites of ADF4 by CPK3 are unknown and ADF4 may also be regulated by other kinases, anticipating the influence of phosphorylation on the WRKY-regulatory function by these data is not decently rigorous. To further explore the phosphor-regulation on the functionality of ADF4, an IP-MS experiment to determine all the phosphorylation sites of ADF4 has been under preparation and optimization, with details described in *Appendix B*.

Discussion

In *Chapter 3*, my research focused on the discovery of ADF-WRKY interaction in Arabidopsis, and the identification of its property and mechanism. By screening WRKY and ADF candidates of different phylogenic clades, I identified ADF2, ADF3, ADF4 in the ADF/cofilin family, as well as WRKY22, WRKY29, and WRKY48 in the WRKY family, as participants that mediate a strong interaction, which occurs in the nucleus and leads to the formation of WRKY-ADF-DNA complex on the WRKY-targeted promoter. Through this physical interaction, strong interactors of ADF enhance the transcriptional activation capability of bound WRKYs and simultaneously stabilize them. As a result, the promoter affinity and targeting spectrum of corresponding WRKYs are regulated to a pro-immune status, thereby enhancing the resistance against pathogens. Furthermore, this process is potentially regulated by the phosphorylation triggered by immune signal, such as those mediated by CPK3 (Lu et al., 2020), which can both up- and down-regulate the ADF-WRKY interaction intensity.

From the perspective of the overall functionality of the actin cytoskeleton in plant immunity, the study herein identified the moonlighting function of ADFs in the nucleus, which supports a novel comprehensive model describing the nuclear-cytoplasmic role of ADFs as a multi-layer regulator of immune responses (see Figure 3-10). In the cytoplasm, the known function of ADF is to catalyze actin depolymerization – as suggested by its name – to facilitate actin remodeling (reorganization) against pathogen threat. In this process, the activity of ADFs is dynamically regulated by phosphorylation to enable accurate and flexible regulation of actin architecture (Li and Day, 2019). At the same time, as early immune signal triggers the expression of WRKYs, ADFs (e.g., ADF2/3/4) in the nucleus stabilize these WRKYs (e.g., WRKY22/29/48) and facilitate their full functionality to secure a robust pro-immune transcriptional reprogramming. Importantly, phosphorylation can act as a dual switch to systemically tune up the immunity, by inhibiting ADF-

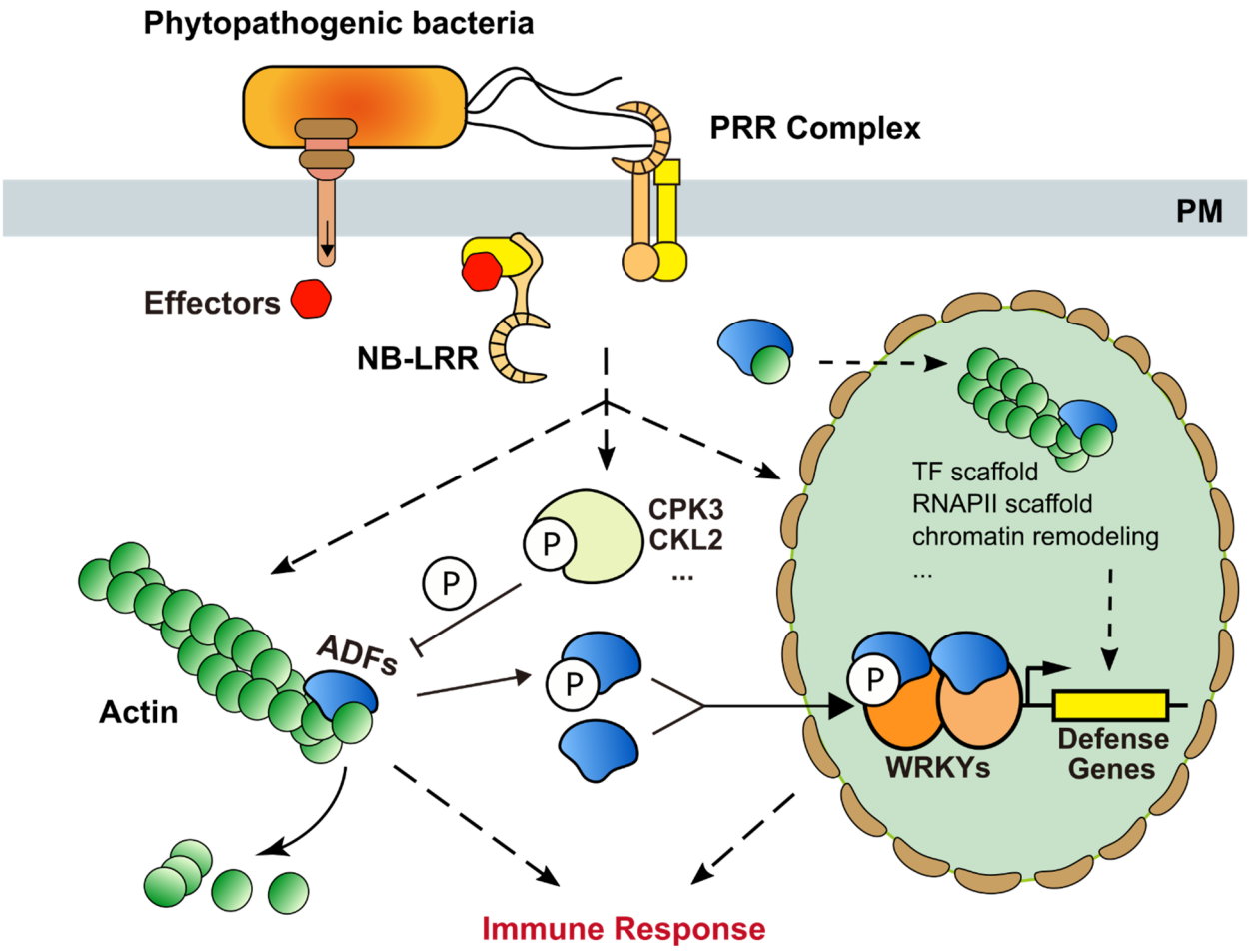

Figure 3-10: a schematic diagram describing the nuclear-cytoplasmic function of ADF4 in immune regulation. Upon recognition of pathogen (PAMPs and/or avirulent effectors), plant triggers immune signaling to initiate actin remodeling to aid downstream immune response, during which one of the critical steps is to activate CPK3 to phosphor-regulate ADFs at high dynamic level. At the same time, ADFs in the nucleus binds to the WRKY TFs induced by immune signal to enhancing their stability and regulate their activity as well as targeting spectrum. The phosphorylated ADF4 by CPK3 and other kinases, released from actin cytoskeleton, have higher affinity to WRKY, which further enhance the pro-immune transcription mediated by ADF-WRKY complex. Besides, ADF can facilitate actin to enter the nucleus (identified in animal system), where actin serve as a transcriptional regulator in many aspects. In the entire process, ADFs participate and secure the robust immunity by the synergistic collaboration of their cytoplasmic and nuclear functions.

ACT interaction and enhancing ADF-WRKY interaction simultaneously. For example, the study described in Figure 3-9 suggests that S6P phosphorylation enhances the ADF4-WRKY29 interaction by 4-fold. Since S6 exactly locates on the ACT-ADF interface, S6P phosphorylation inhibits the intensity of this interaction following immune activation. Thus, with a finite quantity of

ADF4, it is deducible that the overall impact of S6P phosphorylation is to push ADF4 to incline toward the nuclear activity, or a pro-immune phase. This model represents a comprehensive nuclear-cytoplasmic co-regulatory network mediated by the actin cytoskeleton.

There are still two questions that remain to be answered. First, where is the structural interface on ADFs to mediate the interaction with WRKYs and how is it regulated by phosphorylation? The previous attempt to directly solve the problem by testing the mutations of hypothetically critical amino acids failed to prove the importance of these residues, which suggests the study omitted critical residues for this interaction. As an alternative strategy, I will construct chimera proteins of ADF4 and ADF1 (or ADF5) to screen the total protein sequence by BiFC, and gradually locates the critical residues that contribute to the strong interaction between ADF4 and WRKY29. At the same time, I will determine the phosphorylation sites that add to ADF4 in cytoplasm and nucleus, respectively, by IP-MS approach using Arabidopsis transgenic lines expressing ADF4-BFP-FLAG-NES/NLS with PAMP treatment (see *Appendix A*). This study will further confirm the existence of phosphor-regulation on ADF4 and serves to reveal its impact by direct evidence. Second, because all of ADF2/3/4 can boost the activity of WRKY29 while having high expression in Arabidopsis leaves, ADF2/3/4 potentially have redundant functions that overshadow any immune phenotype in ADF single mutants, a hindrance to exploring genetic evidence supporting the nuclear function of ADFs. Therefore, I have been preparing the high-order mutant of ADFs by the CRISPR-Cas9 system, which will be accomplished in the near future (see *Appendix A*).

Last but not least, I wish to discuss the application range of the mechanism model of ADF-WRKY interaction. As the research herein used a strategy of case study (i.e., focusing on the inspection into representative members of ADF and WRKY family as examples to deduce the general properties of their interaction), there was no evidence indicating that this is the only pattern of ADF-WRKY interaction that participates in plant immunity. Instead, other WRKYs that are not

involved in the molecular study but actually highly up-regulated upon the immune signaling, such as WRKY15/30/53, may also play critical roles via interaction with uncertain ADF(s). Similarly, the different WRKY may have other preferences on ADF variants, a perspective that is not covered in depth either.

However, the value of exploring a single case of ADF-WRKY interaction in Arabidopsis lies largely beyond the elucidation of the function of this interaction *per se*. From an expanded horizon, this study discovered brand-new possibilities that indeed refreshed our knowledge on actin cytoskeleton and its associated proteins. First, apart from the ADF-WRKY interaction, ADFs may "moonlighting" as direct TF-regulators at a large scale beyond the WRKY family. In the case of ADF4, the ChIP-seq of ADF4 targeted DNA fraction without co-expression of WRKY actually has revealed 30 promoters (Figure 3-8A), including those of TFs in MYB, bHLH, ERF, and WRKY families. As ADF *per se* does not have any DNA-binding motif, it is predictable that such targeting spectrum is potentially mediated by interaction with other transcription factors. Like the case of ADF4, another study has demonstrated that ADF1 can also interact with TFs such as REM16 (Yu et al., 2020). These shreds of evidence strongly suggest that members of the ADF family, in general, can participate in direct transcriptional regulation regardless of the type of the TF it potentially interacts with, which can enlighten the community as a new perspective to interpret relevant data and observations. In other words, this mechanism may also apply to animals and other eukaryotes – while they do not have WRKY, they do have ADFs or cofilins.

Second, this study conceptually reveals a general signaling pattern that I name as "cytoskeleton reservoir", where cytoskeleton actually serves as a reservoir of storage of semi-functioning proteins that have additional critical function(s) in places beyond cytoskeleton. Like ADFs, their affinity to cytoskeleton can be regulated by incoming signals followed by a change of the affinity to cytoskeleton, or even the collapse of the cytoskeleton itself, to release these proteins for a

different phase of functionality. From this perspective, many ACPs, as well as actin itself, potentially apply to this model, a topic to be explored and verified in the future.

Methods

Plant Growth

All plants are grown in a BioChambers model FLX-37 walk-in growth chamber (BioChambers, Manitoba, Canada) at 20 °C with 12h light/12 dark with 60% relative humidity and a light intensity of 120 μmol photons $m^{-2} s^{-1}$.

Construction of vectors

The studies herein utilized the Gateway™ system, where specific interested genes (such as ADFs and WRKYs) were amplified from Col-0 cDNA, and first cloned into an "entry vector" pENTR™/D-TOPO™ (Thermo #K240020), following the commercial documentation. The obtained pENTR::gene-of-interest can be transferred to any functional "destination vector", by LR clonase (Thermo #12538120) following the same standardized approach in the documentation. If the destination vector is also Kan^r, it will be first linearized by MluI digestion and purified before recombination by LR clonase.

For protoplast BiFC, Gateway-compatible destination vector pM1089 (for -nEYFP) and pH1097 (for -cEYFP) were designed and constructed in this research. To test the BiFC system, vector CD3-1089 and CD3-1097 (purchase from TAIR) was investigated in the beginning, but two major issue were found: (1) CD3-1089 have very low copy number due to mutations on the origin of replication, and (2) both do not have high-specific immune tags. Therefore, we constructed the pH1097 and pM1089 using the edited backbones of different sources, together with other newly

A

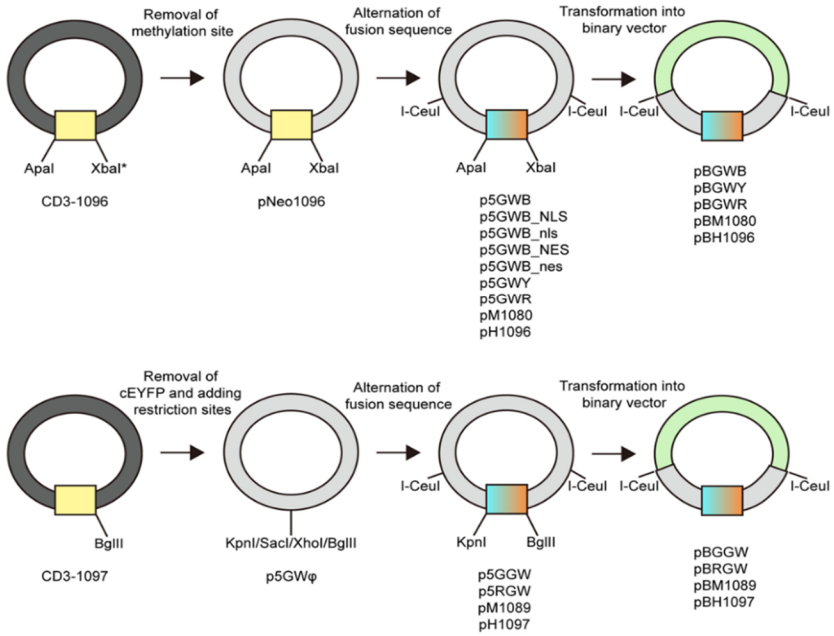

B

Name	Use	bacteria resistance	Plant resistance	structure	Other information
pNeo1096	protoplast	Amp		2X35S-GW-cEYFP-35S terminator	Tested high-copy
p5GWB	protoplast	Amp		2X35S-GW-mTagBFP-Flag-35S terminator	Tested high-copy
p5GWB_NLS	protoplast	Amp		2X35S-GW-mTagBFP-Flag-NLS-35S terminator	Tested high-copy
p5GWB_nls	protoplast	Amp		2X35S-GW-mTagBFP-Flag-nls-35S terminator	Tested high-copy
p5GWB_NES	protoplast	Amp		2X35S-GW-mTagBFP-Flag-NES-35S terminator	Tested high-copy
p5GWB_nes	protoplast	Amp		2X35S-GW-mTagBFP-Flag-nes-35S terminator	Tested high-copy
p5GWY	protoplast	Amp		2X35S-GW-sYFP2-Myc-35S terminator	Tested high-copy
p5GWR	protoplast	Amp		2X35S-GW-mCherry-Ha-35S terminator	Tested high-copy
pM1080	protoplast	Amp		2X35S-GW-Myc-nEYFP-35S terminator	Tested high-copy
pH1096	protoplast	Amp		2X35S-GW-HA-cEYFP-35S terminator	Tested high-copy
pBGWB	Agrobacteria	Spec	Basta	2X35S-GW-mTagBFP-Flag-35S terminator	
pBGWB_NLS	Agrobacteria	Spec	Basta	2X35S-GW-mTagBFP-Flag-NLS-35S terminator	
pBGWB_nls	Agrobacteria	Spec	Basta	2X35S-GW-mTagBFP-Flag-nls-35S terminator	
pBGWB_NES	Agrobacteria	Spec	Basta	2X35S-GW-mTagBFP-Flag-NES-35S terminator	
pBGWB_nes	Agrobacteria	Spec	Basta	2X35S-GW-mTagBFP-Flag-nes-35S terminator	
pBGWY	Agrobacteria	Spec	Basta	2X35S-GW-sYFP2-Myc-35S terminator	
pBGWR	Agrobacteria	Spec	Basta	2X35S-GW-mCherry-Ha-35S terminator	
pBM1080	Agrobacteria	Spec	Basta	2X35S-GW-Myc-nEYFP-35S terminator	
pBH1096	Agrobacteria	Spec	Basta	2X35S-GW-HA-cEYFP-35S terminator	
pBGWϕ	protoplast	Amp		2X35S-GW-35S terminator	
p5GGW	protoplast	Amp		2X35S-Myc-mEGFP-GW-35S terminator	
p5RGW	protoplast	Amp		2X35S-HA-mcherry-GW-35S terminator	
pM1089	protoplast	Amp		2X35S-Myc-nEYFP-GW-35S terminator	Tested high-copy
pH1097	protoplast	Amp		2X35S-cEYFP-HA-GW-35S terminator	Tested high-copy
pBGGW	Agrobacteria	Spec	Basta	2X35S-Myc-mEGFP-GW-35S terminator	
pBRGW	Agrobacteria	Spec	Basta	2X35S-HA-mcherry-GW-35S terminator	
pBM1089	Agrobacteria	Spec	Basta	2X35S-Myc-nEYFP-GW-35S terminator	
pBM1097	Agrobacteria	Spec	Basta	2X35S-cEYFP-HA-GW-35S terminator	

Figure 3-11: Construction of Gateway vectors for multiple purpose. A, the schematic diagram showing the process of construction of the Gateway vectors. From the protoplast vector CD3-1096, a methylation site on a XbaI site necessary for the reconstruction is removed by PCR of the total plasmid to obtain pNeo1096, followed by replacing the cYFP between the ApaI and XbaI site to other sequences. For some of generated protoplast vectors, the functional sequence between the two I-CeuI sites is transferred to pPZP-RCS2-bar (TAIR, #CD3-1057), to generate corresponding binary vectors for Agrobacteria-mediated transformation. A similar strategy is used on CD3-1097 for other objective vectors. **B**, the table describing the information of each generated vector. The ones highlighted by green colors were used in this study.

constructed plasmids for difference functions, with some adapted in this study. The total process is described in Figure 3-11.

In addition, pBGWB and pBGWY were used for subcellular co-localization assay; p5GWH and p5GWM were used for the protein stabilization assay and ChIP; pBGWφ, p5GWB, p5GWB-NLS, p5GWB-NES, and p5GWR were used for the promoter reporter assay. Please refer to these sections for specific usage of these vectors.

DNA point-mutation

The construction of mutants is conducted by fusion PCR, i.e., generating two pieces of PCR product with overlapping sequence (with objective mutation) at the downstream of upstream of the products, respectively, and conduct a second PCR using the previous product as template. The primers used for mutagenesis in this study are listed in the *Appendix B*.

Agrobacteria-mediated transformation

Agrobacterium tumefaciens GV3101 (Rif^r/Gen^r) was used in this study. Target genes in the binary vector are transformed into the Agrobacteria by electroporation. 2-day-old Agrobacterial grown on a LB plate with proper antibiotics are used for plant transformation.

For Agro-infiltration, the Agrobacteria lawn on a plate is diluted to O.D. = 0.6 (single transformation) or each of 0.4 (co-transformation) by Agro-infiltration buffer (10 mM MES [pH 5.6], 10 mM $MgCl_2$, 150 mM acetosyringone). After incubation in darkness for 2 hours, the Agrobacteria solution is inoculated to *N. Benthamiana* leaves by hand-infiltration, and the plant is transferred back to growth environment. 48hpi plants are used for downstream experiments.

For Arabidopsis floral-dip, Agrobacteria are inoculated into 10mL LB media with proper antibiotics overnight. After centrifuge, the bacteria are re-suspended in 2mL of the floral-dip buffer (1/2 MS, 5% sucrose, and 0.02% Silwet L-77). Each flower to be transformed is dipped up-and-down for 10s. The plants with dipped flower are shaded in full darkness with saturated humidity for 24 and restore to growth condition for harvest.

Protoplast transformation

Arabidopsis protoplasts are transformed using a modified method referring to Yoo et al., 2007 and Wu et al., 2009. In brief, leaf #8,9,10 of 5-week-old Arabidopsis are cut off, and the lower epidermis are removed by tapes. The leaves are merged in the Enzyme Solution for 1.5h with slight touch-shake per 20min. The obtained protoplast were washed by the W5 solution finally resuspended by MMG solution at $5x10^5$ protoplast/mL. For a standard procedure, each sample of 200 μL protoplast in MMG is gently mixed with less than 20μL of vector and 220 μL of PEG solution and kept in darkness for 5min. 920μL of W5 is added immediately to stop transformation. The transformed sample is washed once by W5, and finally re-suspended in 1mL W5 solution and kept under weak light (~200 lux) for 12h before downstream experiment. The formula of the solutions involved is exactly identical to those in [].

Confocal microscopy

Olympus FV1000D is used for BiFC, with 515nm excitation, BA535-565 emission filter for YFP signal, and BA650IF for chlorophyll, through Olympus UPLFLN 10X Objective (quantitative analysis) or 65x/1.42 PlanApo N Objective (portrait of detail). Nikon A1Rsi is used for promoter assay, with sequential scanning of (1) 405nm excitation/425-510nm detection for BFP (mTagBFP), with 560nm excitation/580-640nm detection for RFP (mCherry), and (2) 488nm excitation/xxx for GFP and xxx for chlorophyll, through Plan Apo λ 10X objective lens.

Semi-quantitative BiFC

Protoplast samples are transformed with 3.5μg pM1089::ADF and 7μg pH1089::WRKY vector. After 12h, images containing both BiFC fluorescence and chlorophyll channels are collected by confocal microscopy, with low magnification (10X) and large pinhole (~600nm) to include large quantities of entire cells. The laser power and the sensitivity of the photon sensor is set to barely detect saturated pixels in the brightest sample, to obtain the most accurate and comparable results. The data of pixel brightness of the captured image is used to calculate the ratio of the sum of BiFC (YFP) signal to the sum of chlorophyll signal (serving to normalize BiFC signal by the quantity of live cells), above a background threshold. The background threshold is determined by the average of the values below which covers 95% of the pixels, of the mock samples.

Promoter reporter assay

Protoplast samples are transformed with 6μg pBGWφ::pW29/pBAG7/pW46/pW48 (GFP driven by WRKY induced promoter), together w/o 3μg p5GWR::WRKY (WRKY-RFP) and/or 7μg p5GWB::ADF (ADF4-BFP). The confocal images are captured using the same approach as semi-quantitative BiFC, but four channels – BFP, GFP, RFP, and chlorophyll – are collected. Like semi-quantitative BiFC, GFP/chlorophyll (above background threshold) is calculated for the general comparison of ADF-WRKY regulated promoter intensity.

For the mathematical model of WRKY enhancement coefficient (EC), the corresponding background threshold is first subtracted from each channel, and the total fluorescence of each channel is calculated as:

$$B_i = \sum\left(B_{pix} - Thres_B\right) \mid pix \in \{pix \mid B_{pix} > Thres_B\} \quad ,$$

$$G_i = \sum\left(G_{pix} - Thres_G\right) \mid pix \in \{pix \mid G_{pix} > Thres_G\} \quad ,$$

$$R_i = \sum\left(R_{pix} - Thres_R\right) \mid pix \in \{pix \mid R_{pix} > Thres_R\} \quad ,$$

$$Chl_i = \sum\left(Chl_{pix} - Thres_{Chl}\right) \mid pix \in \{pix \mid Chl_{pix} > Thres_{Chl}\} \quad ,$$

where *i* represents each image and *pix* represents each pixel. The GFP brightness normalized by chlorophyll (*Chl*) is calculated as:

$$[G]_i = \frac{G_i}{Chl_i} \quad .$$

Therefore, the basic (untriggered) transcription level of pW29, as a constant, can be estimated as:

$$[G]_{untriggered} = Mean\left([G]_i \mid i \in \{-WRKY, -ADF\}\right) \quad .$$

Next, to evaluate how many folds of regulation on GFP occur due to the introduction of WRKY29 w/o ADF, the regulation level is defined by the ratio of gained GFP brightness to estimated basic GFP level without ADF/WRKY:

$$Reg_i = \frac{G_i}{[G]_{untriggered} * Chl_i} \quad .$$

Then, the upregulation level contributed by per unit of WRKY of each group can be deduced as:

$$RPW_i = (Reg_i - 1)/R_i \quad ,$$

which includes the impact of ADF, if present in the group. In order to further dissect the up-regulation of WRKY activity contributed by ADF, the basic RPW, contributed by WRKY without ADF, as a constant, is estimated by the data of +WRKY/-ADF group, as:

$$RPW_{-ADF} = Mean\left(RPW_i \mid i \in \{+WRKY, -ADF\}\right)$$

Next, to evaluate how many folds of change of RPW is made by the introduced the ADF of each group, the fold of enhancement per unit of WRKY, or EPW, is calculated as:

$$EPW_i = RPW_i / RPW_{-ADF} \quad .$$

Finally, the index to measure the power of WRKY enhancement normalized by per unit of ADF is named as WRKY regulatory coefficient (EC), which is defined as:

$$EC_i = (EPW_i - 1)/B \quad ,$$

which reflect a nature of ADF as WRKY regulator regardless of the quantity in the system.

ChIP-qPCR

600μL protoplast in MMG solution are transformed with 15μg p5GWM::WRKY, w/o 30μg p5GWH::ADF, following the method described in the section *Protoplast transformation*. For flg22 treatment, flg22 at final concentration of 1μM is added to the sample 1 hour before harvest. After 12h incubation under weak light, the samples are crosslinked and the nucleus fractions are purified, sonicated, homogenized for IP, using Pierce™ Classic Magnetic IP/Co-IP Kit (Thermo # 88804) following the official instruction. Particularly, the sonication is conducted by Branson CPX5800 ultrasonic for a total 30min. After overnight IP followed by DNA de-crosslink, the pulled-down DNA fraction as well as input samples is collected by Zymoclean Gel DNA Recovery Kit (Zymo Research, #4008). 45μL elution buffer (without EDTA) is used to solve the DNA for ChIP-qPCR. For each run, 2 μL of eluted DNA is used as template with 3 technical repeats. The primers to detect WRKY-targeted DNA are listed *in Appendix B*.

ChIP-seq

The ChIP is conducted following the same method as ChIP-qPCR, but each sample of 600μL protoplast is finally eluted with only 20μL elution buffer. The distribution of fragmented DNA size is inspected by TapeStation system to ensure the majority of the DNA is between 200-400bp. Then, the library is prepared by Takara ThruPLEX DNA-Seq Kit (Takara, #R400674) and inspected by TapeStation again for quality control. 75bp paired end sequencing is conducted by Illumina NEXTSEQ 500.

The result is inspected to ensure no adapter is detected. BWA is used to align the reads, and results with size >900bp are abandoned. The alignments are filtered to remain only results matching with nuclear genome with quality score greater than 20. Results of 3 biological repeats are pooled together. Finally, the peak-calling of the filtered alignments is conducted by MACS2 with default setting, with band width set to 300, for downstream analysis (specified in figure

legends). Only peaks aligned to promoter region is used. Besides, if a promoter has multiple enriched peaks, the total enrichment fold (TEF) is used to evaluate the level of fraction enrichment, which is defined as $TEF = 2^{\sqrt{\sum(log_2 EF)^2}}$, where EF is the enrichment fold number of each peak. A positive target of WRKY/ADF is generally defined as both log10(p) and log10(q) are greater than 50; for the -WRKY29 /+ADF4 α-HA group, because the total gain of DNA is relatively lower, both thresholds are changed to 20.

Bacterial growth assay

Pseudomonas syringae pv. tomato DC3000 strains are grown on NYGA plates for 2 days for harvest. The bacteria are diluted in 10mM $MgCl_2$ to $O.D._{600}$ = 0.002 (10^6 CFU/mL) to inoculate into Arabidopsis leaves (usually #7,8,9) by hand-infiltration. After the leaf is dried, Arabidopsis plants are kept in a tray with dome, to maintain near-saturation humidity, and returned to growth condition. Samples are harvested 3dpi, with totally 6 leaf disks collected from the 3 leaves from a plant defined as a biological repeat. Totally 8 biological repeats of each group are collected for analysis.

Transcriptional temporal pattern analysis of ACT, ADF, and WRKY

Arabidopsis mRNA-seq dataset GSE85932 and GSE151885 were downloaded, decompressed and uploaded to the Galaxy platform. Each selected .fastq data file is trimmed by Trimmomatic by default setting to eliminate barcode and low-quality reads. Next the reads were quantified by Salmon. The TPM quantifications of each isoform of a gene are summed to render the total TPM of a gene for comparison in form of heatmap. For GSE151885 dataset only, the absolute quantification of all groups is rendered by the reverse-calculation from the 0h group absolute quantification and the relative quantification compared to the 0h group.

Statistics and visualization

All image computation, statistical analysis, and data presentation/visualization are conducted in Python 3.8 environment, using Numpy, Scikit-posthocs, Pandas, Matplotlib, and Seaborn libraries.

APPENDICES

Appendix A: supplemental figures of ILEE

Appendix A describes the supplemental figures (Figure AA-1 to AA-16) describing the design and performance of ILEE algorithm in *Chapter 2*, as listed below:

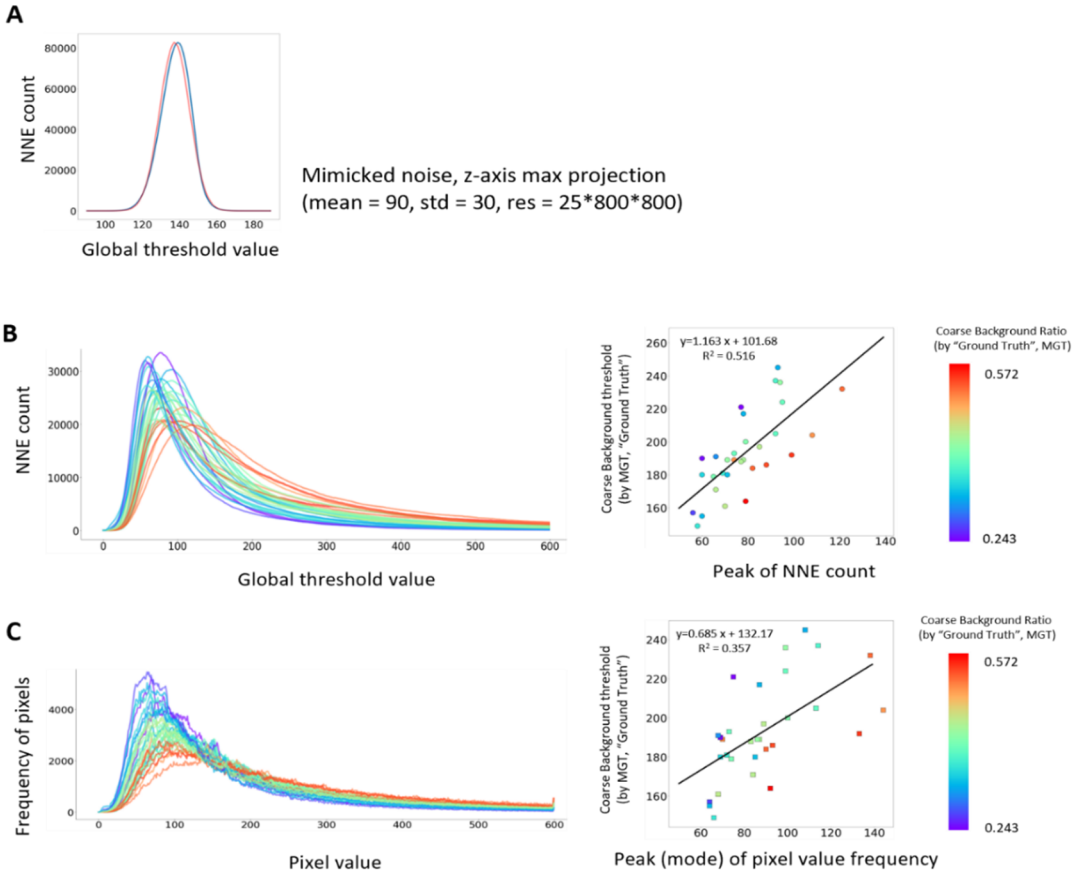

Figure AA-1: NNES (Non-connected negative elements scanning) identification of course ackground. A, NNE count has a normal-like distribution. A confocal microscopy background-noise image was mimicked by random normal distribution (mean = 90, std = 30) into a 25*800*800 array. The maximum projection is conducted by choosing the maximum value of the third axis to make an 800*800 image (distribution shown as blue), and its mean and STD are calculated to make a true normal distribution (shown as red), both of which finely overlap. Therefore, the peak (representing the mean) is a good feature value. **B**, Performance of NNES-based adaptive global thresholding and its prediction. A random set of 31 actin image of 25*800*800 in our database are used to evaluate a coarse background threshold using MGT. Left, the NNES curves reflecting the relationship between global threshold and NNE count; right, correlation of ground truth coarse background evaluated by MGT vs peak of NNE count for individual samples. The color of each sample represents the proportion of coarse background within all pixels. **C**, Performance of brightness based adaptive global thresholding using histogram peak as a feature value. Left, histogram curve of the 31 training samples; right, correlation of the same ground truth coarse background vs peak of histogram (i.e., mathematical mode). Comparing to the histogram-based methods, NNES has a much smoother shape that enables the utilization of peak as a feature value. Also, NNES has a more robust correlation to coarse background determination, as by MGT.

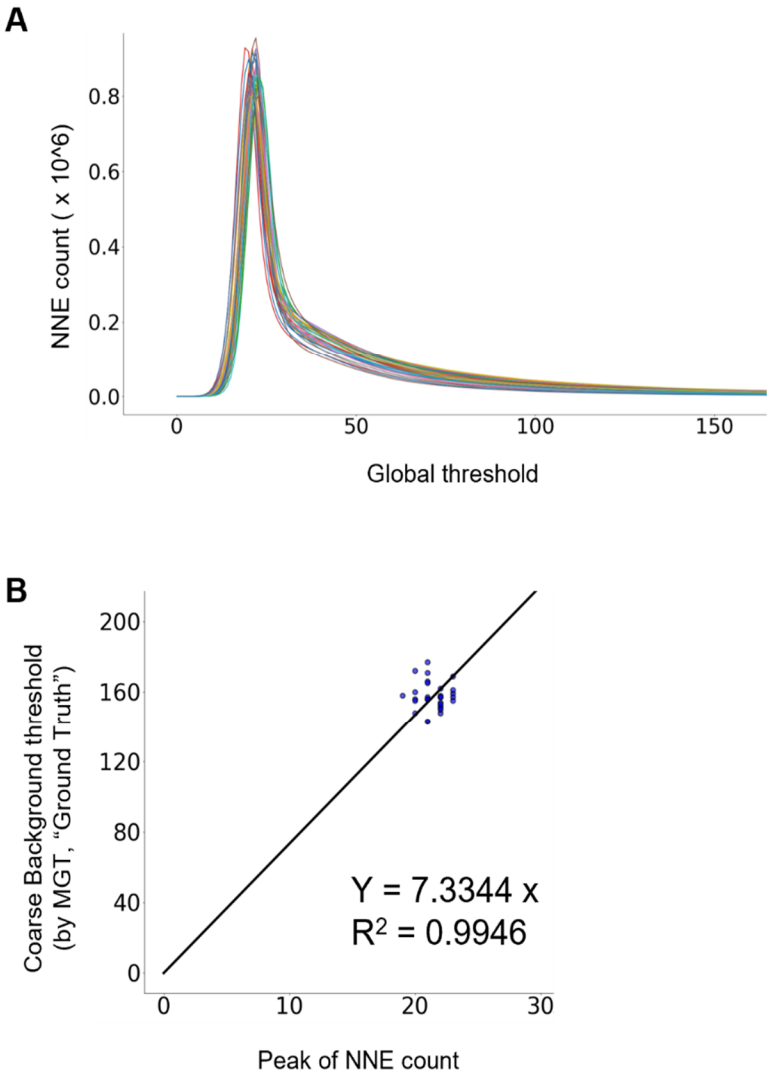

Figure AA-2: Performance of NNES adaptive global thresholding and its prediction model (3D). A, The NNES curve of the same sample set as Figure AA-1. While they varies in actin features (density, bundling, etc.), they have very similar NNES shape. **B,** The correlation of coarse background (evaluated by an approach mimicking 2D MGT) vs the peak of NNE count for individual samples and corresponding coarse background prediction model. As suggested by NNES curve shape, they have very similar peak as well as coarse background, which represents the norm of sensor performance in 3D imaging (2D projection therefore is distorted by information loss). Therefore, we directly used a simple proportional function to establish the regression model.

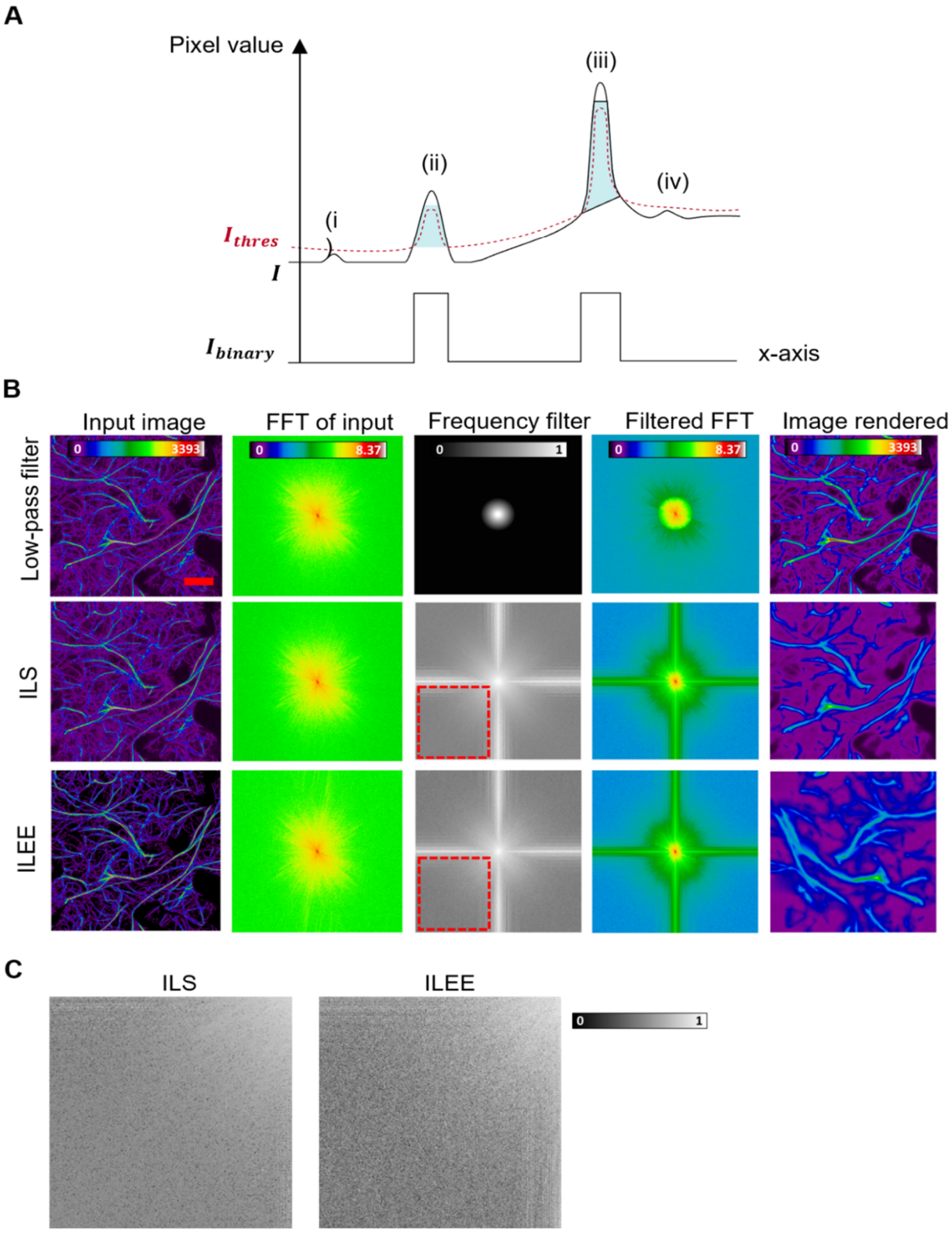

Figure AA-3: Visualized explanation of core ILEE algorithm. The core strategy of ILEE thresholding is explained from the perspective of time domain threshold (marked cyan in A), which…

Figure AA-3 (cont'd) … exclude (i.e., image itself) and frequency domain (i.e., after Fourier transformation, FFT). **A**, Schematic diagram describing how ILEE generates local threshold based on detected edges. For the purposed of simplicity, we use a "1D image" for demonstration. Suppose there is an example grayscale image ($\boldsymbol{I}$) with 4 peaks of pixel value (i, ii, iii, iv); the higher peak ii and iii are true cytoskeleton fluorescence but the lower peaks i and iv are random noise. ILEE first identify edges of cytoskeleton – area with a gradient magnitude higher than a computed threshold. Then these edge are used as "reference values" to generate a threshold image ($\boldsymbol{I_{thres}}$, in red color), that smoothly links all the reference area. Finally, the bona-fide cytoskeleton will be defined as area where $\boldsymbol{I}$ is higher than $\boldsymbol{I_{thres}}$. The areas not selected as edges will not be referred, which means true florescence with locally high values (ii, iii) are selected and background with locally low values (i, iv) are excluded, regardless of whether the local level is generally low (i, ii) or high (iii, iv). **B**, The comparison of effect of ILEE, classic low-pass filter, and implicit Laplacian smoothing (ILS) on image frequency domain. For low-pass filter, the input image (I) transformed into frequency domain pattern by FFT, and we artificially define a filter where 0-1 indicates the passing rate of each frequency fraction. We pass the frequency pattern through the filter to render the filtered FFT pattern, and restore the image by reverse FFT. For ILS and ILEE, the input image (I and Iedge respectively) are transformed to frequency domain pattern by FFT; on the other side, the result of ILS and ILEE are pre-computed and transformed to frequency domain pattern as the "filtered FFT". The (equivalent) frequency filter is deduced by subtracting filtered FFT from FFT of input and make the value relative to the FFT of input, which is comparable to the classic low-pass filter. ILS and ILEE has more fractions low frequency fractions on either x- or y-direction, which are potentially thick line cytoskeleton structures. Scale bar = 20 μm. **C**, Comparison of high-frequency filtering of ILS and ILEE. The red rectangle in subplot **B** is maximized to present the detail. ILEE has uneven but well-directed selection of high frequency fractions because ILEE particularly preserves the cytoskeleton edge and tends to neglect the coarse background.

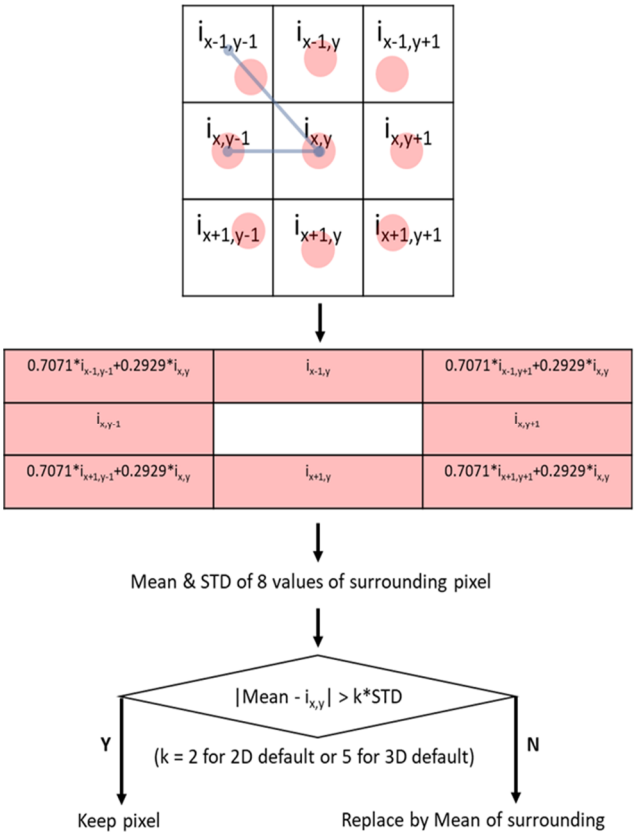

Figure AA-4: Significant difference filter. Significant difference filter changes a pixel to the mean of its surrounding pixel if the object pixel is "significantly different" from its surrounding pixel. "Significant difference" is defined as a difference greater than 2-fold of standard deviation (STD) of surrounding pixels for 2D mode and 5-fold for 3D mode. The rationale behind is that there is no detectable independent actin element as tiny as one pixel element, so a one-pixel region that is significantly different from its surrounding tends to be noise or bias due to z-axis projection.

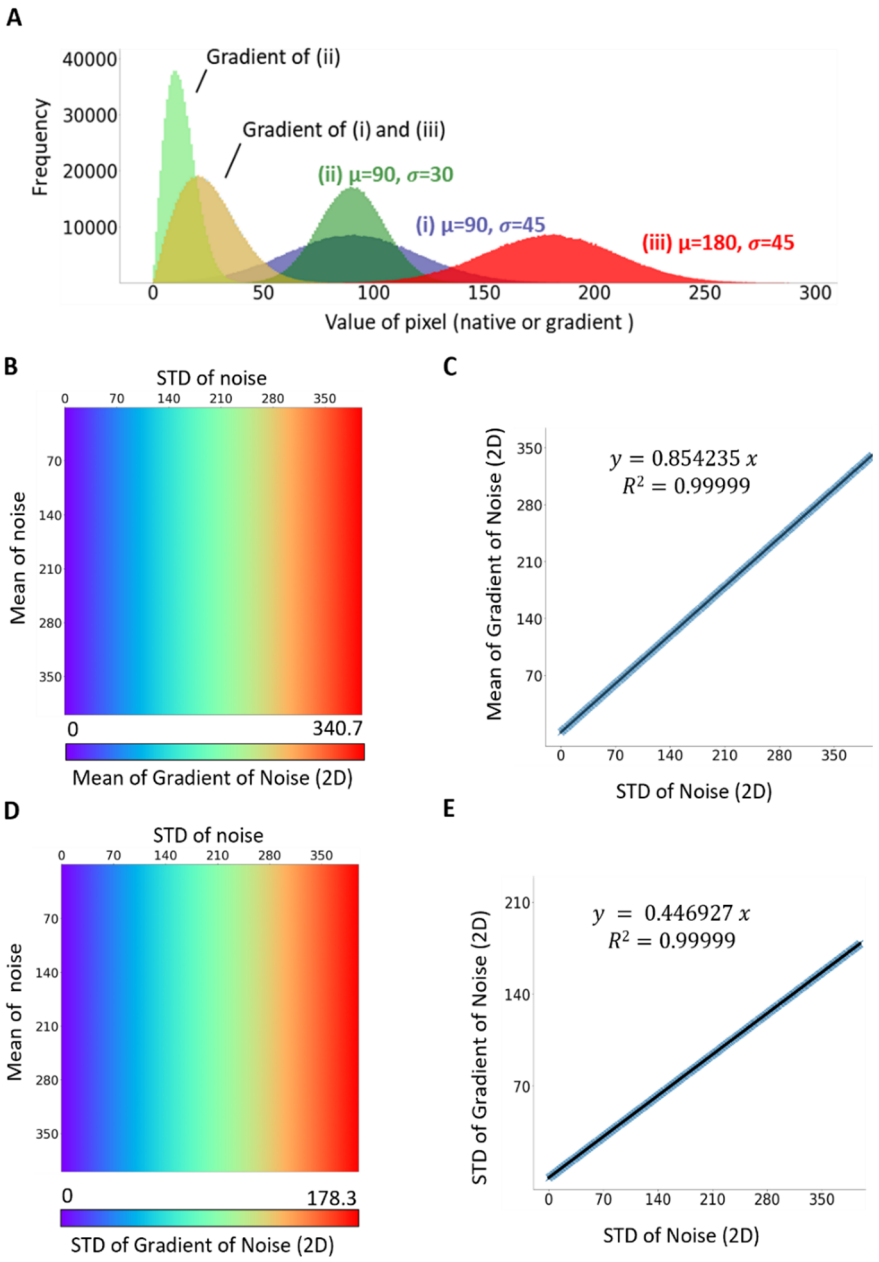

Figure AA-5: The mean and standard deviation (STD) of gradient magnitude of ground noise is directly proportional to the STD of noise. To investigate the mathematical relationship between statistical distribution of ground noise (represented by coarse background located by NNES) and the gradient magnitude of ground noise, we used random normal array that mimics the data structure of our image sample, and generated its Scharr gradient image for statistical analysis. **A,** Normal-like distribution of Scharr gradient**.** Simulated 800*800 ground noise image subject to normal distribution (i), (ii), and (iii) are processed by Scharr operator and the gradient distribution is shown. The gradient distribution is not influenced by the mean yet by the STD of native data of the simulated ground noise. **B** and **C**, The mean of noise gradient is not influenced by the mean of the noise, but the STD of noise. The mean of noise gradient is directly proportional to the STD of native noise. **D** and **E**, The STD of the noise gradient is only influenced by STD of the noise as well. The STD of the noise gradient is directly proportional to the STD of native noise.

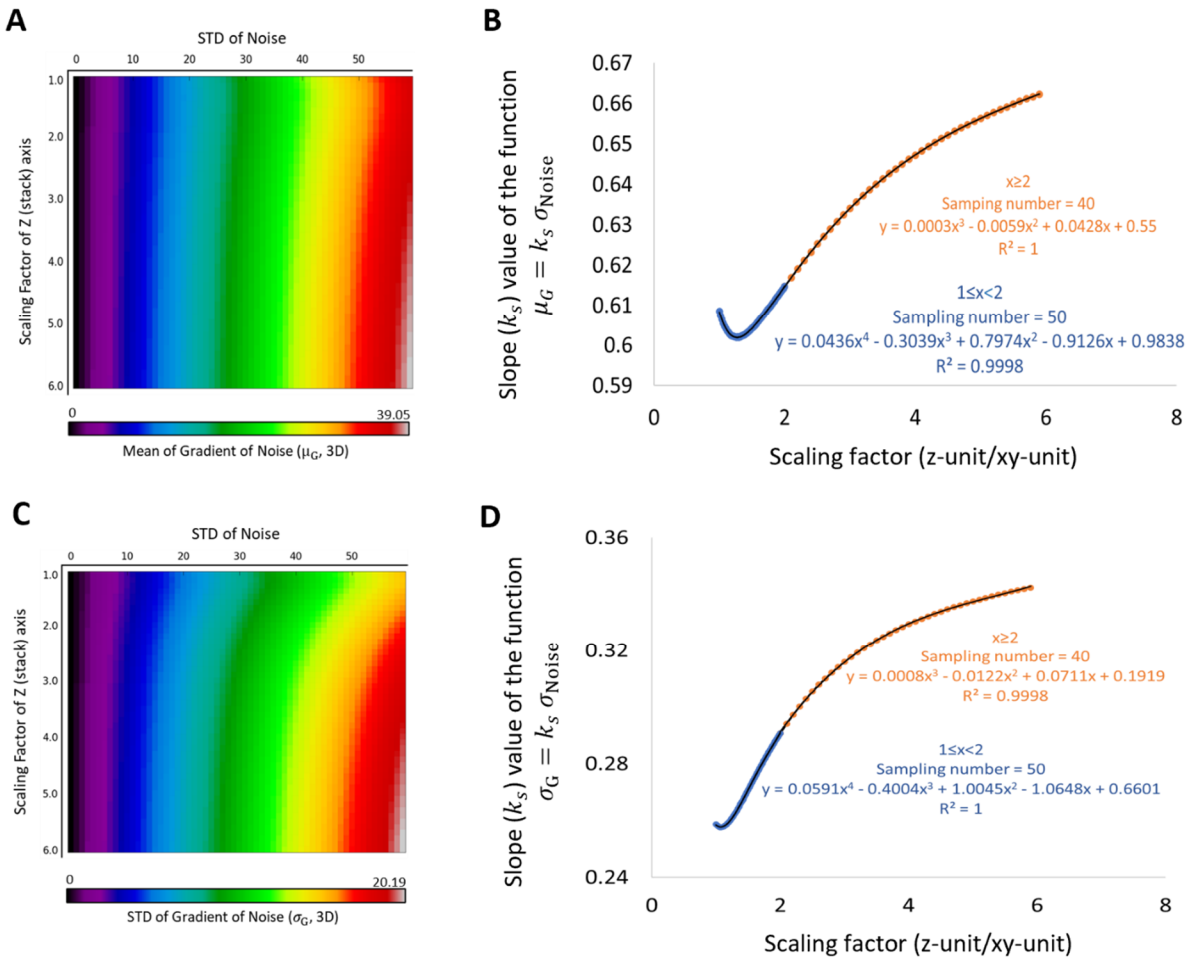

Figure AA-6: The ratio of x-y unit and z unit influences the proportional coefficient of σ_{Noise}-μ_G and σ_{Noise}- σ_G relationship. Using a strategy similar to what is presented in Figure AA-5, we simulated 3D normal ground noise images (800*800*25) with a variable standard deviation (STD) and mean fixed to 90. Next, the z-axis was interpolated by the fold of a scaling factor, defined as z-unit / xy-unit, the second variable. Like the 2D data structure, at a given scaling factor, the mean and STD of noise gradient is proportional only to the STD of native noise. Then, we adopt a mathematical model μ_G or $\sigma_G = k_s(Scaling\ factor)\ \sigma_{Noise}$ to accurately describe the numeric relationship between the gradient and native value of background noise. By a piecewise polynomial regression, we obtain a prediction model that accurately ($R^2 = 1$) calculate k_s and therefore determine the relationship between mean/STD of the noise gradient and the native noise values. **A** and **B**, the relationship between mean of noise gradient and STD of noise. **C** and **D**, the relationship between mean of noise gradient and STD of noise.

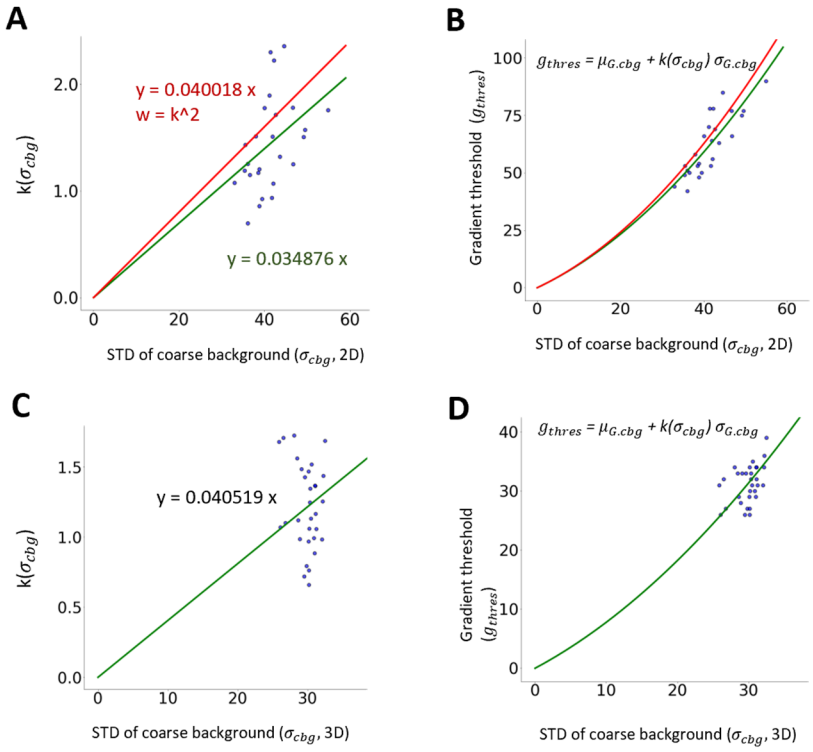

Figure AA-7: Determination of global gradient threshold. In order to determine the global gradient threshold using estimated mean and standard deviation (STD) of coarse background gradient as an input of ILEE, we constructed a non-linear estimation model $g_{thres} = \mu_{G.cbg} + k(\sigma_{cbg})\ \sigma_{G.cbg}$. The global gradient threshold of 30 samples with 800*800*25 resolution randomly collected from our actin image database were evaluated manually (similar to MGT), and the mean and STD of gradient values in coarse background are calculated following the approach described in the *Methods* and Figure AA-5. For the 2D mode, images were first projected to 800*800 resolution. Then, the coefficient k of each sample was calculated and corelated with STD of the coarse background. **A,** The correlation of STD of coarse background and k. Green, standard mode, where each sample have the similar weight of regression; Red, conservative mode (default of this paper), where a weight equal to k^2 is applied. **B,** The g_{thres}-σ_{cbg} relationship restored from a. **C** and **D,** Similar to **a** and **b**, but the reference global gradient threshold were manually evaluated using a 3D visualizing interface.

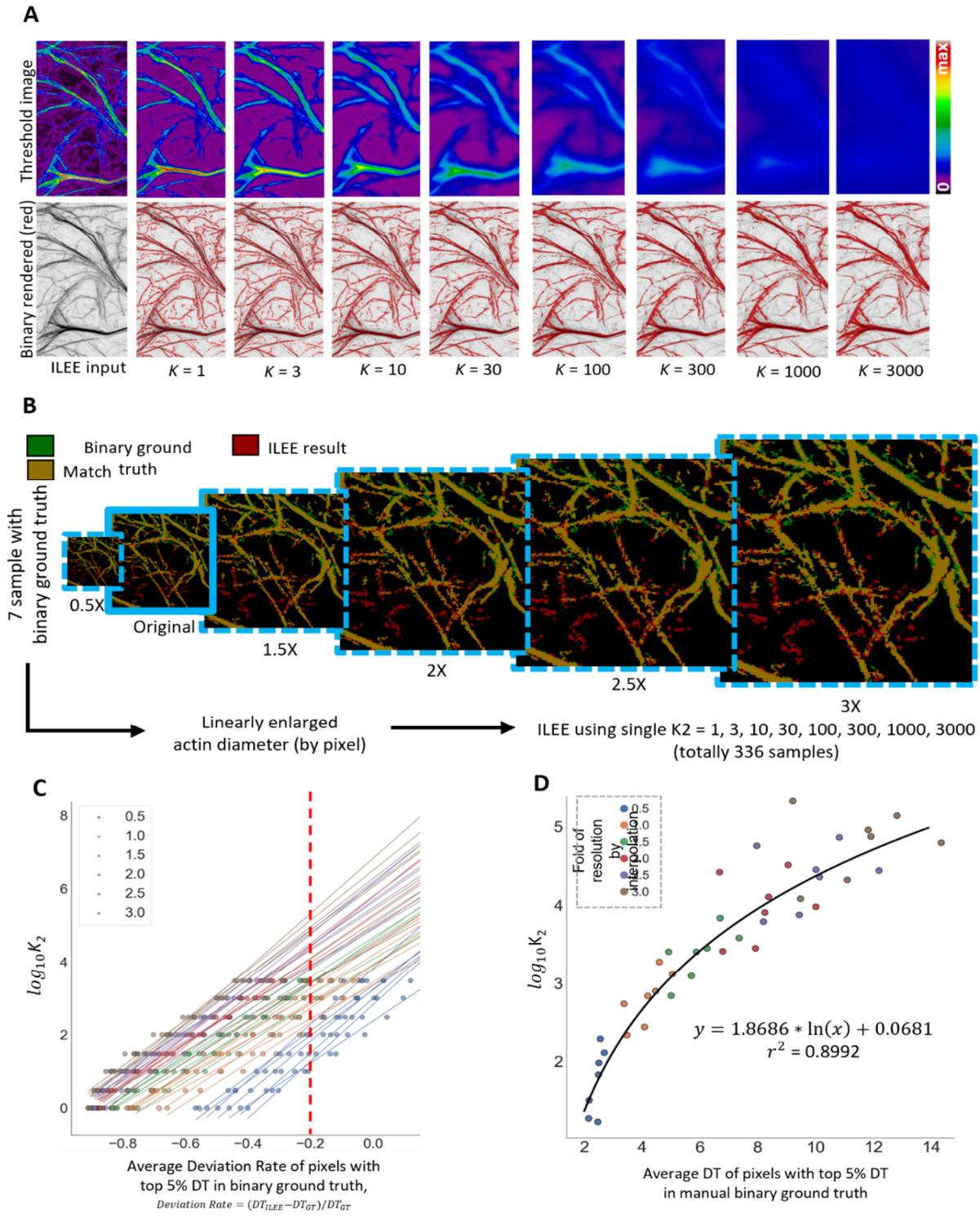

Figure AA-8: The impact of *K* and the training for K_2 estimation. In order to learn the impact *K* (implicit Laplacian smoothing coefficient) and determine the *K* value for a give batch of image sample, we constructed a training database and developed a non-linear estimation model. **A**, The influence of …

Figure AA-8 (cont'd) … different K to rendered threshold image and binary result by ILEE. A low K renders a threshold image that assimilates the object sample with finer filament structure (preserved high frequency information), but tends to underestimate the thickness of bright and thick filament; as K increases, less local detail are preserved, and the rendered binary image losses thin and faint filaments but get more accurate for thick and bright filament. There is a trade-off over the performance over faint/thin and bright/thick for a single K. Therefore, we used the full-outer-join result of a small K_1 and a high K_2 (Fig. 3b and corresponding main text). **B**, Construction of K_2 training database. Initially, we planned using the 7 images with hand-portrayed binary ground truth of filament fraction, but these sample have relatively limited range of filament size by pixel, so we decided to expand out sample pools using these data. Each samples are bicubically interpolated into the resolution of 0.5-, 1,5-, 2-, 2.5-, and 3-fold of the original and added to the database. Their corresponding binary imaged are converted to float data type with 0.0 and 1.0 to process the same bicubic interpolation, with the pixels over 0.42 are defined as True and False if not. Using this approach, the judgement of matching between the ground truth and ILEE result did not have significant change, as shown. Finally, each sample will be processed by ILEE with a single K_2 ranging from 1 to 3000, rendering a total of 336 binary images as the training database. **C** and **D**, Training algorithm. In **c**, we converted the ILEE samples to a feature value – estimated K_2 with -0.2 of average deviation rate of pixels with top 5% DT in binary ground truth. Specifically, for each original or interpolated image sample (shown by independent lines, where different color represents different fold of interpolation), ILEE binary results using various single K_2 are compared with corresponding ground truth image to calculate the deviation rate, defined as the fold of difference of Euclidian distance transformation (DT) of ILEE result vs ground truth relative to ground truth. The averaged deviation rate of pixels with top 5% DT are taken as a feature value to represent thick filament. Next this feature was correlated to the corresponding K_2, and linear regressions were conducted to estimate the $\log_{10}$ of the optimal K_2 that renders -0.2 for average deviation rate for each sample. Finally, the estimated optimal K_2 and the average DT of pixels with top 5% DT of each sample were utilized (shown in **d**) to generate an exponential regression model. This model covers the vast majority (if not all) of possible highest filament thickness rendered by confocal microscope images of cytoskeleton. The average DT of pixels with top 5% DT estimated by Niblack thresholding were used as an independent variable for optimal K_2 estimation.

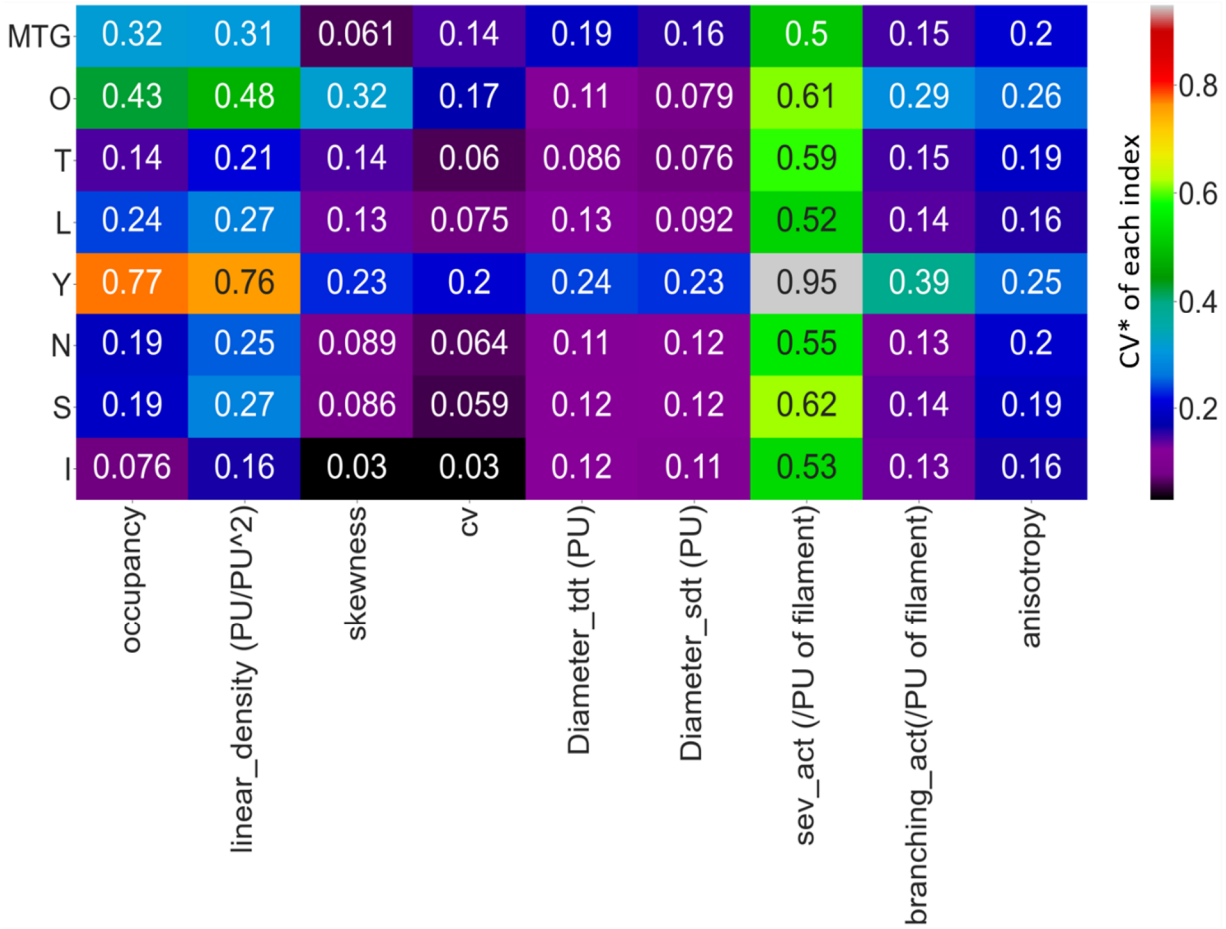

Figure AA-9: The stability of ILEE and other classic image thresholding approaches for cytoskeleton segregation in confocal images. The coefficient of variation (CV*) of each index rendered by each approach in Fig. 4**d** were calculated and visualized as a heatmap. O, Ostu; T, Triangle; L, Li; Y, Yan; N, Niblack; S, Sauvola; I, ILEE. ILEE has a dominantly low CV* (i.e., high stability) over diverse sample for *occupancy*, *linear density*, *skewness*, *CV*, or one of the lowest for other indices. Note that the CV* of the computed indices in the figure and the fluorescence *CV* of a sample, which is a cytoskeletal index, are different concepts.

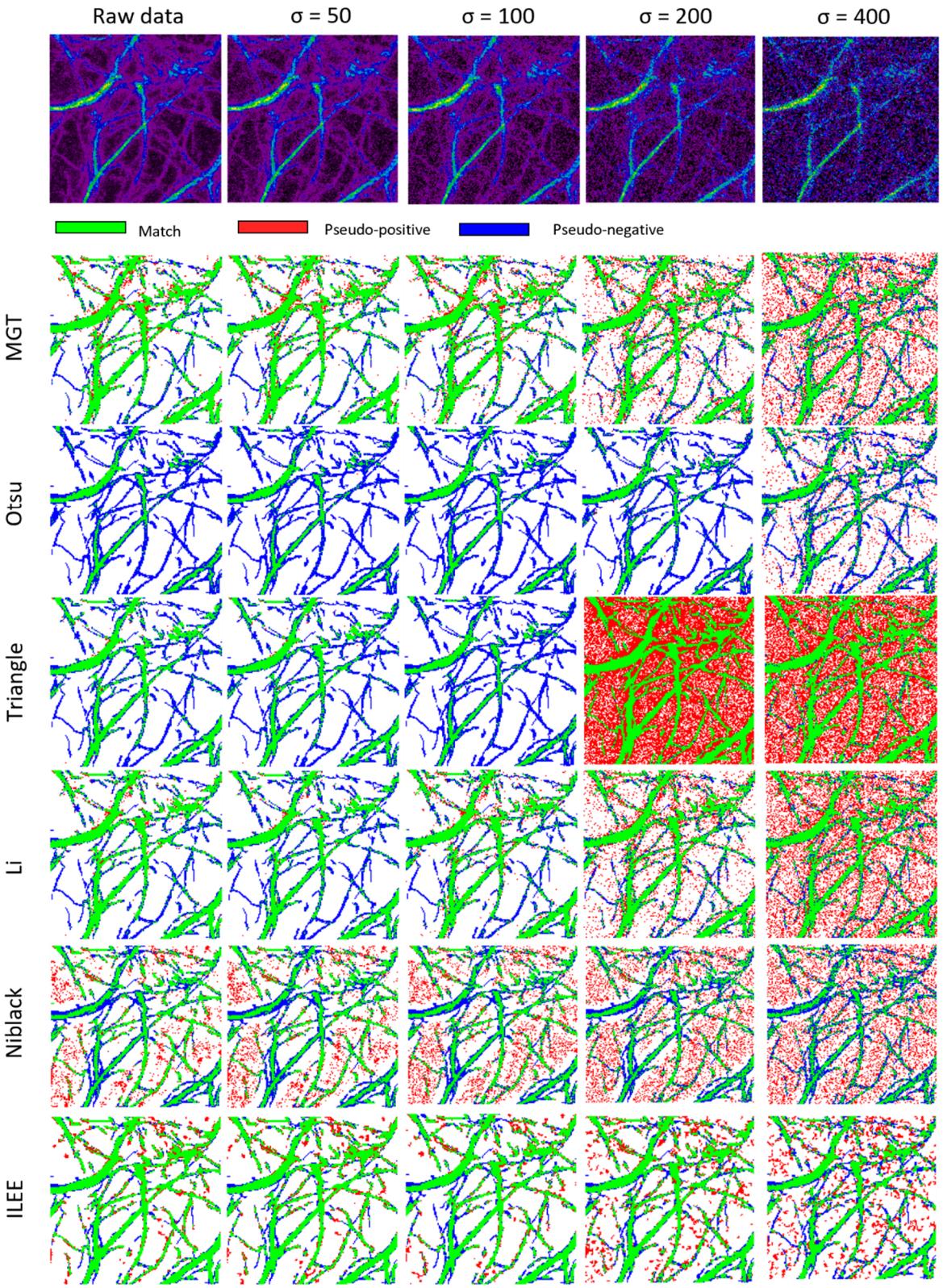

Figure AA-10: The visualized comparison of robustness of ILEE and other algorithms by segmentation accuracy. The presentation image Figure 2-5A are added with a series of gaussian…

Figure AA-10 (cont'd) … noise (μ = 0, σ as variable). The binary images are computed by selected algorithms including ILEE and compared with manually portraited ground truth, and pixels of match, pseudo-positive, and pseudo-negative are presented. By visual observation, all of the algorithms are stable when the σ of noise is within 100 (3~4% of max of dynamic range); 3 of the better performed algorithms, ILEE, MGT, and Li, remain accurate, among which ILEE has the best coverage of ground truth. When σ of noise is higher than 100, all algorithms become visibly unstable. While MGT and Li tend to have single pixel errors while ILEE tends to result in block-shaped errors that are less in number and mimics the thickness of the cytoskeleton in shape, which indicates that the indices derived from ILEE are potentially more accurate at high noise conditions.

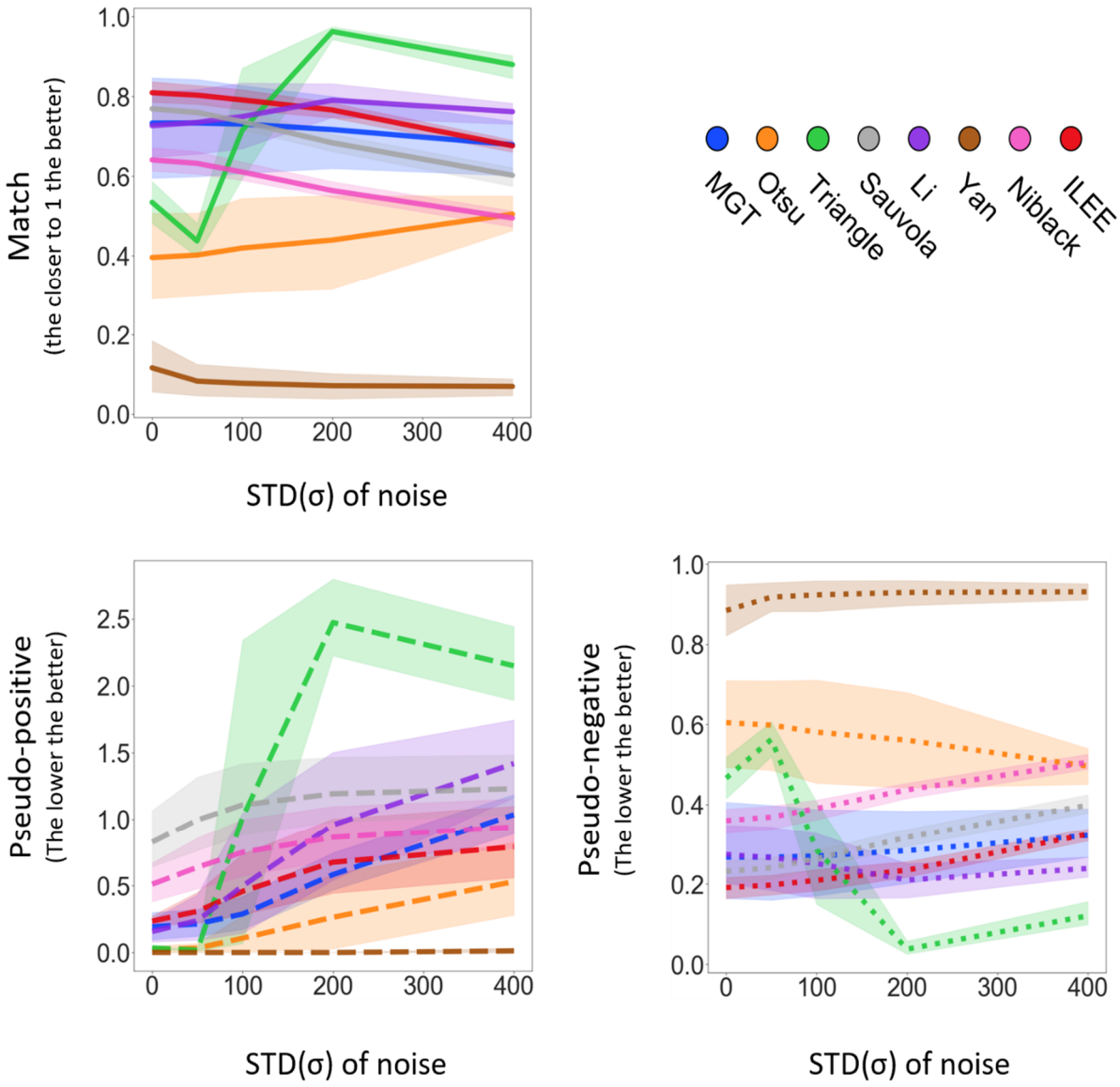

Figure AA-11: The quantificational comparison of robustness of ILEE and other algorithms by segmentation accuracy. The dataset of Figure 2-5B, C, and D are added with a series of gaussian noise (μ = 0, σ as a variable). Since gaussian noise is random and potential unstable, each sample-noise combination are technically repeated by 12 times and the averaged result is used. The transparent area with light color indicates 95% confidence interval of each algorithm. The binary images rendered by different algorithms are compared with manually portraited ground truth to count the pixels that are matched (ideally 1.0), pseudo-positive (ideally 0), and pseudo-negative (ideally 0). Generally speaking, ILEE is the best-performing algorithm with high match, low pseudo-positive, and low pseudo-negative rate at both low and high noise. Other algorithms have one or more flaws.

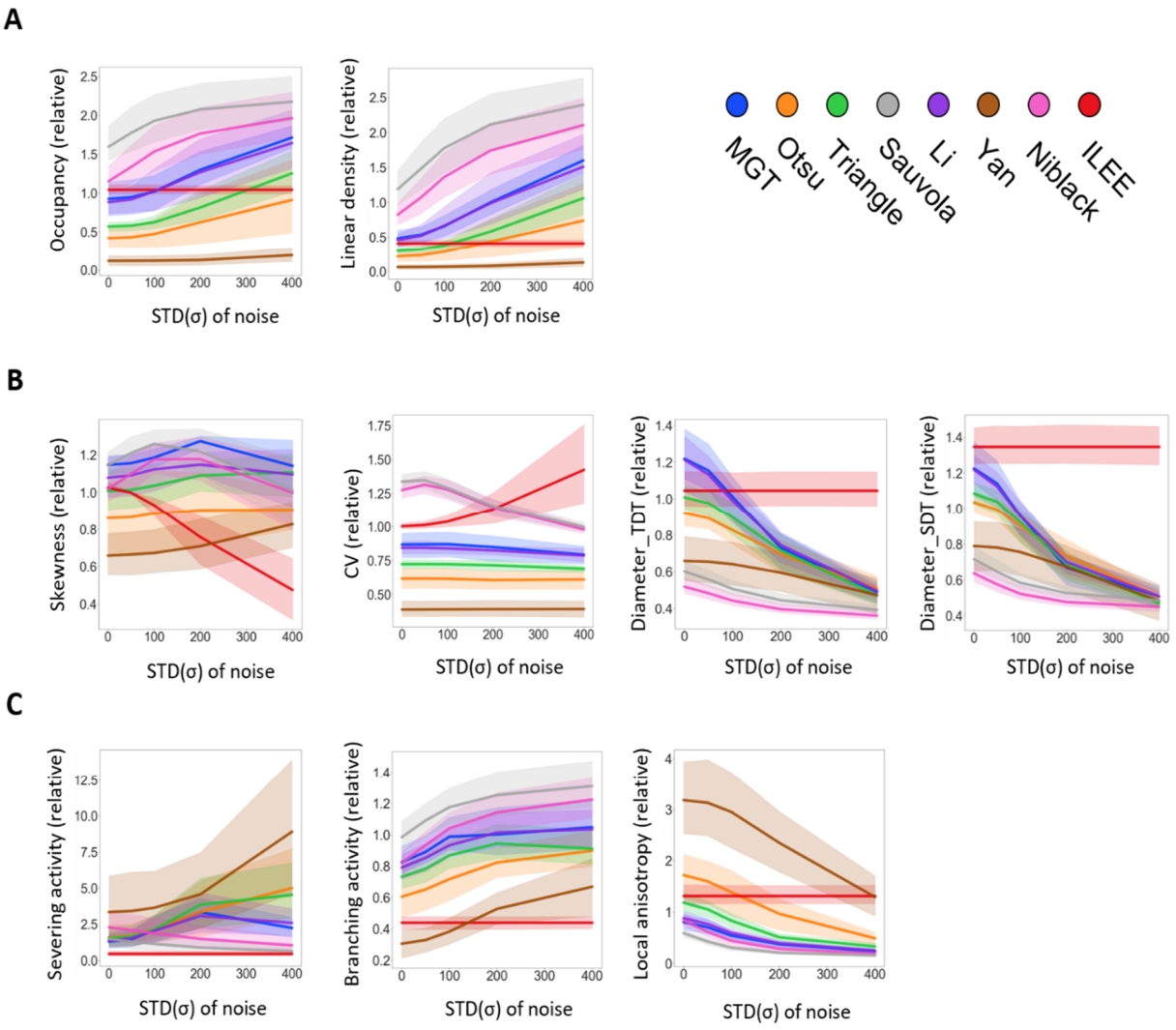

Figure AA-12: The quantificational comparison of robustness of ILEE and other algorithms by index rendering stability. Like Figure AA-11, the dataset of Figure 2-5B, C, and D are added with a series of gaussian noise (μ = 0, σ as variable), segmented by aforementioned algorithms, and their indices are computed and presented as the relative value to the ground truth. Each sample-noise combination are technically repeated by 12 times and the averaged result was used. The transparent area with light color indicates 95% confidence interval of each algorithm. For each figure, the lines with plainer slope indicate higher robustness (resistance to noise); being closer to 1.0 by value indicates higher accuracy. **A**, Index class of density; **B**, index class of bundling; **c**, indices of other classes. For most of the indices, ILEE provide an extremely stable result against increasing noise, while other algorithms has very obvious change of value of output indices and are therefore no longer accurate (if they were), which echoes the visual observation of Figure AA-11. Interestingly, *skewness* and *CV* are two exceptions, where ILEE shows more instability and tends to have a bifurcated direction of change.

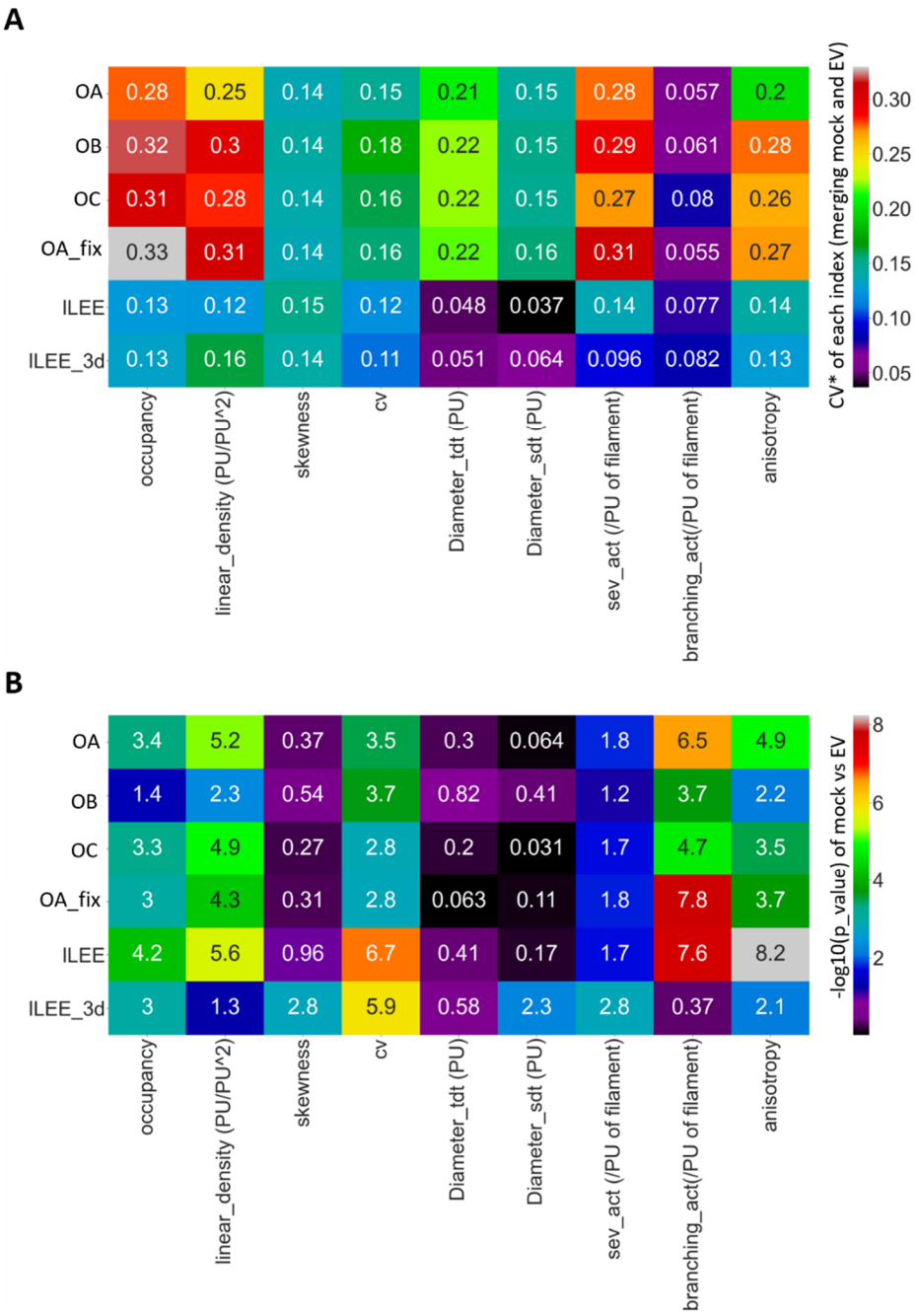

Figure AA-13: The stability/robustness of ILEE and MGT in batch analysis of biological samples of Figure 2-6. A, The coefficient of variation (CV^*) of each index rendered by ILEE and MGT by different operators. The individual CV^*s of mock and EV group for each index-method combination are merged. ILEE or ILEE_3d got the lowest CV^* (or highest stability) on *occupancy*, *linear density*, (fluorescence) *CV*, *Diameter_TDT/SDT*, *severing activity*, and *anisotropy*. **B**, A comparison of the t-test P value of mock versus *P. syringae* (EV)-inoculated sample rendered by ILEE and MGT by different operators. ILEE or ILEE_3d has the highest $-\log_{10}$ P value (i.e., lowest P value) on *occupancy*, *linear density*, *skewness*, (fluorescence) *CV*, *Diameter_SDT*, *severing activity*, and *anisotropy*. Note that the CV^* of computed indices in the figure and the fluorescence *CV* of the samples, which is a cytoskeletal index, are different concept.

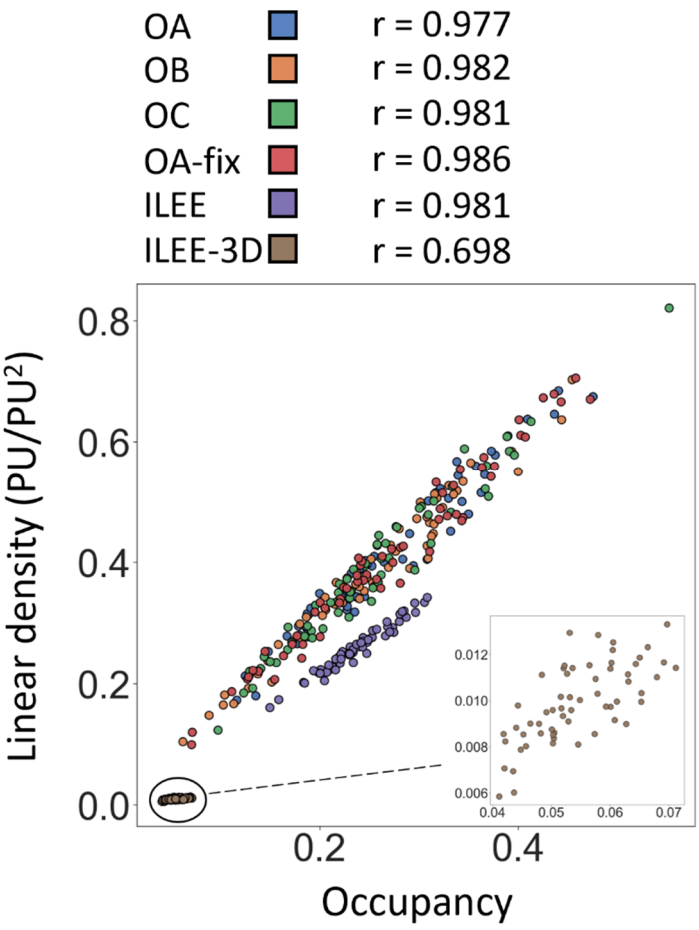

Figure AA-14: The correlation of *occupancy* and *linear density.* The *occupancy* and *linear density* rendered by ILEE and MGT shown in Figure 5 are corelated. The *occupancy* and *linear density* generally have a very high linear correlation, indicating that they agree with each other on evaluating the cytoskeletal density. ILEE and MGT does not display the same mathematical relationship, indicating that ILEE and MGT possess different tendencies in rendering the topological structure (mostly influencing linear density). In the 3D mode, they only have medium-strong correlation, potentially because the 3D topological structure cannot be perfectly rendered due to concave/convex structures present in the skeletonized images. Additionally, this could be the result of abandoned oversampling process for generating the skeletonized image due to insufficient computational power for standard PCs.

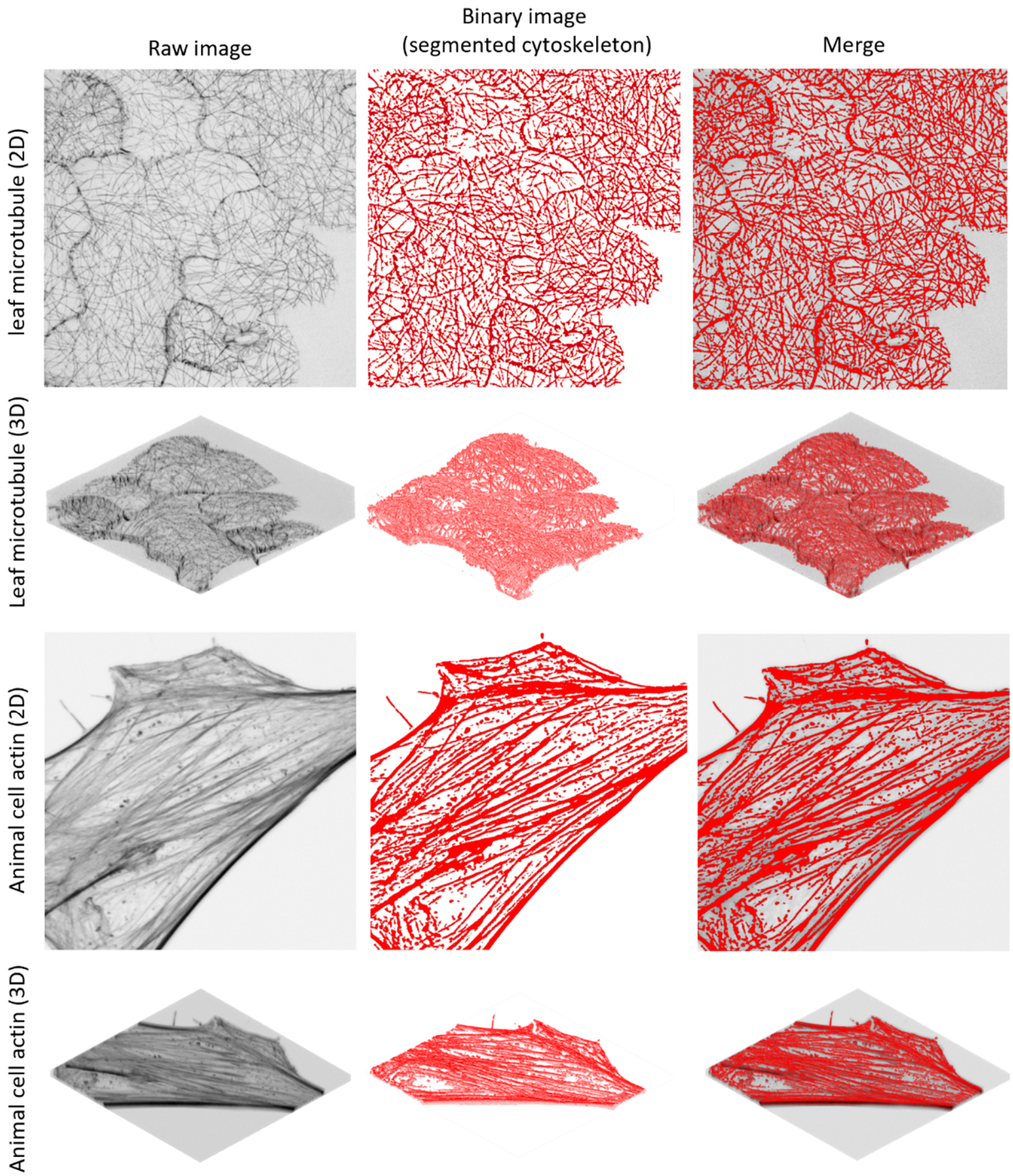

Figure AA-15: The performance of ILEE on other type of biological sample. We tested ILEE on leaf microtubule images of Arabidopsis Col-0/GFP-MAP4 and animal cell actin images of YUMMER1.7D4 line. The Col-0/GFP-MAP4 images were generously provided by Dr. Silke Robatzek (Ludwig-Maximilians-Universität München) from a previously published dataset. The result indicates ILEE accurately covers the cytoskeleton samples with locally dynamic brightness, thickness, and shape, with no visible difference compared with its performance on leaf actin images.

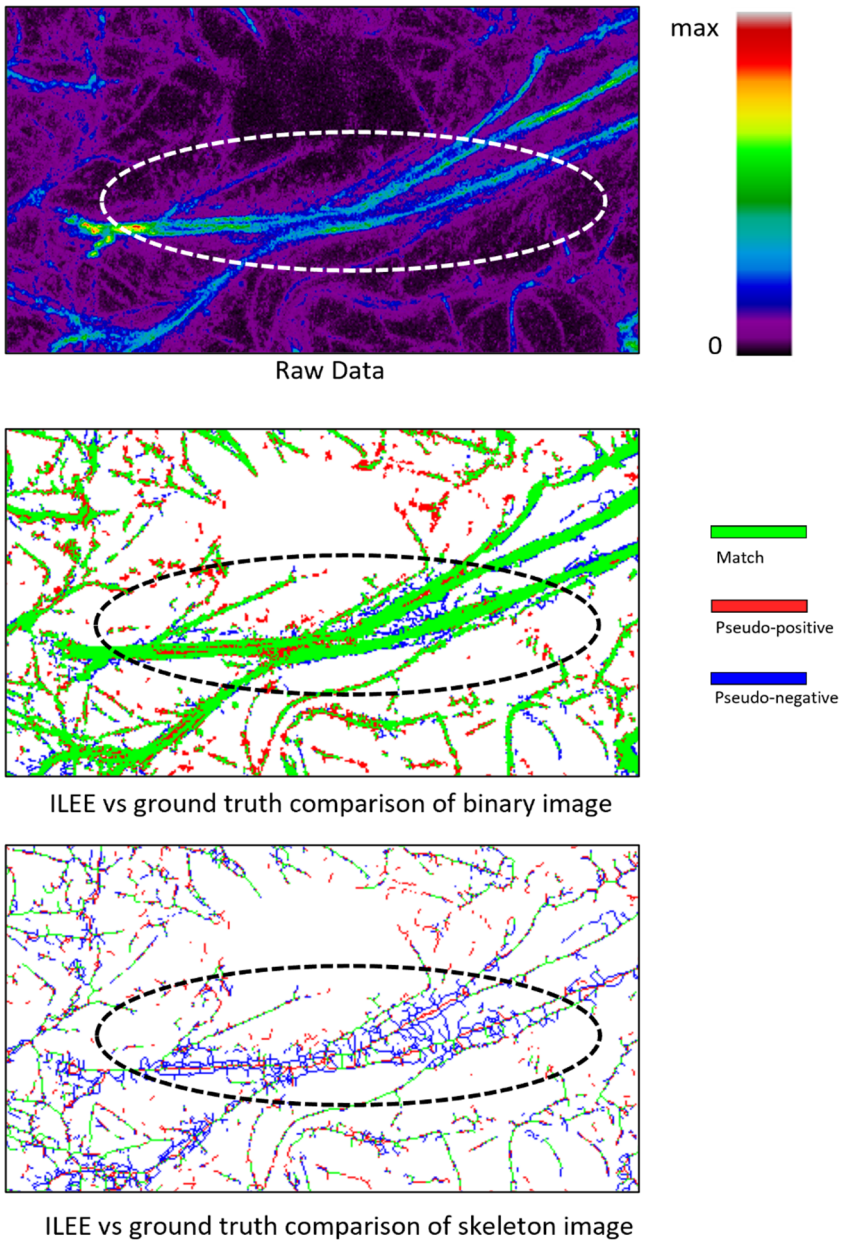

Figure AA-16. ILEE and human eye have different tendency to judge the topological structure of cytoskeleton, especially between two bright bundles. A cropped portion of the demonstration image from Fig. 3**a** and its derived images are generated and demonstrated to explain the discrepancy related to the determination of the topological structure between ILEE and hand-drawn binary ground truth (i.e., human eye evaluation). When ILEE binary image is compared with ground truth, they mostly match with each other with only minor and non-influential differences. When both binary images were skeletonized based on their topological structure, a numerous branches were detected from the ground truth, but not from ILEE. This phenomenon is very obvious in the highlighted (i.e., circled) area, where two bright actin bundles are very close to each other. This is intriguing, as where the human eye identified many branches and intervals, ILEE did not. These structures have a strong impact on the topological structure. Therefore, the topology-sensitive indices, *linear density*, *severing activity*, and *branching activity* display contrast and stable inconformity between ground truth and ILEE. However, since the hand-drawn ground truth image is not a rigorously defined ground truth, we surmise that inconformity cannot be interpreted to any inaccuracy of ILEE.

Appendix B: Proposed future experiments

Appendix B describes the critical experiments to be conducted after the submission of this dissertation, related to this study herein. It includes the preparation of high-order ADF mutant facilitated by CRISPR-Cas9 system (see Figure AB-1, below), and IP-MS based identification of ADF in vivo Phosphorylation sites (See Figure AB-2, next page).

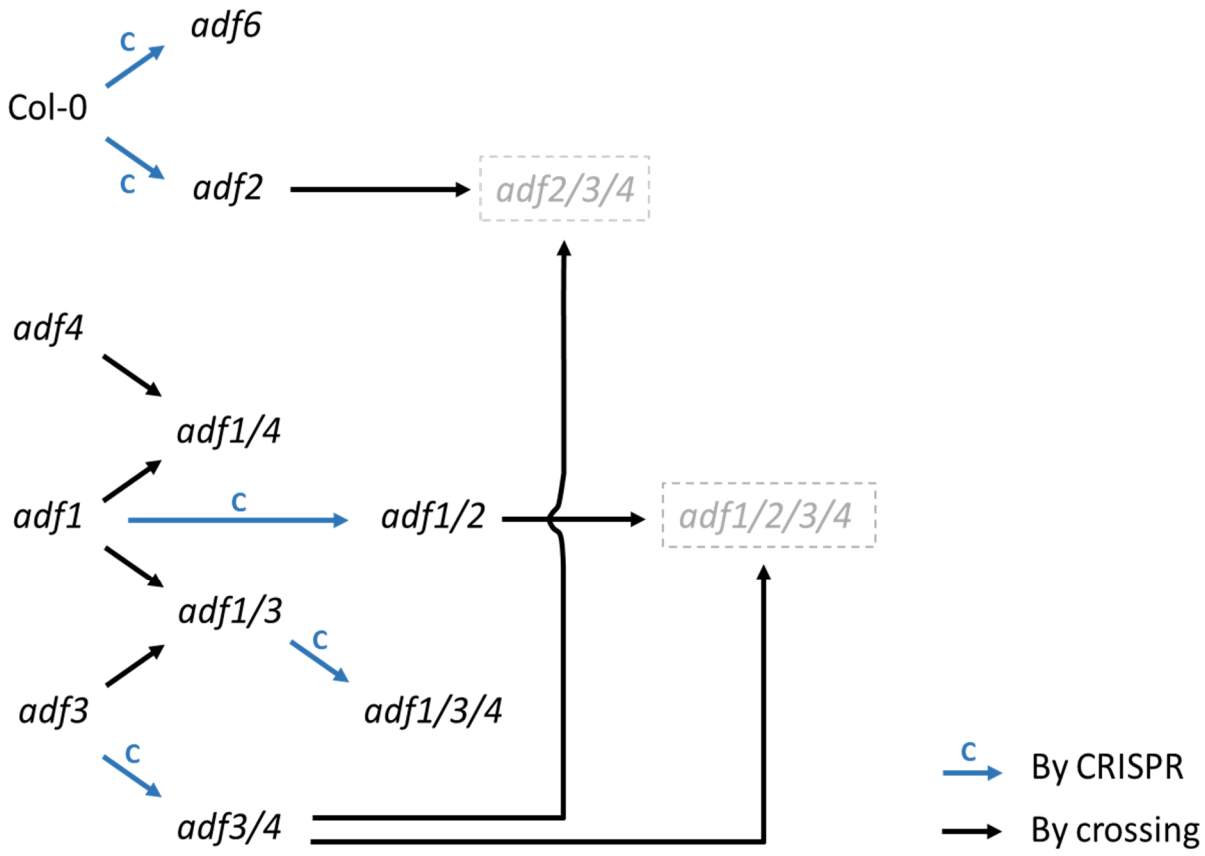

Figure AB-1: the technical route to construct the high-order mutant lines of ADFs. Blue arrow indicates knocking-out the gene by CRISPR-Cas9; black arrow indicates general crossing. Black text as the name indicates the mutant has been successfully constructed by the submission of this dissertation; grey text with dashed boarder as the name indicates the mutant is to be prepared soon.

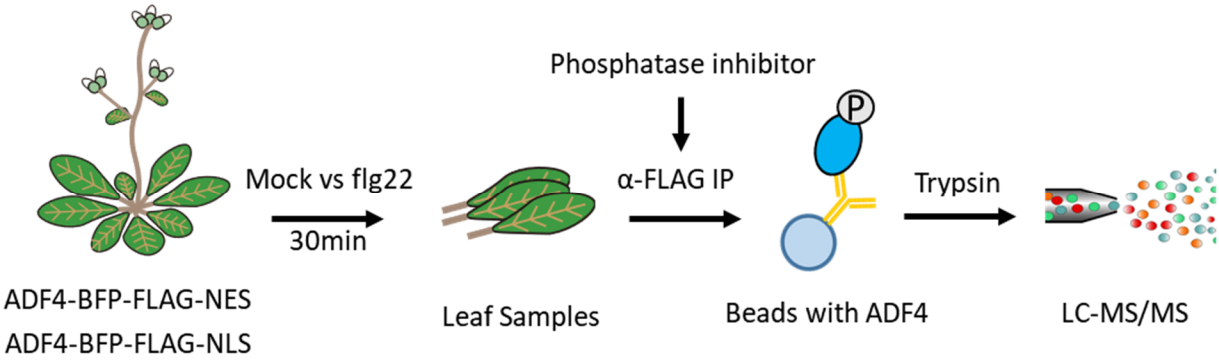

Figure AB-2: the scheme diagram describing the IP-MS based identification of ADF4 in vivo phosphorylation sites. adf4/ADF4-BFP-FLAG-NES/NLS plants are grown to 5-week-old; flg22 or mock is injected into the leaves and the samples are harvested 30 min post treatment. The leaf samples are homogenized with abundant phosphatase in the buffer, and an α-FLAG IP is conducted to purify all ADF4 fractions. The purified beads will be digested for a spectrometer assay (LC-MS/MS) to identified the phosphorylation on ADF4 residues.

Appendix C: specialized primers in this study

Appendix C lists the primers specifically designed for generation of ADF4 mutations and detection of W-box fractions by ChIP-qPCR (see below).

	Primer name	Sequence
For ADF4 mutation	ADF4-dα3-P2-F	TAGCAAAGGTG**GCG**AGC**GC**GATGATCTATGCGAGCTCTAAGGAC
	ADF4-dα3-P1-R	CGCATAGATCATC**GC**GCT**CGC**CACCTTTGCTACGTCGGG
	ADF4 S99D-p2 for	TAGCAAAGGTGAGA**GA**CAAGATGATCTATGCGAGC
	ADF4 S99D-p1 rev	GCATAGATCATCTTGTCT**CT**CACCTTTGCTACGTC
	ADF4 T124E-p2 for	TGGAGCTTCAAGCA**GAA**GATCCAACTGAGATGGAT
	ADF4 T124E-p1 rev	ATCTCAGTTGGATC**TTC**TGCTTGAAGCTCCACTTG
	ADF4 T127E-p2 for	AAGCAACTGATCCA**GAA**GAGATGGATCTTGATGTT
	ADF4 T127E-p1 rev	TCAAGATCCATCTC**TTC**TGGATCAGTTGCTTGAAG
	ADF4 S136E rev stop	TTAGTTGACGCG**TTC**TTTCAAAACATCAAGATCCA
For ChIP-qPCR	pW29_Wbox1-F	TCAAATCGAACTCACAGAAGTC
	pW29_Wbox1-R	TGACCATTTCTGTTGGAAAACA
	pW29_Wbox2-F	AGTTGCAAGAGTAAGCTGACT
	pW29_wBoxII-R	GCGATGGAGATTAAAAGTTGGC
	pW29_Wbox3-F	TGGACCGAAATATTTAAGACCA
	pW29_Wbox3-R	CTATCAAATGGAAACCGAGATGA
	pW29_Wbox4/5-Fv2	TGGACTTTCCTGAATGTTGTGT
	pW29_Wbox4/5-Rv2	CGTTTCCCATGTGAACCCGT
	pBAG7/-213R	ATATTGAAGATAACCGTGTGT
	pBAG7/-297F	AAGATTCTCTTGTCGACGTA
	Act2_ChIP-For	CCATCCTCCGTCTTGACCTT
	Act2_ChIP-Re	ACTTGCCCATCGGGTAATTC

Table AC-1: list of specialized primers used in the study herein. Primers for ADF4 mutation and ChIP-qPCR are listed. The bold underlined bases indicate mutation comparing to the wild type gene.

REFERENCES

REFERENCES

Alioscha-Perez, M., Benadiba, C., Goossens, K., Kasas, S., Dietler, G., Willaert, R., and Sahli, H. (2016). A Robust Actin Filaments Image Analysis Framework. PLoS Comput Biol 12: e1005063.

Anderson, J.C., Bartels, S., Besteiro, M.A.G., Shahollari, B., Ulm, R., and Peck, S.C. (2011). Arabidopsis MAP Kinase Phosphatase 1 (AtMKP1) negatively regulates MPK6-mediated PAMP responses and resistance against bacteria. The Plant Journal 67: 258–268.

Anjago, W.M., Zhou, T., Zhang, H., Shi, M., Yang, T., Zheng, H., and Wang, Z. (2018). Regulatory network of genes associated with stimuli sensing, signal transduction and physiological transformation of appressorium in Magnaporthe oryzae. Mycology 9: 211–222.

Arnaud, D. and Hwang, I. (2015). A Sophisticated Network of Signaling Pathways Regulates Stomatal Defenses to Bacterial Pathogens. Molecular Plant 8: 566–581.

Asai, T., Tena, G., Plotnikova, J., Willmann, M.R., Chiu, W.-L., Gomez-Gomez, L., Boller, T., Ausubel, F.M., and Sheen, J. (2002). MAP kinase signalling cascade in Arabidopsis innate immunity. Nature 415: 977–983.

Auyong, A.S. (2015). The Role of Cutinase and its Impact on Pathogenicity of Colletotrichum truncatum. J Plant Pathol Microbiol 06.

Bacete, L., Mélida, H., Miedes, E., and Molina, A. (2018). Plant cell wall-mediated immunity: cell wall changes trigger disease resistance responses. The Plant Journal 93: 614–636.

Baker, C.M., Chitrakar, R., Obulareddy, N., Panchal, S., Williams, P., and Melotto, M. (2010). Molecular battles between plant and pathogenic bacteria in the phyllosphere. Braz J Med Biol Res 43: 698–704.

Balint-Kurti, P. (2019). The plant hypersensitive response: concepts, control and consequences. Molecular Plant Pathology 20: 1163–1178.

Bartolák-Suki, E., Imsirovic, J., Nishibori, Y., Krishnan, R., and Suki, B. (2017). Regulation of Mitochondrial Structure and Dynamics by the Cytoskeleton and Mechanical Factors. International Journal of Molecular Sciences 18: 1812.

Beck, M., Zhou, J., Faulkner, C., MacLean, D., and Robatzek, S. (2012). Spatio-Temporal Cellular Dynamics of the Arabidopsis Flagellin Receptor Reveal Activation Status-Dependent Endosomal Sorting. The Plant Cell 24: 4205–4219.

Bellincampi, D., Cervone, F., and Lionetti, V. (2014). Plant cell wall dynamics and wall-related susceptibility in plant–pathogen interactions. Frontiers in Plant Science 5: 228.

Bielig, H. et al. (2014). The Cofilin Phosphatase Slingshot Homolog 1 (SSH1) Links NOD1 Signaling to Actin Remodeling. PLOS Pathogens 10: e1004351.

Biezen, E.A.V.D. and Jones, J.D.G. (1998). Plant disease-resistance proteins and the gene-for-gene concept. Trends in Biochemical Sciences 23: 454–456.

Birkenbihl, R.P., Kracher, B., Roccaro, M., and Somssich, I.E. (2017). Induced Genome-Wide Binding of Three Arabidopsis WRKY Transcription Factors during Early MAMP-Triggered Immunity. The Plant Cell 29: 20–38.

Blanchoin, L., Boujemaa-Paterski, R., Sykes, C., and Plastino, J. (2014). Actin Dynamics, Architecture, and Mechanics in Cell Motility. Physiol Rev 94: 29.

Block, A., Guo, M., Li, G., Elowsky, C., Clemente, T.E., and Alfano, J.R. (2010). The Pseudomonas syringae type III effector HopG1 targets mitochondria, alters plant development and suppresses plant innate immunity. Cellular Microbiology 12: 318–330.

Bonardi, V., Tang, S., Stallmann, A., Roberts, M., Cherkis, K., and Dangl, J.L. (2011). Expanded functions for a family of plant intracellular immune receptors beyond specific recognition of pathogen effectors. PNAS 108: 16463–16468.

Boudaoud, A., Burian, A., Borowska-Wykręt, D., Uyttewaal, M., Wrzalik, R., Kwiatkowska, D., and Hamant, O. (2014). FibrilTool, an ImageJ plug-in to quantify fibrillar structures in raw microscopy images. Nature Protocols 9: 457–463.

Boutrot, F. and Zipfel, C. (2017). Function, Discovery, and Exploitation of Plant Pattern Recognition Receptors for Broad-Spectrum Disease Resistance. Annual Review of Phytopathology 55: 257–286.

Brandizzi, F. and Wasteneys, G.O. (2013). Cytoskeleton-dependent endomembrane organization in plant cells: an emerging role for microtubules. The Plant Journal 75: 339–349.

Brandt, B., Brodsky, D.E., Xue, S., Negi, J., Iba, K., Kangasjärvi, J., Ghassemian, M., Stephan, A.B., Hu, H., and Schroeder, J.I. (2012). Reconstitution of abscisic acid activation of SLAC1 anion channel by CPK6 and OST1 kinases and branched ABI1 PP2C phosphatase action. PNAS 109: 10593–10598.

Braun, U., Shin, H.D., Takamatsu, S., Meeboon, J., Kiss, L., Lebeda, A., Kitner, M., and Götz, M. (2019). Phylogeny and taxonomy of Golovinomyces orontii revisited. Mycol Progress 18: 335–357.

Brouhard, G.J. (2018). Microtubule dynamics: an interplay of biochemistry and mechanics.: 13.

Bücherl, C.A., Jarsch, I.K., Schudoma, C., Segonzac, C., Mbengue, M., Robatzek, S., MacLean, D., Ott, T., and Zipfel, C. (2017). Plant immune and growth receptors share common signalling components but localise to distinct plasma membrane nanodomains. eLife 6: e25114.

Cai, G., Faleri, C., Del Casino, C., Emons, A.M.C., and Cresti, M. (2011). Distribution of Callose Synthase, Cellulose Synthase, and Sucrose Synthase in Tobacco Pollen Tube Is Controlled in Dissimilar Ways by Actin Filaments and Microtubules. Plant Physiology 155: 1169–1190.

Caplan, J.L., Kumar, A.S., Park, E., Padmanabhan, M.S., Hoban, K., Modla, S., Czymmek, K., and Dinesh-Kumar, S.P. (2015). Chloroplast Stromules Function during Innate Immunity. Developmental Cell 34: 45–57.

Caplan, J.L., Mamillapalli, P., Burch-Smith, T.M., Czymmek, K., and Dinesh-Kumar, S.P. (2008). Chloroplastic Protein NRIP1 Mediates Innate Immune Receptor Recognition of a Viral Effector. Cell 132: 449–462.

cesari, S., Bernoux, M., Moncuquet, P., Kroj, T., and Dodds, P. (2014). A novel conserved mechanism for plant NLR protein pairs: the 'integrated decoy' hypothesis. Frontiers in Plant Science 5: 606.

Chang, H.-X., Miller, L.A., and Hartman, G.L. (2014). Melanin-Independent Accumulation of Turgor Pressure in Appressoria of Phakopsora pachyrhizi. Phytopathology® 104: 977–984.

Chappelka, A.H. and Grulke, N.E. (2016). Disruption of the 'disease triangle' by chemical and physical environmental change. Plant Biology 18: 5–12.

Cheng, F., Ma, A., Zhuang, X., He, X., and Zhuang, G. (2016). N-(3-oxo-hexanoyl)-homoserine lactone has a critical contribution to the quorum-sensing-dependent regulation in phytopathogen Pseudomonas syringae pv. tabaci 11528. FEMS Microbiology Letters 363.

Cheong, M.S., Kirik, A., Kim, J.-G., Frame, K., Kirik, V., and Mudgett, M.B. (2014). AvrBsT Acetylates Arabidopsis ACIP1, a Protein that Associates with Microtubules and Is Required for Immunity. PLOS Pathogens 10: e1003952.

Chisholm, S.T., Coaker, G., Day, B., and Staskawicz, B.J. (2006). Host-Microbe Interactions: Shaping the Evolution of the Plant Immune Response. Cell 124: 803–814.

Claus, L.A.N., Savatin, D.V., and Russinova, E. (2018). The crossroads of receptor-mediated signaling and endocytosis in plants. Journal of Integrative Plant Biology 60: 827–840.

Coates, M.E. and Beynon, J.L. (2010). Hyaloperonospora arabidopsidis as a Pathogen Model. Annual Review of Phytopathology 48: 329–345.

Couto, D. et al. (2016). The Arabidopsis Protein Phosphatase PP2C38 Negatively Regulates the Central Immune Kinase BIK1. PLOS Pathogens 12: e1005811.

Couto, D. and Zipfel, C. (2016). Regulation of pattern recognition receptor signalling in plants. Nat Rev Immunol 16: 537–552.

Day, B., Henty, J.L., Porter, K.J., and Staiger, C.J. (2011). The Pathogen-Actin Connection: A Platform for Defense Signaling in Plants. Annual Review of Phytopathology 49: 483–506.

Desbrun, M., Meyer, M., Schröder, P., and Barr, A.H. (1999). Implicit fairing of irregular meshes using diffusion and curvature flow. In Proceedings of the 26th annual conference on Computer graphics and interactive techniques - SIGGRAPH '99 (ACM Press: Not Known), pp. 317–324.

Dong, J. and Chen, W. (2013). The Role of Autophagy in Chloroplast Degradation and Chlorophagy in Immune Defenses during Pst DC3000 (AvrRps4) Infection. PLOS ONE 8: e73091.

Du, J., Wang, X., Dong, C.-H., Yang, J.M., and Yao, X.J. (2016). Computational Study of the Binding Mechanism of Actin-Depolymerizing Factor 1 with Actin in Arabidopsis thaliana. PLOS ONE 11: e0159053.

Duxbury, Z. (2016). Determining the molecular mechanism of plant disease resistance following pathogen effector perception by the resistance gene pair RPS4/RRS1.

Elliott, A. and Shaw, S.L. (2018). Update: Plant Cortical Microtubule Arrays. Plant Physiology 176: 94–105.

Erickson, J.L., Adlung, N., Lampe, C., Bonas, U., and Schattat, M.H. (2018). The Xanthomonas effector XopL uncovers the role of microtubules in stromule extension and dynamics in Nicotiana benthamiana. The Plant Journal 93: 856–870.

Fan, L., Li, R., Pan, J., Ding, Z., and Lin, J. (2015). Endocytosis and its regulation in plants. Trends in Plant Science 20: 388–397.

Faulkner, C., Zhou, J., Evrard, A., Bourdais, G., MacLean, D., Häweker, H., Eckes, P., and Robatzek, S. (2017). An automated quantitative image analysis tool for the identification of microtubule patterns in plants. Traffic 18: 683–693.

Fawke, S., Doumane, M., and Schornack, S. Oomycete Interactions with Plants: Infection Strategies and Resistance Principles. Microbiology and Molecular Biology Reviews 79: 263–280.

Frei dit Frey, N. et al. (2014). Functional analysis of Arabidopsisimmune-related MAPKs uncovers a role for MPK3 as negative regulator of inducible defences. Genome Biology 15: R87.

Fu, Y., Duan, X., Tang, C., Li, X., Voegele, R.T., Wang, X., Wei, G., and Kang, Z. (2014). TaADF7, an actin-depolymerizing factor, contributes to wheat resistance against Puccinia striiformis f. sp. tritici. The Plant Journal 78: 16–30.

Gao, X., Chen, X., Lin, W., Chen, S., Lu, D., Niu, Y., Li, L., Cheng, C., McCormack, M., Sheen, J., Shan, L., and He, P. (2013). Bifurcation of Arabidopsis NLR Immune Signaling via Ca2+-Dependent Protein Kinases. PLOS Pathogens 9: e1003127.

Geng, X., Cheng, J., Gangadharan, A., and Mackey, D. (2012). The Coronatine Toxin of Pseudomonas syringae Is a Multifunctional Suppressor of Arabidopsis Defense. The Plant Cell 24: 4763–4774.

Guan, X., Buchholz, G., and Nick, P. (2013). The cytoskeleton is disrupted by the bacterial effector HrpZ, but not by the bacterial PAMP flg22, in tobacco BY-2 cells. Journal of Experimental Botany 64: 1805–1816.

Guo, M., Kim, P., Li, G., Elowsky, C.G., and Alfano, J.R. (2016). A Bacterial Effector Co-opts Calmodulin to Target the Plant Microtubule Network. Cell Host & Microbe 19: 67–78.

Hanson, M.R. and Hines, K.M. (2018). Stromules: Probing Formation and Function. Plant Physiology 176: 128–137.

He, Z., Huang, T., Ao, K., Yan, X., and Huang, Y. (2017). Sumoylation, Phosphorylation, and Acetylation Fine-Tune the Turnover of Plant Immunity Components Mediated by Ubiquitination. Frontiers in Plant Science 8: 1682.

Henty-Ridilla, J.L., Li, J., Day, B., and Staiger, C.J. (2014). ACTIN DEPOLYMERIZING FACTOR4 Regulates Actin Dynamics during Innate Immune Signaling in *Arabidopsis*. Plant Cell 26: 340–352.

Henty-Ridilla, J.L., Shimono, M., Li, J., Chang, J.H., Day, B., and Staiger, C.J. (2013). The Plant Actin Cytoskeleton Responds to Signals from Microbe-Associated Molecular Patterns. PLOS Pathogens 9: e1003290.

Higaki, T., Akita, K., and Katoh, K. (2020). Coefficient of variation as an image-intensity metric for cytoskeleton bundling. Scientific Reports 10: 22187.

Higaki, T., Kutsuna, N., Sano, T., Kondo, N., and Hasezawa, S. (2010). Quantification and cluster analysis of actin cytoskeletal structures in plant cells: role of actin bundling in stomatal movement during diurnal cycles in Arabidopsis guard cells. The Plant Journal 61: 156–165.

Hong, J.-S. and Ju, H.-J. (2017). The Plant Cellular Systems for Plant Virus Movement. Plant Pathol J 33: 213–228.

Hsu, F.-C., Chou, M.-Y., Chou, S.-J., Li, Y.-R., Peng, H.-P., and Shih, M.-C. (2013). Submergence Confers Immunity Mediated by the WRKY22 Transcription Factor in Arabidopsis. The Plant Cell 25: 2699–2713.

Hu, Y., Dong, Q., and Yu, D. (2012). Arabidopsis WRKY46 coordinates with WRKY70 and WRKY53 in basal resistance against pathogen Pseudomonas syringae. Plant Science 185–186: 288–297.

Huot, B., Yao, J., Montgomery, B.L., and He, S.Y. (2014). Growth–Defense Tradeoffs in Plants: A Balancing Act to Optimize Fitness. Molecular Plant 7: 1267–1287.

Hussain, A., Noman, A., Khan, M.I., Zaynab, M., Aqeel, M., Anwar, M., Ashraf, M.F., Liu, Z., Raza, A., Mahpara, S., Bakhsh, A., and He, S. (2019). Molecular regulation of pepper innate immunity and stress tolerance: An overview of WRKY TFs. Microbial Pathogenesis 135: 103610.

Inada, N., Higaki, T., and Hasezawa, S. (2016). Nuclear Function of Subclass I Actin-Depolymerizing Factor Contributes to Susceptibility in Arabidopsis to an Adapted Powdery Mildew Fungus. Plant Physiology 170: 1420–1434.

Jeworutzki, E., Roelfsema, M.R.G., Anschütz, U., Krol, E., Elzenga, J.T.M., Felix, G., Boller, T., Hedrich, R., and Becker, D. (2010). Early signaling through the Arabidopsis pattern recognition receptors FLS2 and EFR involves Ca2+-associated opening of plasma membrane anion channels. The Plant Journal 62: 367–378.

Jiang, J., Ma, S., Ye, N., Jiang, M., Cao, J., and Zhang, J. (2017a). WRKY transcription factors in plant responses to stresses. Journal of Integrative Plant Biology 59: 86–101.

Jiang, L., Anderson, J.C., Besteiro, M.A.G., and Peck, S.C. (2017b). Phosphorylation of Arabidopsis MAP Kinase Phosphatase 1 (MKP1) Is Required for PAMP Responses and Resistance against Bacteria. Plant Physiology 175: 1839–1852.

Jiang, L., Chen, Y., Luo, L., and Peck, S.C. (2018). Central Roles and Regulatory Mechanisms of Dual-Specificity MAPK Phosphatases in Developmental and Stress Signaling. Frontiers in Plant Science 9: 1697.

Jiang, L., Wan, Y., Anderson, J.C., Hou, J., Islam, S.M., Cheng, J., and Peck, S.C. (2017c). Genetic dissection of Arabidopsis MAP kinase phosphatase 1-dependent PAMP-induced transcriptional responses. Journal of Experimental Botany 68: 5207–5220.

Jones, J.D.G. and Dangl, J.L. (2006). The plant immune system. Nature 444: 323–329.

Journot-Catalino, N., Somssich, I.E., Roby, D., and Kroj, T. (2006). The Transcription Factors WRKY11 and WRKY17 Act as Negative Regulators of Basal Resistance in Arabidopsis thaliana. The Plant Cell 18: 3289–3302.

Jubic, L.M., Saile, S., Furzer, O.J., El Kasmi, F., and Dangl, J.L. (2019). Help wanted: helper NLRs and plant immune responses. Current Opinion in Plant Biology 50: 82–94.

Jui-Cheng Yen, Fu-Juay Chang, and Shyang Chang (1995). A new criterion for automatic multilevel thresholding. IEEE Transactions on Image Processing 4: 370–378.

Kadota, Y., Shirasu, K., and Zipfel, C. (2015). Regulation of the NADPH Oxidase RBOHD During Plant Immunity. Plant and Cell Physiology 56: 1472–1480.

Kadota, Y., Sklenar, J., Derbyshire, P., Stransfeld, L., Asai, S., Ntoukakis, V., Jones, J.D., Shirasu, K., Menke, F., Jones, A., and Zipfel, C. (2014). Direct Regulation of the NADPH Oxidase RBOHD by the PRR-Associated Kinase BIK1 during Plant Immunity. Molecular Cell 54: 43–55.

Kaksonen, M. and Roux, A. (2018). Mechanisms of clathrin-mediated endocytosis. Nat Rev Mol Cell Biol 19: 313–326.

Kanellos, G. and Frame, M.C. (2016). Cellular functions of the ADF/cofilin family at a glance. Journal of Cell Science 129: 3211–3218.

Kang, Y., Jelenska, J., Cecchini, N.M., Li, Y., Lee, M.W., Kovar, D.R., and Greenberg, J.T. (2014). HopW1 from Pseudomonas syringae Disrupts the Actin Cytoskeleton to Promote Virulence in Arabidopsis. PLoS Pathog 10: e1004232.

Kebdani, N., Pieuchot, L., Deleury, E., Panabières, F., Le Berre, J.-Y., and Gourgues, M. (2010). Cellular and molecular characterization of Phytophthora parasitica appressorium-mediated penetration. New Phytologist 185: 248–257.

Keinath, N.F., Kierszniowska, S., Lorek, J., Bourdais, G., Kessler, S.A., Shimosato-Asano, H., Grossniklaus, U., Schulze, W.X., Robatzek, S., and Panstruga, R. (2010). PAMP (Pathogen-associated Molecular Pattern)-induced Changes in Plasma Membrane Compartmentalization Reveal Novel Components of Plant Immunity *. Journal of Biological Chemistry 285: 39140–39149.

Kelpsch, D.J. and Tootle, T.L. (2018). Nuclear Actin: From Discovery to Function. The Anatomical Record 301: 1999–2013.

Kim, K.-C., Lai, Z., Fan, B., and Chen, Z. (2008). Arabidopsis WRKY38 and WRKY62 Transcription Factors Interact with Histone Deacetylase 19 in Basal Defense. The Plant Cell 20: 2357–2371.

Kleemann, J., Rincon-Rivera, L.J., Takahara, H., Neumann, U., Themaat, E.V.L. van, Does, H.C. van der, Hacquard, S., Stüber, K., Will, I., Schmalenbach, W., Schmelzer, E., and O'Connell, R.J. (2012). Sequential Delivery of Host-Induced Virulence Effectors by Appressoria and Intracellular Hyphae of the Phytopathogen Colletotrichum higginsianum. PLOS Pathogens 8: e1002643.

Kobayashi, I., Kobayashi, Y., Yamaoka, N., and Kunoh, H. (1992). Recognition of a pathogen and a nonpathogen by barley coleoptile cells. III. Responses of microtubules and actin filaments in barley coleoptile cells to penetration attempts. Can. J. Bot. 70: 1815–1823.

Krutinová, H., Trdá, L., Kalachova, T., Lamparová, L., Pospíchalová, R., Dobrev, P.I., Malínská, K., Burketová, L., Valentová, O., and Janda, M. (2018). Can Actin Depolymerization Actually Result in Increased Plant Resistance to Pathogens?

Kufer, T.A., Kremmer, E., Adam, A.C., Philpott, D.J., and Sansonetti, P.J. (2008). The pattern-recognition molecule Nod1 is localized at the plasma membrane at sites of bacterial interaction. Cellular Microbiology 10: 477–486.

Kumar, A.S., Park, E., Nedo, A., Alqarni, A., Ren, L., Hoban, K., Modla, S., McDonald, J.H., Kambhamettu, C., Dinesh-Kumar, S.P., and Caplan, J.L. (2018). Stromule extension along microtubules coordinated with actin-mediated anchoring guides perinuclear chloroplast movement during innate immunity. eLife 7: e23625.

Kyheröinen, S. and Vartiainen, M.K. (2020). Nuclear actin dynamics in gene expression and genome organization. Seminars in Cell & Developmental Biology 102: 105–112.

Lai, Z., Vinod, K., Zheng, Z., Fan, B., and Chen, Z. (2008). Roles of ArabidopsisWRKY3 and WRKY4 Transcription Factors in Plant Responses to Pathogens. BMC Plant Biol 8: 68.

Latunde-Dada, A., O'Connell, R., Nash, and Lucas, J. (2002). Stomatal penetration of cowpea (Vigna unguiculata) leaves by a Colletotrichum species causing latent anthracnose. Plant Pathology 48: 777–784.

Lee, A.H.-Y. et al. (2012). A Bacterial Acetyltransferase Destroys Plant Microtubule Networks and Blocks Secretion. PLOS Pathogens 8: e1002523.

Lee, T.C., Kashyap, R.L., and Chu, C.N. (1994). Building Skeleton Models via 3-D Medial Surface Axis Thinning Algorithms. CVGIP: Graphical Models and Image Processing 56: 462–478.

Leelarasamee, N., Zhang, L., and Gleason, C. (2018). The root-knot nematode effector MiPFN3 disrupts plant actin filaments and promotes parasitism. PLOS Pathogens 14: e1006947.

Legrand-Poels, S., Kustermans, G., Bex, F., Kremmer, E., Kufer, T.A., and Piette, J. (2007). Modulation of Nod2-dependent NF-κB signaling by the actin cytoskeleton. Journal of Cell Science 120: 1299–1310.

Lehmann, S., Serrano, M., L'Haridon, F., Tjamos, S.E., and Metraux, J.-P. (2015). Reactive oxygen species and plant resistance to fungal pathogens. Phytochemistry 112: 54–62.

Leonard, S., Hommais, F., Nasser, W., and Reverchon, S. (2017). Plant–phytopathogen interactions: bacterial responses to environmental and plant stimuli. Environmental Microbiology 19: 1689–1716.

Lewis, L.A. et al. (2015). Transcriptional Dynamics Driving MAMP-Triggered Immunity and Pathogen Effector-Mediated Immunosuppression in Arabidopsis Leaves Following Infection with Pseudomonas syringae pv tomato DC3000. The Plant Cell 27: 3038–3064.

Li, B., Meng, X., Shan, L., and He, P. (2016). Transcriptional Regulation of Pattern-Triggered Immunity in Plants. Cell Host & Microbe 19: 641–650.

Li, C.H. and Tam, P.K.S. (1998). An iterative algorithm for minimum cross entropy thresholding. Pattern Recognition Letters 19: 771–776.

Li, J., Cao, L., and Staiger, C.J. (2017a). Capping Protein Modulates Actin Remodeling in Response to Reactive Oxygen Species during Plant Innate Immunity. Plant Physiology 173: 1125–1136.

Li, J., Henty-Ridilla, J.L., Staiger, B.H., Day, B., and Staiger, C.J. (2015). Capping protein integrates multiple MAMP signalling pathways to modulate actin dynamics during plant innate immunity. Nat Commun 6: 7206.

Li, P. and Day, B. (2019). Battlefield Cytoskeleton: Turning the Tide on Plant Immunity. MPMI 32: 25–34.

Li, P., Lu, Y.-J., Chen, H., and Day, B. (2020a). The Lifecycle of the Plant Immune System. Critical Reviews in Plant Sciences 39: 72–100.

Li, P., Zhang, Z., Day, B., and Tong, Y. (2021). Implicit Laplacian of Enhanced Edge (ILEE): An unguided algorithm for accurate and automated quantitative analysis of cytoskeletal images.

Li, S., Blanchoin, L., Yang, Z., and Lord, E.M. (2003). The Putative Arabidopsis Arp2/3 Complex Controls Leaf Cell Morphogenesis. Plant Physiology 132: 2034–2044.

Li, S., Han, X., Yang, L., Deng, X., Wu, H., Zhang, M., Liu, Y., Zhang, S., and Xu, J. (2018). Mitogen-activated protein kinases and calcium-dependent protein kinases are involved in wounding-induced ethylene biosynthesis in Arabidopsis thaliana. Plant, Cell & Environment 41: 134–147.

Li, W., Pang, S., Lu, Z., and Jin, B. (2020b). Function and Mechanism of WRKY Transcription Factors in Abiotic Stress Responses of Plants. Plants 9: 1515.

Li, Y., Williams, B., and Dickman, M. (2017b). Arabidopsis B-cell lymphoma2 (Bcl-2)-associated athanogene 7 (BAG7)-mediated heat tolerance requires translocation, sumoylation and binding to WRKY29. New Phytologist 214: 695–705.

Lian, N., Wang, X., Jing, Y., and Lin, J. (2021). Regulation of cytoskeleton-associated protein activities: Linking cellular signals to plant cytoskeletal function. Journal of Integrative Plant Biology 63: 241–250.

Liang, X., Ding, P., Lian, K., Wang, J., Ma, M., Li, L., Li, L., Li, M., Zhang, X., Chen, S., Zhang, Y., and Zhou, J.-M. (2016). Arabidopsis heterotrimeric G proteins regulate immunity by directly coupling to the FLS2 receptor. eLife 5: e13568.

Liao, D., Cao, Y., Sun, X., Espinoza, C., Nguyen, C.T., Liang, Y., and Stacey, G. (2017). Arabidopsis E3 ubiquitin ligase PLANT U-BOX13 (PUB13) regulates chitin receptor LYSIN MOTIF RECEPTOR KINASE5 (LYK5) protein abundance. New Phytologist 214: 1646–1656.

Lichtenstein, N., Geiger, B., and Kam, Z. (2003). Quantitative analysis of cytoskeletal organization by digital fluorescent microscopy. Cytometry Part A 54A: 8–18.

Liu, S., Kracher, B., Ziegler, J., Birkenbihl, R.P., and Somssich, I.E. (2015). Negative regulation of ABA signaling by WRKY33 is critical for Arabidopsis immunity towards Botrytis cinerea 2100. eLife 4: e07295.

Liu, Y., Mollaeian, K., and Ren, J. (2018). An Image Recognition-Based Approach to Actin Cytoskeleton Quantification. Electronics 7: 443.

Liu, Y., Nedo, A., Seward, K., Caplan, J., and Kambhamettu, C. (2020). Quantifying Actin Filaments in Microscopic Images using Keypoint Detection Techniques and A Fast Marching Algorithm. In 2020 IEEE International Conference on Image Processing (ICIP), pp. 2506–2510.

Liu, Z.-Q., Yan, L., Wu, Z., Mei, C., Lu, K., Yu, Y.-T., Liang, S., Zhang, X.-F., Wang, X.-F., and Zhang, D.-P. (2012). Cooperation of three WRKY-domain transcription factors WRKY18, WRKY40, and WRKY60 in repressing two ABA-responsive genes ABI4 and ABI5 in Arabidopsis. Journal of Experimental Botany 63: 6371–6392.

Lu, D., Lin, W., Gao, X., Wu, S., Cheng, C., Avila, J., Heese, A., Devarenne, T.P., He, P., and Shan, L. (2011). Direct Ubiquitination of Pattern Recognition Receptor FLS2 Attenuates Plant Innate Immunity. Science 332: 1439–1442.

Lu, Y.-J. and Day, B. (2017). Quantitative Evaluation of Plant Actin Cytoskeletal Organization During Immune Signaling. In Plant Pattern Recognition Receptors: Methods and Protocols, L. Shan and P. He, eds, Methods in Molecular Biology. (Springer: New York, NY), pp. 207–221.

Lu, Y.-J., Li, P., Shimono, M., Corrion, A., Higaki, T., He, S.Y., and Day, B. (2020). Arabidopsis calcium-dependent protein kinase 3 regulates actin cytoskeleton organization and immunity. Nature Communications 11: 6234.

Ludwig, N., Löhrer, M., Hempel, M., Mathea, S., Schliebner, I., Menzel, M., Kiesow, A., Schaffrath, U., Deising, H.B., and Horbach, R. (2014). Melanin Is Not Required for Turgor Generation but Enhances Cell-Wall Rigidity in Appressoria of the Corn Pathogen Colletotrichum graminicola. MPMI 27: 315–327.

Lumbreras, V., Vilela, B., Irar, S., Solé, M., Capellades, M., Valls, M., Coca, M., and Pagès, M. (2010). MAPK phosphatase MKP2 mediates disease responses in Arabidopsis and functionally interacts with MPK3 and MPK6. The Plant Journal 63: 1017–1030.

Luna, E., Pastor, V., Robert, J., Flors, V., Mauch-Mani, B., and Ton, J. (2011). Callose Deposition: A Multifaceted Plant Defense Response. MPMI 24: 183–193.

Mackey, D., Belkhadir, Y., Alonso, J.M., Ecker, J.R., and Dangl, J.L. (2003). Arabidopsis RIN4 Is a Target of the Type III Virulence Effector AvrRpt2 and Modulates RPS2-Mediated Resistance. Cell 112: 379–389.

Mackey, D., Holt, B.F., Wiig, A., and Dangl, J.L. (2002). RIN4 Interacts with Pseudomonas syringae Type III Effector Molecules and Is Required for RPM1-Mediated Resistance in Arabidopsis. Cell 108: 743–754.

Mao, G., Meng, X., Liu, Y., Zheng, Z., Chen, Z., and Zhang, S. (2011). Phosphorylation of a WRKY Transcription Factor by Two Pathogen-Responsive MAPKs Drives Phytoalexin Biosynthesis in Arabidopsis. The Plant Cell 23: 1639–1653.

Mbengue, M., Bourdais, G., Gervasi, F., Beck, M., Zhou, J., Spallek, T., Bartels, S., Boller, T., Ueda, T., Kuhn, H., and Robatzek, S. (2016). Clathrin-dependent endocytosis is required for immunity mediated by pattern recognition receptor kinases. PNAS 113: 11034–11039.

McDowell, J.M., Huang, S., McKinney, E.C., An, Y.-Q., and Meagher, R.B. (1996). Structure and Evolution of the Actin Gene Family in Arabidopsis thaliana. Genetics 142: 587–602.

McGhie, E.J., Brawn, L.C., Hume, P.J., Humphreys, D., and Koronakis, V. (2009). Salmonella takes control: effector-driven manipulation of the host. Current Opinion in Microbiology 12: 117–124.

van de Meene, A.M.L., Doblin, M.S., and Bacic, A. (2017). The plant secretory pathway seen through the lens of the cell wall. Protoplasma 254: 75–94.

Melak, M., Plessner, M., and Grosse, R. (2017). Correction: Actin visualization at a glance. Journal of Cell Science 130: 1688–1688.

Meng, X. and Zhang, S. (2013). MAPK Cascades in Plant Disease Resistance Signaling. Annual Review of Phytopathology 51: 245–266.

Miklis, M., Consonni, C., Bhat, R.A., Lipka, V., Schulze-Lefert, P., and Panstruga, R. (2007). Barley MLO Modulates Actin-Dependent and Actin-Independent Antifungal Defense Pathways at the Cell Periphery. Plant Physiology 144: 1132–1143.

Mine, A., Berens, M.L., Nobori, T., Anver, S., Fukumoto, K., Winkelmüller, T.M., Takeda, A., Becker, D., and Tsuda, K. (2017). Pathogen exploitation of an abscisic acid- and jasmonate-inducible MAPK phosphatase and its interception by Arabidopsis immunity. PNAS 114: 7456–7461.

Mine, A., Seyfferth, C., Kracher, B., Berens, M.L., Becker, D., and Tsuda, K. (2018). The Defense Phytohormone Signaling Network Enables Rapid, High-Amplitude Transcriptional Reprogramming during Effector-Triggered Immunity. The Plant Cell 30: 1199–1219.

Mithoe, S.C. and Menke, F.L. (2018). Regulation of pattern recognition receptor signalling by phosphorylation and ubiquitination. Current Opinion in Plant Biology 45: 162–170.

Mondal, H.A., Louis, J., Archer, L., Patel, M., Nalam, V.J., Sarowar, S., Sivapalan, V., Root, D.D., and Shah, J. (2018). Arabidopsis ACTIN-DEPOLYMERIZING FACTOR3 Is Required for Controlling Aphid Feeding from the Phloem. Plant Physiology 176: 879–890.

Monteiro, F. and Nishimura, M.T. (2018). Structural, Functional, and Genomic Diversity of Plant NLR Proteins: An Evolved Resource for Rational Engineering of Plant Immunity. Annual Review of Phytopathology 56: 243–267.

Moore, J.W., Loake, G.J., and Spoel, S.H. (2011). Transcription Dynamics in Plant Immunity. The Plant Cell 23: 2809–2820.

Morris, C.E., Barny, M.-A., Berge, O., Kinkel, L.L., and Lacroix, C. (2017). Frontiers for research on the ecology of plant-pathogenic bacteria: fundamentals for sustainability. Molecular Plant Pathology 18: 308–319.

Nagawa, S., Xu, T., Lin, D., Dhonukshe, P., Zhang, X., Friml, J., Scheres, B., Fu, Y., and Yang, Z. (2012). ROP GTPase-Dependent Actin Microfilaments Promote PIN1 Polarization by Localized Inhibition of Clathrin-Dependent Endocytosis. PLOS Biology 10: e1001299.

Nan, Q., Qian, D., Niu, Y., He, Y., Tong, S., Niu, Z., Ma, J., Yang, Y., An, L., Wan, D., and Xiang, Y. (2017). Plant Actin-Depolymerizing Factors Possess Opposing Biochemical Properties Arising from Key Amino Acid Changes throughout Evolution. The Plant Cell 29: 395–408.

Natesan, S.K.A., Sullivan, J.A., and Gray, J.C. (2009). Myosin XI Is Required for Actin-Associated Movement of Plastid Stromules. Molecular Plant 2: 1262–1272.

Nebenführ, A. and Dixit, R. (2018). Kinesins and Myosins: Molecular Motors that Coordinate Cellular Functions in Plants. Annual Review of Plant Biology 69: 329–361.

Niblack, W. (1985). An Introduction to Digital Image Processing (Prentice Hall).

Nomoto, M., Tada, Y., and Tsukagoshi, H. (2019). In vitro Protein-DNA Binding Assay (AlphaScreen® Technology). Bio Protoc 9: e3155.

Nühse, T.S., Bottrill, A.R., Jones, A.M.E., and Peck, S.C. (2007). Quantitative phosphoproteomic analysis of plasma membrane proteins reveals regulatory mechanisms of plant innate immune responses. The Plant Journal 51: 931–940.

Nunez-Iglesias, J., Blanch, A.J., Looker, O., Dixon, M.W., and Tilley, L. (2018). A new Python library to analyse skeleton images confirms malaria parasite remodelling of the red blood cell membrane skeleton. PeerJ 6: e4312.

Opalski, K.S., Schultheiss, H., Kogel, K.-H., and Hückelhoven, R. (2005). The receptor-like MLO protein and the RAC/ROP family G-protein RACB modulate actin reorganization in barley attacked by the biotrophic powdery mildew fungus Blumeria graminis f.sp. hordei. The Plant Journal 41: 291–303.

Ortiz-Martín, I., Thwaites, R., Macho, A.P., Mansfield, J.W., and Beuzón, C.R. (2010). Positive Regulation of the Hrp Type III Secretion System in Pseudomonas syringae pv. phaseolicola. MPMI 23: 665–681.

Ortiz-Morea, F.A. et al. (2016). Danger-associated peptide signaling in Arabidopsis requires clathrin. PNAS 113: 11028–11033.

Otsu, N. (1979). A Threshold Selection Method from Gray-Level Histograms. IEEE Transactions on Systems, Man, and Cybernetics 9: 62–66.

Paccanaro, M.C., Sella, L., Castiglioni, C., Giacomello, F., Martínez-Rocha, A.L., D'Ovidio, R., Schäfer, W., and Favaron, F. (2017). Synergistic Effect of Different Plant Cell Wall–Degrading Enzymes Is Important for Virulence of Fusarium graminearum. MPMI 30: 886–895.

Pandey, S.P., Roccaro, M., Schön, M., Logemann, E., and Somssich, I.E. (2010). Transcriptional reprogramming regulated by WRKY18 and WRKY40 facilitates powdery mildew infection of Arabidopsis. The Plant Journal 64: 912–923.

Park, E., Nedo, A., Caplan, J.L., and Dinesh-Kumar, S.P. (2018). Plant–microbe interactions: organelles and the cytoskeleton in action. New Phytologist 217: 1012–1028.

Pitzalis, N. and Heinlein, M. (2018). The roles of membranes and associated cytoskeleton in plant virus replication and cell-to-cell movement. Journal of Experimental Botany 69: 117–132.

Porter, K. and Day, B. (2016). From filaments to function: The role of the plant actin cytoskeleton in pathogen perception, signaling and immunity. Journal of Integrative Plant Biology 58: 299–311.

Porter, K., Shimono, M., Tian, M., and Day, B. (2012). Arabidopsis Actin-Depolymerizing Factor-4 Links Pathogen Perception, Defense Activation and Transcription to Cytoskeletal Dynamics. PLOS Pathogens 8: e1003006.

Postma, J., Liebrand, T.W.H., Bi, G., Evrard, A., Bye, R.R., Mbengue, M., Kuhn, H., Joosten, M.H.A.J., and Robatzek, S. (2016). Avr4 promotes Cf-4 receptor-like protein association with the BAK1/SERK3 receptor-like kinase to initiate receptor endocytosis and plant immunity. New Phytologist 210: 627–642.

Qi, Z., Verma, R., Gehring, C., Yamaguchi, Y., Zhao, Y., Ryan, C.A., and Berkowitz, G.A. (2010). Ca2+ signaling by plant Arabidopsis thaliana Pep peptides depends on AtPepR1, a receptor with guanylyl cyclase activity, and cGMP-activated Ca2+ channels. PNAS 107: 21193–21198.

Quiñones, B., Dulla, G., and Lindow, S.E. (2005). Quorum Sensing Regulates Exopolysaccharide Production, Motility, and Virulence in Pseudomonas syringae. MPMI 18: 682–693.

Robatzek, S., Chinchilla, D., and Boller, T. (2006). Ligand-induced endocytosis of the pattern recognition receptor FLS2 in Arabidopsis. Genes Dev. 20: 537–542.

Ruzicka, D.R., Kandasamy, M.K., McKinney, E.C., Burgos-Rivera, B., and Meagher, R.B. (2007). The ancient subclasses of Arabidopsis ACTIN DEPOLYMERIZING FACTOR genes exhibit novel and differential expression. The Plant Journal 52: 460–472.

Ryder, L.S. and Talbot, N.J. (2015). Regulation of appressorium development in pathogenic fungi. Current Opinion in Plant Biology 26: 8–13.

Saile, S.C., Jacob, P., Castel, B., Jubic, L.M., Salas-Gonzáles, I., Bäcker, M., Jones, J.D.G., Dangl, J.L., and Kasmi, F.E. (2020). Two unequally redundant "helper" immune receptor families mediate Arabidopsis thaliana intracellular "sensor" immune receptor functions. PLOS Biology 18: e3000783.

Sanabria, N., Goring, D., Nürnberger, T., and Dubery, I. (2008). Self/nonself perception and recognition mechanisms in plants: a comparison of self-incompatibility and innate immunity. New Phytologist 178: 503–514.

Sauvola, J. and Pietikäinen, M. (2000). Adaptive document image binarization. Pattern Recognition 33: 225–236.

Scharr, H. (2000). Optimal operators in digital image processing.

Schmidt, S.M. and Panstruga, R. (2007). Cytoskeleton functions in plant–microbe interactions. Physiological and Molecular Plant Pathology 71: 135–148.

Schneider, R., Hanak, T., Persson, S., and Voigt, C.A. (2016). Cellulose and callose synthesis and organization in focus, what's new? Current Opinion in Plant Biology 34: 9–16.

Schön, M., Töller, A., Diezel, C., Roth, C., Westphal, L., Wiermer, M., and Somssich, I.E. (2013). Analyses of wrky18 wrky40 Plants Reveal Critical Roles of SA/EDS1 Signaling and Indole-Glucosinolate Biosynthesis for Golovinomyces orontii Resistance and a Loss-of Resistance Towards Pseudomonas syringae pv. tomato AvrRPS4. MPMI 26: 758–767.

Segonzac, C., Macho, A.P., Sanmartín, M., Ntoukakis, V., Sánchez-Serrano, J.J., and Zipfel, C. (2014). Negative control of BAK1 by protein phosphatase 2A during plant innate immunity. The EMBO Journal 33: 2069–2079.

Shah, S.A., Santago, P., and Rubin, B.K. (2005). Quantification of biopolymer filament structure. Ultramicroscopy 104: 244–254.

Sharma, B., Joshi, D., Yadav, P.K., Gupta, A.K., and Bhatt, T.K. (2016). Role of Ubiquitin-Mediated Degradation System in Plant Biology. Frontiers in Plant Science 7: 806.

Sharma, D. and Kanneganti, T.-D. (2016). The cell biology of inflammasomes: Mechanisms of inflammasome activation and regulation. Journal of Cell Biology 213: 617–629.

Shimono, M., Higaki, T., Kaku, H., Shibuya, N., Hasezawa, S., and Day, B. (2016a). Quantitative Evaluation of Stomatal Cytoskeletal Patterns during the Activation of Immune Signaling in Arabidopsis thaliana. PLOS ONE 11: e0159291.

Shimono, M., Lu, Y.-J., Porter, K., Kvitko, B.H., Henty-Ridilla, J., Creason, A., He, S.Y., Chang, J.H., Staiger, C.J., and Day, B. (2016b). The *Pseudomonas syringae* Type III Effector HopG1 Induces Actin Remodeling to Promote Symptom Development and Susceptibility during Infection. Plant Physiol. 171: 2239–2255.

Singh, A., Sagar, S., and Biswas, D.K. (2017). Calcium Dependent Protein Kinase, a Versatile Player in Plant Stress Management and Development. Critical Reviews in Plant Sciences 36: 336–352.

Skalamera, D. and Heath, M.C. (1998). Changes in the cytoskeleton accompanying infection-induced nuclear movements and the hypersensitive response in plant cells invaded by rust fungi. The Plant Journal 16: 191–200.

Smith, J.M. and Heese, A. (2014). Rapid bioassay to measure early reactive oxygen species production in Arabidopsis leave tissue in response to living Pseudomonas syringae. Plant Methods 10: 6.

Stam, R., Mantelin, S., McLellan, H., and Thilliez, G. (2014). The role of effectors in nonhost resistance to filamentous plant pathogens. Frontiers in Plant Science 5: 582.

Staskawicz, B.J. (2001). Genetics of Plant-Pathogen Interactions Specifying Plant Disease Resistance. Plant Physiology 125: 73–76.

Su, S., Liu, Z., Chen, C., Zhang, Y., Wang, X., Zhu, L., Miao, L., Wang, X.-C., and Yuan, M. (2010). Cucumber Mosaic Virus Movement Protein Severs Actin Filaments to Increase the Plasmodesmal Size Exclusion Limit in Tobacco. The Plant Cell 22: 1373–1387.

Sukarta, O.C.A., Slootweg, E.J., and Goverse, A. (2016). Structure-informed insights for NLR functioning in plant immunity. Seminars in Cell & Developmental Biology 56: 134–149.

Sun, H., Qiao, Z., Chua, K.P., Tursic, A., Liu, X., Gao, Y.-G., Mu, Y., Hou, X., and Miao, Y. (2018). Profilin Negatively Regulates Formin-Mediated Actin Assembly to Modulate PAMP-Triggered Plant Immunity. Current Biology 28: 1882-1895.e7.

Sun, Y., Zhu, Y.-X., Balint-Kurti, P.J., and Wang, G.-F. (2020). Fine-Tuning Immunity: Players and Regulators for Plant NLRs. Trends in Plant Science 25: 695–713.

Takemoto, D., Jones, D.A., and Hardham, A.R. (2003). GFP-tagging of cell components reveals the dynamics of subcellular re-organization in response to infection of Arabidopsis by oomycete pathogens. The Plant Journal 33: 775–792.

Takemoto, D., Jones, D.A., and Hardham, A.R. (2006). Re-organization of the cytoskeleton and endoplasmic reticulum in the Arabidopsis pen1-1 mutant inoculated with the non-adapted powdery mildew pathogen, Blumeria graminis f. sp. hordei. Molecular Plant Pathology 7: 553–563.

Tanaka, K., Takeda, S., Mitsuoka, K., Oda, T., Kimura-Sakiyama, C., Maéda, Y., and Narita, A. (2018). Structural basis for cofilin binding and actin filament disassembly. Nat Commun 9: 1860.

Tang, C., Deng, L., Chang, D., Chen, S., Wang, X., and Kang, Z. (2016). TaADF3, an Actin-Depolymerizing Factor, Negatively Modulates Wheat Resistance Against Puccinia striiformis. Frontiers in Plant Science 6: 1214.

Tang, W., Gao, C., Wang, J., Yin, Z., Zhang, J., Ji, J., Zhang, H., Zheng, X., Zhang, Z., and Wang, P. (2018). Disruption of actin motor function due to MoMyo5 mutation impairs host penetration and pathogenicity in Magnaporthe oryzae. Molecular Plant Pathology 19: 689–699.

Tang, X., Xiao, Y., and Zhou, J.-M. (2006). Regulation of the Type III Secretion System in Phytopathogenic Bacteria. MPMI 19: 1159–1166.

Tena, G., Boudsocq, M., and Sheen, J. (2011). Protein kinase signaling networks in plant innate immunity. Current Opinion in Plant Biology 14: 519–529.

Tian, M., Chaudhry, F., Ruzicka, D.R., Meagher, R.B., Staiger, C.J., and Day, B. (2009). Arabidopsis Actin-Depolymerizing Factor AtADF4 Mediates Defense Signal Transduction Triggered by the Pseudomonas syringae Effector AvrPphB. Plant Physiology 150: 815–824.

Tominaga, M. and Ito, K. (2015). The molecular mechanism and physiological role of cytoplasmic streaming. Current Opinion in Plant Biology 27: 104–110.

Tsuda, K. and Somssich, I.E. (2015). Transcriptional networks in plant immunity. New Phytologist 206: 932–947.

Underwood, W. (2012). The Plant Cell Wall: A Dynamic Barrier Against Pathogen Invasion. Frontiers in Plant Science 3: 85.

Van Ngo, H. and Mostowy, S. (2019). Role of septins in microbial infection. Journal of Cell Science 132.

Verdeil, J.-L., Alemanno, L., Niemenak, N., and Tranbarger, T.J. (2007). Pluripotent versus totipotent plant stem cells: dependence versus autonomy? Trends in Plant Science 12: 245–252.

Verma, V., Ravindran, P., and Kumar, P.P. (2016). Plant hormone-mediated regulation of stress responses. BMC Plant Biology 16: 86.

Wang, J. et al. (2018). A Regulatory Module Controlling Homeostasis of a Plant Immune Kinase. Molecular Cell 69: 493-504.e6.

Wang, J., Hu, M., Wang, J., Qi, J., Han, Z., Wang, G., Qi, Y., Wang, H.-W., Zhou, J.-M., and Chai, J. (2019). Reconstitution and structure of a plant NLR resistosome conferring immunity. Science 364: eaav5870.

Wang, W., Wen, Y., Berkey, R., and Xiao, S. (2009). Specific Targeting of the Arabidopsis Resistance Protein RPW8.2 to the Interfacial Membrane Encasing the Fungal Haustorium Renders Broad-Spectrum Resistance to Powdery Mildew. The Plant Cell 21: 2898–2913.

Wang, Y., Zheng, X., Yu, B., Han, S., Guo, J., Tang, H., Yu, A.Y.L., Deng, H., Hong, Y., and Liu, Y. (2015). Disruption of microtubules in plants suppresses macroautophagy and triggers starch excess-associated chloroplast autophagy. Autophagy 11: 2259–2274.

Wei, M., Fan, X., Ding, M., Li, R., Shao, S., Hou, Y., Meng, S., Tang, F., Li, C., and Sun, Y. Nuclear actin regulates inducible transcription by enhancing RNA polymerase II clustering. Science Advances 6: eaay6515.

Withers, J. and Dong, X. (2017). Post-translational regulation of plant immunity. Current Opinion in Plant Biology 38: 124–132.

Wu, D., Ding, W., Zhang, Y., Liu, X., and Yang, L. (2015). Oleanolic Acid Induces the Type III Secretion System of Ralstonia solanacearum. Frontiers in Microbiology 6: 1466.

Wu, F.-H., Shen, S.-C., Lee, L.-Y., Lee, S.-H., Chan, M.-T., and Lin, C.-S. (2009). Tape-Arabidopsis Sandwich - a simpler Arabidopsis protoplast isolation method. Plant Methods 5: 16.

Xie, K., Chen, J., Wang, Q., and Yang, Y. (2014). Direct Phosphorylation and Activation of a Mitogen-Activated Protein Kinase by a Calcium-Dependent Protein Kinase in Rice. The Plant Cell 26: 3077–3089.

Xin, X.-F., Kvitko, B., and He, S.Y. (2018). Pseudomonas syringae: what it takes to be a pathogen. Nat Rev Microbiol 16: 316–328.

Xu, X., Chen, C., Fan, B., and Chen, Z. (2006). Physical and Functional Interactions between Pathogen-Induced Arabidopsis WRKY18, WRKY40, and WRKY60 Transcription Factors. The Plant Cell 18: 1310–1326.

Yang, L., Qin, L., Liu, G., Peremyslov, V.V., Dolja, V.V., and Wei, Y. (2014). Myosins XI modulate host cellular responses and penetration resistance to fungal pathogens. PNAS 111: 13996–14001.

Yi, M. and Valent, B. (2013). Communication Between Filamentous Pathogens and Plants at the Biotrophic Interface. Annual Review of Phytopathology 51: 587–611.

Yi, S.Y., Shirasu, K., Moon, J.S., Lee, S.-G., and Kwon, S.-Y. (2014). The Activated SA and JA Signaling Pathways Have an Influence on flg22-Triggered Oxidative Burst and Callose Deposition. PLOS ONE 9: e88951.

Yoo, S.-D., Cho, Y.-H., and Sheen, J. (2007). Arabidopsis mesophyll protoplasts: a versatile cell system for transient gene expression analysis. Nat Protoc 2: 1565–1572.

Yu, Y., Qiao, L., Chen, J., Rong, Y., Zhao, Y., Cui, X., Xu, J., Hou, X., and Dong, C.-H. (2020). Arabidopsis REM16 acts as a B3 domain transcription factor to promote flowering time via directly binding to the promoters of SOC1 and FT. The Plant Journal 103: 1386–1398.

Zack, G.W., Rogers, W.E., and Latt, S.A. (1977). Automatic measurement of sister chromatid exchange frequency. J Histochem Cytochem. 25: 741–753.

Zhang, Y., Li, J., Zhang, W., Wang, R., Qiu, Q., Luo, F., Hikichi, Y., Ohnishi, K., and Ding, W. (2017). Ferulic Acid, But Not All Hydroxycinnamic Acids, Is a Novel T3SS Inducer of Ralstonia solanacearum and Promotes Its Infection Process in Host Plants under Hydroponic Condition. Frontiers in Plant Science 8: 1595.

Zheng, Z., Qamar, S.A., Chen, Z., and Mengiste, T. (2006). Arabidopsis WRKY33 transcription factor is required for resistance to necrotrophic fungal pathogens. The Plant Journal 48: 592–605.